

# REPORT DOCUMENTATION PAGE

Form Approved  
OMB No. 0704-0188

Public reporting burden for this collection of information is estimated to average 1 hour per response, including the time for reviewing instructions, searching existing data sources, gathering and maintaining the data needed, and completing and reviewing the collection of information. Send comments regarding this burden estimate or any other aspect of this collection of information, including suggestions for reducing the burden, to Washington Headquarters Services, Directorate for Information Operations and Reports, 1215 Jefferson Davis Highway, Suite 1204, Arlington, VA 22202-4302, and to the Office of Management and Budget, Paperwork Reduction Project (0704-0188), Washington, DC 20503.

1. AGENCY USE ONLY (Leave blank)		2. REPORT DATE		3. REPORT TYPE AND DATES COVERED FINAL	
4. TITLE AND SUBTITLE Structural, Chemical and Electronic Properties of Superconducting Thin Films and Junctions				5. FUNDING NUMBERS 61102F 2305/GS	
6. AUTHOR(S) Professor Michael E. McHenry					
7. PERFORMING ORGANIZATION NAME(S) AND ADDRESS(ES) Carnegie Mellon University Pittsburgh, PA				8. PERFORMING ORGANIZATION REPORT NUMBER AFOSR-TR- 95 0162	
9. SPONSORING / MONITORING AGENCY NAME(S) AND ADDRESS(ES) AFOSR/NE 110 Duncan Avenue Suite B115 Bolling AFB DC 20332-0001				10. SPONSORING / MONITORING AGENCY REPORT NUMBER F49620-92-J-0415	
11. SUPPLEMENTARY NOTES					
12. DISTRIBUTION STATEMENT (If applicable) APPROVED FOR PUBLIC RELEASE: DISTRIBUTION UNLIMITED					
13. ABSTRACT (If applicable) SEE FINAL REPORT ABSTRACT					
14. SUBJECT TERMS				15. NUMBER OF PAGES	
16. SECURITY CLASSIFICATION OF REPORT UNCLASSIFIED				17. PRICE CODE	
18. SECURITY CLASSIFICATION OF ABSTRACT UNCLASSIFIED		19. SECURITY CLASSIFICATION OF ABSTRACT UNCLASSIFIED		20. LIMITATION OF ABSTRACT UNCLASSIFIED	

DTIC  
SELECTE  
MAR 27 1995  
C

19950322 164

**STRUCTURAL, CHEMICAL, AND ELECTRONIC  
PROPERTIES OF SUPERCONDUCTING  
THIN FILMS AND JUNCTIONS**

*Submitted in partial fulfillment of the requirements  
for the degree of Doctor of Philosophy*

by

Beth A. Baumert

Department of Materials Science and Engineering  
Carnegie Mellon University  
Pittsburgh, Pennsylvania

May 1994

Advisor: Professor Michael E. McHenry

Accession For	
NTIS CRA&I	<input checked="checked" type="checkbox"/>
DTIC TAB	<input type="checkbox"/>
Unannounced	<input type="checkbox"/>
Justification	
By	
Distribution	
Date	
Dist	Author
A-1	

Research supported by the U.S. Air Force Office of Scientific Research  
under contract numbers F49620-92-J-0415, F49620-91-C-0034,  
and F49620-94-C-0021.

To my parents

Copyright © 1994  
Beth A. Baumert  
All rights reserved.

## Abstract

$\text{Ba}_{1-x}\text{K}_x\text{BiO}_3$  (BKBO) has a transition temperature,  $T_c$ , of 34 K and is unique among the high-temperature oxide superconductors because it is isotropic. It has been little studied and it is desirable to understand its behavior from the perspectives of both potential electronic applications and fundamental understanding of superconductivity. This study has involved a determination of the structural, electronic, and chemical properties of BKBO films and junctions deposited by rf magnetron sputtering. It was found that films with the highest  $T_c$  and lowest rocking curve widths were consistently grown on  $\text{SrTiO}_3$ . This material was therefore used as a buffer layer for growing high-quality BKBO films on the more practical substrates  $\text{LaAlO}_3$  and  $\text{NdGaO}_3$ .  $\text{SrTiO}_3$  was also used as a barrier to fabricate BKBO/ $\text{SrTiO}_3$ /BKBO SIS junctions for the first time. These junctions exhibited tunneling behavior. Modelling based on electrical measurements and electron diffraction observations of surface structure indicated island-type growth of the barrier material. The thickness variation in the tunnel barrier as a result of island formation limits the practical potential of such junctions in most applications where tunneling current uniformity and junction reproducibility are required.

As an alternative to BKBO junctions,  $\text{YBa}_2\text{Cu}_3\text{O}_{7-x}$  (YBCO) was used in junction fabrication. YBCO is a desirable material for junctions despite the difficulties that arise due to its anisotropy because its  $T_c$  of 90 K allows the use of liquid nitrogen as a cryogen and because it has no volatile components. High-quality

films of YBCO were deposited using rf magnetron sputtering. Barriers such as Co-doped YBCO on YBCO have been studied and used to fabricate SNS edge junctions.

## Acknowledgements

I am particularly grateful to Dr. Harold Weinstock of the Air Force Office of Scientific Research for funding my work. Without his support, this project would not have been possible.

I thank my thesis committee for their suggestions and efforts: Dr. Marek Skowronski for first telling me of my acceptance here and for making semiconductors interesting, Dr. David Laughlin for his patient help and encouragement, and my advisors Dr. Michael McHenry for his advice and support and most of all for allowing me to work on a project of my own interest, and Dr. John Talvacchio of Westinghouse for countless hours of guidance and for teaching me all about Josephson junctions.

I am grateful to the Superconductivity Group at Westinghouse for their assistance in my research there, and particularly to Martin Forrester for his kindness, patient guidance and assistance, advice, and encouragement, to John Gavalier for his technical advice and for being one of the most kindhearted and decent people I know, to Jim Uphoff for a great deal of assistance and for being a true gentleman, to Ron Grassel for a great deal of assistance and advice about the assembly of my sputtering system, to Al Stewart for his assistance and patience, to Stan Pieseski for always listening to me when I really needed a friend, and to Hodge Worsham for his friendship and advice. I am very grateful to Bill Partlow for letting me use his power supply for all of those months, and to Alexana Roshko of NIST for observing my samples with the AFM, to George Burcin and Tom Mullen for their assistance with

EDXS, to Dave Detar for Auger depth profiling, and to John T., Martin, and Jerry for the fabrication and measurement of YBCO edge junctions. I also thank Gene Madia, Jerry Faychak, and Carl Brown for their moral support, and Mike Janocko and John Gavalier for many great walks/discussions. I thank my friends at Westinghouse for their friendship and support and Rob Young for a lot of good advice.

The encouragement and understanding I received from B.J. Cline, Madeline Lesko, Amy Watts, Valerie Scott, and Carole Carter got me through the most difficult of times, and I am truly grateful to them for this. I also thank my friends at Carnegie Mellon, especially Celeste McCallen, for making life more bearable. I thank Wendy Kelly for being the best friend I ever had.

Ich muß Dr. Hallstein viel danken. Er ist ein netter, süßer Mann und er macht Deutsch Spaß. Er ist bestimmt mein Lieblingsprofessor. Ich muß auch Dr. William Johnson, Werner Hort, und Michael und Elke Fahrman für viele gute Gespräche danken.

My friends at DuPont and especially my mother greatly encouraged me to return to graduate school, and I am indeed grateful to them and to Barry Johnson and Kevin Scott for believing in me.

Most of all, my deepest gratitude and love go to my family for their love, encouragement, and support. I never could have done this without them.



## Table of Contents

<u>Section</u>	<u>Page</u>
List of Tables .....	ix
List of Figures .....	x
Introduction .....	1
I. Principles of Superconductivity .....	4
A. Bulk Properties	
1. Cooper Pairing, Concept of Electron-Phonon Interaction,.....	5
and the BCS Energy Gap	
2. Resistive Transition, Variable-Range Hopping Conduction, .....	7
and the Two-Fluid Model	
3. Meissner Effect, Type I and II Superconductivity, and .....	10
Length Scales	
B. Josephson Junctions	
1. Tunneling Phenomena in SIS Junctions .....	15
2. Circuit Analog .....	20
3. SNS Junctions .....	20
4. Magnetic Field Effects .....	23
5. Applications .....	25
II. Literature Review	
A. Historical Background of Superconductivity .....	29
B. Historical Background of Josephson Junction Development .....	33
C. Introduction to BKBO Properties	
1. Structure .....	35
2. Pairing Mechanism .....	40
3. Electronic Structure .....	41
4. Transition Temperature .....	44
5. Resistivity .....	45
6. Magnetic Properties .....	47
D. YBCO Properties	
1. Structure .....	50
2. Electronic Structure .....	52
3. Conduction Mechanism .....	56
4. Transition Temperature .....	58
5. Resistivity .....	58
6. Magnetic Properties .....	58

III. Research Objectives	
A. Necessary Junction Properties	
1. Tunnel Junctions (SIS) .....	63
2. Edge Junctions (SNS) .....	65
B. Methods.....	68
IV. Experimental Techniques	
A. Review of Experimental Methods	
1. RF Magnetron Sputtering .....	72
2. XPS .....	75
3. EDXS .....	79
4. RHEED and LEED .....	81
5. X-Ray Diffraction.....	83
6. Resistivity Measurements .....	88
7. Inductance Measurements .....	90
8. Critical Current Density Measurements.....	90
9. Junction Measurements .....	92
B. Film Fabrication .....	92
C. Junction Fabrication .....	94
V. Results and Discussion	
A. BKBO Films .....	98
B. BKBO Junctions .....	119
C. YBCO Films .....	128
D. Barrier Films.....	128
E. YBCO Edge Junctions .....	131
VI. Conclusions	
A. Discussion of Results	
1. BKBO Films.....	135
2. BKBO Junctions.....	137
3. YBCO and Barrier Films .....	139
4. YBCO Edge Junctions.....	139
B. Suggestions for Future Research .....	140
 Appendix I: X-Ray Structure Factor Calculations.....	142
Appendix II: Simmons Model for a Rectangular Barrier.....	148
Appendix III: RHEED and LEED Patterns .....	149
 References.....	153

## List of Tables

<u>Number</u>	<u>Title</u>	<u>Page</u>
I	Oxide Superconductors with $T_c$ below 15 K .....	28
II	Lattice Parameters of Superconducting YBCO .....	49
III	A Summary of Experimental Data on the Upper ..... Critical Fields of YBCO	59
IV	A Summary of Experimental Data on the Lower..... Critical Fields of YBCO	59
V	Properties of Typical Substrate Materials Compared..... to those of YBCO	62
VI	Properties of Typical Substrate, Insulator, and Barrier ..... Materials Compared to those of YBCO	65

## List of Figures

<u>No.</u>	<u>Caption</u>	<u>Page</u>
1	Dependence of the superconducting gap on temperature. The gap is zero at the transition temperature, $T_C$ [1].	7
2	Superconducting transitions in pure and impure tin. Impure materials have much broader transitions [5].	7
3	Magnetization versus applied field for (a) a Type I superconductor, which becomes normal as soon as $H_C$ is reached, and for (b) a Type II superconductor, which is in a flux vortex state between $H_{C1}$ and $H_{C2}$ and then is normal above $H_{C2}$ . The area under both curves is the same for a given $H_C$ [4].	12
4	Superconductor coherence length, $\xi$ , and normal phase penetration depth, $\lambda$ , at a superconductor/normal phase interface [9].	12
5	(a) Energy band diagram for two identical superconductors separated by a thin insulator. (b) Density of states for the superconductor [2].	17
6	Energy band diagram for two identical superconductors and an insulator with an applied voltage of $2\Delta/e$ [2].	17
7	I-V characteristic for an SIS Josephson junction at $T=0$ [15].	18
8	I-V characteristic for an SIS Josephson junction at $T>0$ [2].	18
9	Energy band diagram for two different superconductors separated by a thin insulator at (a) $V=0$ (b) $V=(\Delta_2-\Delta_1)/e$ (c) $V=(\Delta_1+\Delta_2)/e$ [2]	19
10	I-V characteristic for two different superconductors separated by a thin insulator. There is a negative resistance region for $(\Delta_2 - \Delta_1)/2e < V < (\Delta_1 + \Delta_2)/2e$ [2].	21
11	I-V characteristic for an SNS Josephson junction [16].	21
12	The circuit equivalent for a Josephson junction [17].	22
13	Schematic of the spatial dependence of $i_C$ and $J_C$ vs. the superconducting wavefunction for an SNS junction [18].	22

14	The current density distribution for a single, short Josephson junction with an applied magnetic field. The current density is maximized in each case. $\Phi_J$ is the flux in the junction, $\Phi_0$ a flux quantum, $d$ the length of the junction, and $\phi$ the phase difference [19].	24
15	Current vs. applied magnetic field response of a single, short Josephson junction with no self-fields [19].	25
16	Current vs. magnetic field response of a SQUID [19].	25
17	(a) I-V characteristic of an SIS Josephson junction, showing "zero" and "one" states [23] (b) I-V characteristic of a SQUID loop for integer and half-integer multiples of the flux quantum in the loop, showing "zero" and "one" states [16].	28
18	The A15 crystal structure for $A_3B$ compounds [26].	30
19	Schematic of various types of SNS and SS'S Josephson junctions.	34
20	The structure of BKBO [64].	36
21	"Phase" diagram for $Ba_{1-x}K_xBiO_3$ as a function of potassium content, $x$ [65].	36
22	Crystal structures of several compounds in the BKBO series. The figures below them show the tilting of the $BiO_6$ octahedra [68].	38
23	X-ray diffraction powder pattern of BKBO. Inset shows ac susceptibility of the sample [69].	38
24	Pseudocubic lattice parameter change as a function of potassium content, $x$ [65].	39
25	Energy band diagram for BKBO as a function of crystallographic direction in the Brillouin zone [36].	42
26	Schematic of density of states for $Bi_2O_3$ [101].	43
27	Variation of transition temperature of BKBO with potassium content, $x$ [65].	46
28	Lower critical field of BKBO as a function of temperature, giving $H_{c1} = 419 \pm 24$ Oe and $\lambda = 0.12 \pm 0.02$ $\mu m$ [122].	48

29	A summary of upper critical field values measured for BPBO and BKBO using various techniques, including magnetization, resistance, and specific heat [123].	48
30	Upper critical field as a function of temperature measured on a BKBO single crystal in a pulsed magnetic field. The solid line is based on modelling [124].	49
31	Upper critical field as a function of temperature for a BKBO single crystal. These results yield the values $dH_{C2}/dT = -4.8 \pm 0.1$ kOe/K, $\xi(0) = 58 \pm 1$ Å, and $H_{C2}(0) = 96 \pm 2$ kOe [122].	49
32	Structure of superconducting YBCO	51
33	Possible phase diagram of $YBa_2Cu_3O_{6+\delta}$ assuming only tetragonal and orthorhombic phases are present [135].	53
34	The <i>a</i> - and <i>b</i> -axis lattice parameters of YBCO vs. temperature for samples heated in 100% oxygen [134].	54
35	Possible phase diagram for binary cut through the CuO-YO <sub>1.5</sub> -BaO phase diagram [140].	54
36	Energy band diagram for YBCO as a function of crystallographic direction in the Brillouin zone. The cross-hatched area denotes a large number of weakly bonded Cu-O bands [142].	56
37	YBCO structure showing alternating conduction layers and charge reservoir layers. The conduction layers consist of two CuO <sub>2</sub> planes separated by yttrium atoms. The charge reservoir layers consist of CuO <sub>x</sub> chains along the <i>b</i> direction and also Ba and O atoms. The oxygen content near the copper chains is variable: <i>x</i> ranges from 0 to 1 [143].	57
38	Dependence of $T_C$ and $\rho$ on oxygen content of YBCO. The +'s represent the range of the resistive transition [136].	59
39	In-plane resistivity $\rho_{ab}$ and perpendicular resistivity $\rho_c$ of a YBCO single crystal as functions of temperature. The former shows metallic behavior and the latter, semiconductor-like [144].	60
40	Inverse of the Hall coefficient measured on three YBCO crystals. There is a strong temperature dependence which is most pronounced when $T_C$ is optimized [141].	60

41	I-V characteristic for a junction with 35 GHz applied rf power. Solid lines show experimental results. Broken lines give results of calculations without noise [159].	71
42	Depiction of magnetron sputtering process [160].	73
43	Riber chamber with sputtering and evaporation capabilities and <i>in-situ</i> RHEED, LEED, and XPS.	73
44	The chamber used for sputter deposition of BKBO and YBCO films.	74
45	Ionization energies for iron and uranium, where the depth of the state below the Fermi level is proportional to the ionization energy [161].	76
46	XPS survey scan of a BKBO film with Ba, Bi, and O lines identified.	77
47	XPS scan with distinct energy windows for the elements present in the BKBO film observed.	79
48	Depiction of the generation of x-rays by interaction of electromagnetic radiation with an atom, using the Bohr model of the atom [162].	81
49	Reciprocal lattice and Ewald sphere constructions. Diffraction geometry and momentum shown are appropriate for (a) LEED (b) RHEED [163].	82
50	Reciprocal lattice for a single plane of atoms, for which the reciprocal lattice is a set of rods normal to the plane of the layer, and Ewald construction for (a) LEED (b) RHEED [163].	82
51	Allowed volume of measurement in diffraction space with $\phi$ and $\psi$ angles depicted [164].	84
52	Schematic of instrument with parallel beam optics employed in measurement of highly textured films [164].	84
53	Reciprocal space map used in determination of measurement parameters. One chooses the desired (hkl) with the cursor in the allowed region and is presented with the optimum $2\theta$ , $\omega$ , and $\phi$ angles based on a pre-defined unit cell of expected dimensions [164].	85

54	Diagram of diffractometer positions for a BKBO (303) reflection to be observed.	85
55	Schematic of rocking curve width measurements for the growth direction and in the plane of the film.	87
56	Configuration of the mask used to pattern films for critical current density measurements.	91
57	Schematic of the configuration used in BKBO tunnel junction measurements [171].	91
58	Procedure used in patterning edge junctions.	96
59	XPS scan of a BKBO film showing the composition of the native surface layer. Note the carbon peak at 969 eV. The other peaks are all Ba, K, Bi, or O peaks from the underlying film.	99
60	Comparison of the superconducting transition of a film shortly after deposition to that of the same film one year later. The transition temperature is very similar but the resistivity has changed by $\sim 50 \mu\Omega\text{-cm}$ .	99
61	Background subtraction shown for a BKBO single-crystal spectrum after the standard "Fe efficiency" program was run in order to calibrate the background spectrum.	101
62	Auger depth profile of T91-83-S3, a 4300 Å BKBO film grown on a 190 Å BaBiO <sub>3</sub> buffer and a SrTiO <sub>3</sub> substrate. Beam used was 10 kV, 38 nA (a) expanded scale showing C and O (at top) peaks at surface (b) expanded scale for BKBO film (c) scan for entire sample	102
63	LEED patterns of (a) a BKBO counter electrode and (b) an MgO barrier. The electron energies were 20.3 and 143.0 eV, respectively [171].	104
64	RHEED patterns for (a) a BKBO base electrode (b) an MgO barrier on BKBO (c) a SrTiO <sub>3</sub> barrier on BKBO and (d) a BKBO counter electrode grown on the SrTiO <sub>3</sub> barrier [171].	104
65	Typical $2\theta$ - $\omega$ scan for a BKBO film of mixed orientation on LaAlO <sub>3</sub> .	106
66	X-ray $2\theta$ scan showing a comparison of the (022) and (003) peaks of a BKBO film on NdGaO <sub>3</sub> .	106



67	X-ray $2\theta$ scan showing a comparison of (011) to (001) BKBO growth and how $\text{SrTiO}_3$ buffer layers simulate $\text{SrTiO}_3$ single-crystal substrates [58].	108
68	Mosaic spread of misaligned grains for the (001) growth direction of BKBO films. This shows the improvement gained by using $\text{SrTiO}_3$ buffer layers and how they mimic $\text{SrTiO}_3$ substrates [58].	108
69	Rocking curve width, $\Delta\omega_2$ , of BKBO (303) peak showing the mosaic spread in the plane of a BKBO film on $\text{NdGaO}_3$ .	109
70	This $\phi$ scan is of the BKBO, $\text{SrTiO}_3$ , and $\text{LaAlO}_3$ {033} x-ray diffraction peaks and shows the in-plane orientation of a BKBO (001) film grown on $\text{SrTiO}_3$ -buffered $\text{LaAlO}_3$ [58].	109
71	Orientation of BKBO (011) on $\text{LaAlO}_3$ (001) as determined by a $\phi$ scan.	110
72	Schematic of nucleation occurring on a flat surface and on a step. Addition of a single atom onto (a) a flat interface increases the number of broken bonds by four (b) a ledge increases the number of broken bonds by two (c) a jog does not change the number of broken bonds [177].	110
73	X-ray $2\theta$ - $\theta$ scans showing (a) {220} peak splitting (b) {110} splitting for BKBO films which are believed to have randomly-oriented orthorhombic grains.	112
74	Transition temperature for a BKBO film on $\text{SrTiO}_3$ -buffered $\text{LaAlO}_3$ . The use of the buffer raised the $T_c$ by 3 K.	113
75	Transition temperature for a BKBO film grown directly on a $\text{SrTiO}_3$ substrate. This film was deposited during the same run as that shown in Figure 74.	113
76	Resistivity vs. temperature for a BKBO film grown on $\text{SrTiO}_3$ . This film had a particularly low resistivity of $68 \mu\Omega\cdot\text{cm}$ just above the transition.	114
77	Resistivity vs. temperature for a BKBO film on $\text{MgO}$ , showing an initial rise and then a drop in resistivity. This film was grown in the same run as that of Figure 76.	116

78	(a) Resistivity vs. temperature for a BKBO film grown on LaAlO <sub>3</sub> . This film exhibits variable-range hopping conduction. (b) Plot of $\rho$ vs. $T^{-1/4}$ for this film and two non-superconducting samples. Variable-range hopping has such a temperature dependence. (c) Plot of $\rho$ vs. $1/T$ , showing that thermal excitation is <b>not</b> the mechanism responsible for conduction.	116-117
79	Superconductive transitions for a BKBO film on LaAlO <sub>3</sub> . Inset shows resistive transition at ~18.5 K and inductive at ~17.2 K.	118
80	Critical current density measurement of a BKBO film [171].	118
81	SIN tunneling data for a BKBO/native barrier/Ag junction at 4.2 K [171].	120
82	SIN tunneling data for a BKBO/native barrier/Ag junction at various temperatures. It can be seen that the gap has closed by 13.0 K [171].	120
83	XPS scans of sample T92-85-B1, a BKBO film on MgO. (a) shows a scan for the BKBO film without oxygen anneal (b) is for a MgO barrier on a BKBO film. The tall peak in the fourth window of (b) is a Mg peak. Note how the Bi, Ba, and K peaks have been attenuated by the presence of the MgO overlayer. The peaks in (a) have not shifted in KE in (b), however, indicating that the two layers have not reacted.	122
84	I-V characteristics for an epitaxial BKBO/SrTiO <sub>3</sub> /BKBO trilayer junction at various temperatures below $T_C$ [58].	125
85	Tunneling data for an epitaxial BKBO/SrTiO <sub>3</sub> /BKBO trilayer junction at various temperatures below $T_C$ [58].	125
86	I-V characteristic of an all-BKBO SIS tunnel junction at 4.2 K. Nominal area of the device is 10 x 10 $\mu\text{m}$ . Scales are vertical current = 1 $\mu\text{A}/\text{div.}$ , horizontal voltage = 5 mV/div. $T_C$ ( $R=0$ ) of the BKBO is 23 K [57].	126
87	Conductance vs. bias voltage taken at four different temperatures below $T_C$ on an all-BKBO junction [57].	126
88	Resistive (90 K) and inductive (86.1 K) transitions for a YBCO film on LaAlO <sub>3</sub> .	129
89	The $\rho$ vs. $T$ and $I$ vs. $T$ curves for a YBCO film on LaAlO <sub>3</sub> . The ratio $\rho(300\text{ K})/\rho(100\text{ K})$ is 2.75.	129

90	Area $2\theta/\omega$ scan for a Ca/YBCO film. The peaks, from the left, are the YBCO (039), (309), and $\text{LaAlO}_3$ (303), respectively. Were $a$ -axis grains present, there would be another (309) peak at the same $2\theta$ value as the other but a positive $\omega$ value.	130
91	A $\psi$ scan for Ca/YBCO. The peak at $37^\circ$ represents $c$ -axis growth. There is no peak at $54^\circ$ , indicating no $a$ -axis-oriented material.	130
92	Resistivity vs. temperature for a Co/YBCO film on $\text{LaAlO}_3$ . There is metallic behavior from room temperature to $\sim 100$ K, then there is a rise in resistivity just above the transition.	132
93	I-V characteristic for a YBCO SNS edge junction measured at $T = 63.9$ K with a Co/YBCO barrier. Vertical axis is $V$ , horizontal $I$ , with $x = 200 \mu\text{A}/\text{division}$ .	132
94	I-V characteristic of same junction as in Figure 94, showing Shapiro steps as a result of the application of 9.9 GHz radiation. This was measured at 64.7 K, and $x = 200 \mu\text{A}/\text{division}$ .	133

## Introduction

The goal of this thesis work has been to produce BKBO and YBCO thin film superconductors for device applications and for study of their structural, chemical, and electronic properties. In Chapter I, several of the fundamental principles of superconductivity necessary for discussion of materials and devices are presented. Although the microscopic theory of high-temperature superconductors is still actively debated, the BCS theory is considered here to be the most relevant. This assumption appears to be well-justified for cubic BKBO and for YBCO, which is relatively isotropic compared to the higher temperature materials such as the Bi, Tl, and Hg compounds. Other pairing mechanisms and statistical mechanics of the superfluid condensation have been offered but still remain controversial and will not be discussed here. The BCS theory describes the nature of the attractive pairing between electrons and the condensation into the superfluid ground state.

Transport properties are considered both in the normal state and through the superconducting transition. The traditional role of impurities on normal-state properties and the superconducting transition is discussed. More importantly, deviations from linear behavior of normal-state resistivity as a function of temperature, which have been observed for BKBO and YBCO derivatives, are discussed in terms of a variable-range hopping model. The two-fluid model is offered as a means of discussing the superposition of current densities from both normal and superconducting electrons under ac conditions.

The magnetic properties of superconductors are described next, including experimental manifestations of the Meissner Effect and the distinction between Type

I and Type II superconductors. All of the oxide superconductors are high- $\kappa$  Type II superconductors with short ( $< 100 \text{ \AA}$ ) coherence lengths. The two superconducting length scales, the Ginzburg-Landau (and BCS) coherence length and the London penetration depth, are introduced. In high-temperature superconducting materials, novel H-T (magnetic field vs. temperature) phase diagrams have been observed with important experimental manifestations of phenomena such as flux lattice melting and 3D-2D vortex transitions. These are not, however, important for the materials studied in this project and are therefore not discussed. For the isotropic and lower-temperature superconductor BKBO, with a  $T_c$  of 34 K, these considerations are not necessary. For the more anisotropic YBCO material, manifestation of novel vortex phases are limited to temperatures very near the superconducting transition temperature and can therefore be ignored in most of the work considered here.

Tunneling phenomena associated with both electrons pairs and quasiparticles are considered next. This includes a discussion of energy level diagrams, circuit analogs, and I-V characteristics of SIS and SNS Josephson Junctions. The modulation of the tunneling current density in an applied field is discussed next. Finally, the applications of Josephson Junctions are summarized. One of the important goals of the research presented in this thesis has been the demonstration of interesting high-temperature superconducting devices, and particularly the fabrication of BKBO SIS trilayer junctions and YBCO SNS edge junctions; other geometries were not emphasized in this work. These types of junctions have mostly digital logic applications, so analog applications are introduced but are not considered any further.

The rest of the thesis is organized in the following manner: in Chapter II is a historical background of the discovery of superconductivity in metals and compounds and of the subsequent development of Josephson Junctions which utilize these compounds. A great deal of effort has been made in utilizing oxide superconductors in electronic devices. Of these, BKBO is the highest- $T_c$  material which is also isotropic. In addition, it has a relatively long coherence length (30-60 Å). All of these properties make it an interesting material for study. By contrast, YBCO has the advantages of a higher  $T_c$  and of having no volatile components. An introduction to the properties of BKBO and YBCO, the materials studied in this work, is then given.

The objectives of this research are discussed in Chapter III. This discussion includes a list of necessary junction properties and a description of experimental techniques used to measure these properties. Chapter IV contains an account of the methods and procedures used in film and junction growth and characterization and explanations of the physical principles involved in each technique. Experimental results for films and junctions are discussed in Chapter V, and conclusions are drawn and future research directions suggested in Chapter VI.

## Chapter I. Principles of Superconductivity

Superconductors have the unique properties of zero resistance and of magnetic flux expulsion from their interiors, both of which are observed for temperatures below the superconducting transition temperature,  $T_c$ . The resistanceless state has been described in many theories. The most comprehensive and widely accepted of these, however, is the Bardeen-Cooper-Schrieffer (BCS) theory. The BCS theory describes an attractive interaction between electrons which is mediated by an electron-phonon interaction. This theory is applicable to isotropic superconductors. In these materials, the electrons condense into a superfluid state in which they are paired. Upon excitation, the pairs split and the electrons become normal. A simple two-fluid model is often employed to describe the currents carried by both superconducting and normal electrons under ac conditions.

In conventional superconductors, two types of behavior are observed with respect to magnetization behavior. The behavior is dependent upon the sign of the interfacial energy between the superconducting and normal regions. If the interfacial energy is positive, the flux entering the superconducting sample for fields exceeding the thermodynamic critical field,  $H_c$ , causes the abrupt loss of superconductivity, which is characteristic of type I response. By contrast, a negative interfacial energy stabilizes the vortex state above a lower critical field,  $H_{c1}$ , with the eventual loss of superconductivity at the upper critical field,  $H_{c2}$ , in a type II superconductor. In Ginzburg-Landau theory, the distinction between type I and type II superconductivity depends on the ratio of two characteristic length scales, the London penetration depth,  $\lambda$ , and the coherence length,  $\xi$ . When the ratio  $\kappa = \lambda/\xi$  is  $> 1/\sqrt{2}$ , type II superconductivity is observed, while type I superconductivity is seen for  $\kappa < 1/\sqrt{2}$ .

## A. Bulk properties

### 1. Cooper pairing, concept of electron-phonon interaction, and the BCS energy gap

The concept of an electron-phonon interaction in superconductors was first proposed by Fröhlich in 1950. He suggested that the electron-phonon interaction was capable of coupling two electrons together through the emission of a phonon from a first electron and subsequent absorption by a second [1]. R.A. Ogg was the first to suggest that superconducting electrons form pairs, but his chemical theory did not gain acceptance [2]. Cooper later gave a physical basis for pairing. He demonstrated that when two electrons are added to a metal at zero temperature, they are forced to occupy states outside the Fermi sphere by the Pauli Exclusion Principle, but if there is an attractive potential coupling the electrons, their total energy will be less than  $2E_F$  (where  $E_F$  is the Fermi energy of the metal) [1]. His treatment involved only two electrons, which was further refined in 1957 by Bardeen, Cooper, and Schrieffer to apply to a many-electron system. The three won the Nobel Prize for this work in 1972. BCS theory explains how the residual effective positive charge left by the first electron-phonon interaction attracts the second electron of opposite momentum, thus creating a resistanceless path for the Cooper pairs. This theory also proposes a ground state, which contains the superconducting electrons, or Cooper pairs, separated from excited states, which contain the normal electrons, or quasiparticles, by an energy gap. This gap represents the energy to split apart the coupled electrons and has been unambiguously observed in the lower- $T_c$  superconductors. The BCS gap energy can be related to the density of states,  $N_0$ , and the electron-lattice interaction potential,  $V_0$ , by [3]:

$$\Delta(0) = 2\hbar\omega e^{-(1/N_0 V_0)} \quad (1)$$



where  $\hbar = \text{Planck's constant}/2\pi$  and  $\omega$  is the phonon frequency. The relationship for the critical temperature,  $T_c$ , in zero magnetic field results from a statistical mechanical treatment of the Bose condensation and is of a similar form:

$$kT_c = 1.13\hbar\omega e^{-(1/N_0V_0)} \quad (2)$$

The ratio of these yields  $2\Delta(0)/kT_c = 3.52$  and gives an estimate of the strength of the electron-phonon coupling. Note that the energy to overcome the gap is  $2\Delta$  since there are two electrons in a Cooper pair which traverse the gap when excited. The BCS temperature dependence of the gap is given by the relation [3]:

$$\Delta(T)/\Delta(0) = 1.74 (1 - T/T_c)^{1/2} \quad (3)$$

for  $T$  near  $T_c$ . It can be seen from Figure 1 that below about  $0.6T_c$ , the gap is essentially independent of temperature. Above this value, the specific heat of the superconductor rises rapidly with temperature because  $d\Delta(T)/dT$  diverges as  $T$  approaches  $T_c$ . The energy  $2\Delta$  required to split a Cooper pair is reduced as the gap becomes smaller. Above  $T_c$ , no energy is required for pair splitting, so there is an abrupt decrease in the specific heat with increasing temperature [1].

Another consequence of electron-phonon interaction in superconductors is that they exhibit an isotope effect. It has been observed that the critical temperature of superconductors varies with isotopic mass in a relation of the form  $M^\alpha T_c = \text{a constant}$ . This is a result of the direct proportionality of  $T_c$  to  $\Theta_D$ , the Debye temperature of the lattice, which in turn is proportional to  $\hbar k(K/M)^{1/2}$ , where  $K$  = the spring constant of the lattice,  $M$  = the isotope mass, and  $k$  is a phonon wavevector. In the original BCS model,  $\alpha = 1/2$ , but if Coulombic interactions are

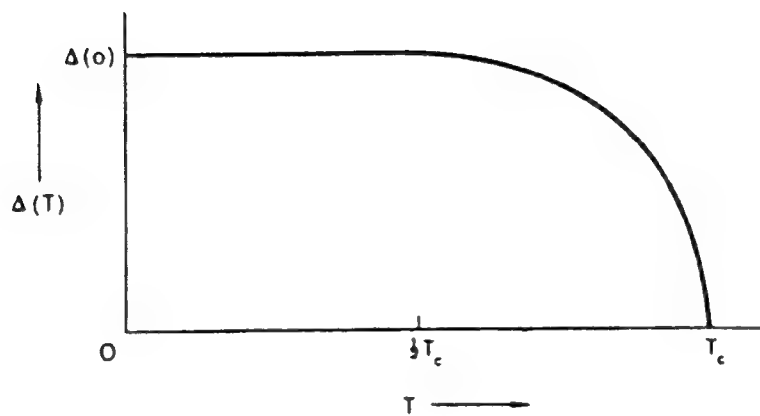


Figure 1. Dependence of the superconducting gap on temperature. The gap is zero at the transition temperature,  $T_c$  [1].

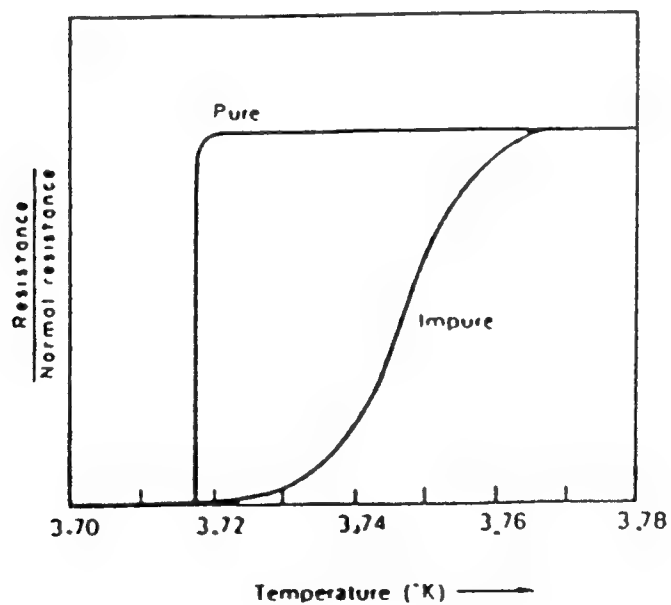


Figure 2. Superconducting transitions in pure and impure tin. Impure materials have much broader transitions [5].

considered, phonon frequencies are "dressed" and the exponent changes. Observed values of  $\alpha$  actually range from  $0.32 \pm 0.07$  in Cd to  $0.61 \pm 0.10$  in Tl [4]; in some elemental superconductors,  $\alpha$  is zero, and in some alloy superconductors, it is negative.

## 2. Resistive transition, variable-range hopping conduction, and the two-fluid model

In addition to the pairing of electrons, there are two properties that distinguish superconductors from other materials. The first is the lack of resistance. The resistance of a pure material will drop precipitously as the material approaches its superconducting transition temperature,  $T_c$ , as shown in Figure 2. If the material is impure, however, the resistance will drop gradually, which is shown in Figure 2 as well. The transition for the impure material is broader;  $T_c(\text{onset})$  occurs at 3.76 K, whereas  $T_c(R=0)$  occurs at 3.72 K. Above the transition temperature, superconductors tend to exhibit metallic behavior. If the  $\rho$  vs.  $T$  line were extrapolated beyond the transition, the slope should be such that the line would intersect (0,0) for a pure material. This is not always the case, however. In some superconductors, variable-range hopping occurs; in such a case,  $\rho$  rises as temperature is lowered until the superconducting transition is reached.

Variable-range hopping conduction is observed in lightly-doped and strongly-compensated heavily-doped semiconductors. In the former case, the average distance between impurities,  $N^{-1/3}$  (where  $N$  = impurity concentration), is greater than the Bohr radius,  $a$ , of the impurity so that  $Na^3 \ll 1$ . Heavy doping implies that  $Na^3 \gg 1$ . Very heavy doping without compensation leads to metallic conduction with little variation in carrier concentration with temperature [6].

If the temperature is relatively high in a compensated semiconductor, the electrons can acquire enough thermal energy to overcome the potential barriers

between them. The electrons are excited from donor impurity levels to the conduction band. When the temperature is lowered, the conduction mechanism is one of electrons "hopping" from donor to donor. "Hopping" occurs by electrons tunneling from one potential well to another. These hops are possible because of the overlap of neighboring impurity state wave functions [6]. The probability of such a jump occurring is proportional to the square of the modulus of the overlap integral of the wave functions of the ground state of an electron at each of the donors [7].

The following argument by Mott [8] gives an explanation for the  $T^{-1/4}$  dependence of the resistivity at very low temperatures:

Thermally activated hopping occurs when an electron in a state with energy below the Fermi energy ( $E_F$ ) receives sufficient energy from a phonon for excitation to a state above  $E_F$ . Thermally activated hopping conductivities are described by the Arrhenius relation:

$$\sigma = \sigma_3 \exp(-\epsilon_3/kT) \quad (4)$$

where  $\epsilon_3$  is an energy barrier to hopping of the form:

$$\epsilon_3 \sim 1/N(E_F)a^3 \quad (5)$$

where  $a$  is the distance between nearest neighbors and  $N(E_F)$  is the density of states per unit volume at the Fermi level. The density of states in a sphere of radius  $R$  for energies near the Fermi energy is  $(4\pi/3)R^3N(E_F)$  per unit energy. At low temperatures, hopping need not be to a nearest neighbor; the activation energy,  $\Delta E$ , will be smaller if the electron hops farther since

$$\Delta E = 1/(4\pi/3)R^3N(E_F) \quad (6)$$

Hopping over a large distance has a lower probability, however, since tunneling is the hopping mechanism and the probability is proportional to  $\exp(-2\alpha R)$ , where  $1/\alpha$  is the decay length of the localized wave function. The parameter  $\alpha$  is on the order of

$k_F$ , which is the magnitude of a wavevector at the Fermi surface. The optimum hopping distance  $R$  is that for which:

$$\exp(-2\alpha R)\exp(-\Delta E/kT) \quad (7)$$

is a maximum. This occurs when:

$$2\alpha R + 1/\{(4\pi/3)R^3N(E_F)kT\}=0 \quad (8)$$

for which the maximum  $R$  value is:

$$R = \{1/8\pi N(E_F)\alpha kT\}^{1/4} \quad (9)$$

Substituting the expression in (9) for  $R$  in equation (8) yields a hopping probability and therefore a conductivity of the general form  $A \exp(-B/T^{1/4})$ , where  $B=2(3/2\pi)^{1/4}\{\alpha^3/kN(E_F)\}^{1/4}$ .

Below the transition temperature, a superconducting material is resistanceless under dc conditions, for which all of the current is carried by Cooper pairs. There is no current carried by the normal electrons without an electric field to drive their movement. In an alternating field, however, both normal and superconducting electrons carry current, which can be represented by a two-fluid model. There is a resulting resistance from scattering of the normal electrons. In addition, the superelectrons possess a small inertial mass which causes them to lag behind the field and to thus present an inductive impedance [5].

### 3. Meissner effect, Type I and II superconductivity, and length scales

The second distinguishing feature of superconductors is the expulsion of magnetic flux from their interior. All superconductors become normal if their critical temperatures or critical currents are exceeded. All will expel flux from their interiors by generating currents which circulate on the surface of the material and oppose any

change in applied magnetic field when below the thermodynamic critical field. This is true whether the superconductor was cooled in a magnetic field or not. There are two types of behavior observed in superconductors when the critical field is exceeded, however. Elemental metallic superconductors exhibit an equilibrium magnetization curve such as that in Figure 3(a) and are known as Type I superconductors. When the critical field of a Type I material is exceeded, it becomes normal. Type II superconductors tend to be alloys or transition metals with short electronic mean free paths in the normal state. These materials are perfectly diamagnetic up to  $H_{c1}$ , the lower critical field. Above  $H_{c1}$ , magnetic flux enter the superconductor, forming a periodic array of vortices until  $H_{c2}$ , the upper critical field, is reached and the superconductor becomes a normal conductor due to vortex overlap [4]. The equilibrium magnetization curve for a Type II superconductor is depicted in Figure 3(b).

Ginzburg-Landau theory describes the change in upper critical field with temperature. This can be used to calculate the coherence length,  $\xi$ , which is the exponential decay length over which the superconducting wavefunction decreases at the interface with a normal conducting region as shown in Figure 4. The equation used to calculate  $\xi$  is given below [10]:

$$\left. \frac{-dH_{c2}}{dT} \right|_{BCS} = \frac{\hbar c}{2e} \frac{1}{\xi_{GL}^2(0)} \frac{1}{T_c} \quad (10)$$

where  $H_{c2}$  = upper critical field,  $\hbar$  = Planck's constant/ $2\pi$  =  $1.055 \times 10^{-27}$  erg•sec,  $c$  = speed of light =  $2.998 \times 10^{10}$  cm/sec,  $e$  = electron charge =  $4.803 \times 10^{-10}$  esu, and  $\xi_{GL}(0)$  = zero-temperature Ginzburg-Landau coherence length. The extent to which the magnetic flux penetrates the superconductor, i.e., the length of the normal

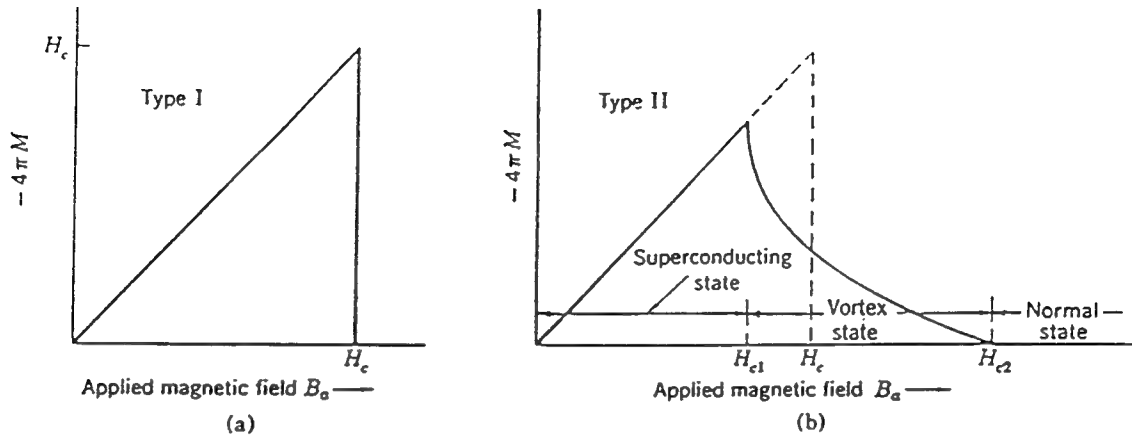


Figure 3. Magnetization versus applied field for (a) a Type I superconductor, which becomes normal as soon as  $H_c$  is reached, and for (b) a Type II superconductor, which is in a flux vortex state between  $H_{c1}$  and  $H_{c2}$  and then is normal above  $H_{c2}$ . The area under both curves is the same for a given  $H_c$  [4].

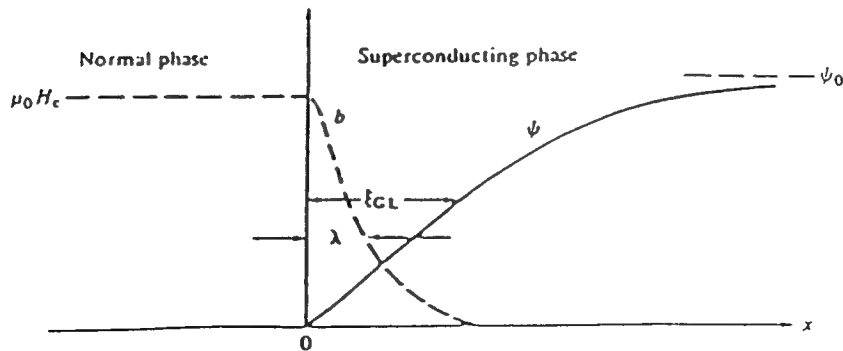


Figure 4. Superconductor coherence length,  $\xi$ , and normal-phase penetration depth,  $\lambda$ , at a superconductor/normal phase interface [9].

phase in the superconducting material, is designated  $\lambda$ , the London penetration depth. This length is depicted in Figure 4 and originates in the following manner:

In a superconductor, the superconducting electrons encounter no resistance and are therefore accelerated steadily in a constant electric field  $E$ :

$$m(dv/dt) = eE \quad (11)$$

where  $v$  = velocity of the superelectrons,  $m$  = mass of electrons, and  $e$  = charge of electrons. The supercurrent density  $J$  will then be

$$J = nev \quad (12)$$

where  $n$  = the number of superelectrons per unit volume. Differentiating (12) and substituting it into (11) gives

$$dJ/dt = ne^2E/m \quad (13)$$

From Maxwell's equations, if one considers the displacement current to be negligible in comparison to  $J$  and if one assumes that currents in the superconductor affect  $B$  but not  $H$ , one can write

$$\text{curl } B = \mu_0 J \quad (14)$$

substituting this into equation (13) gives

$$dB/dt = (-m/ne^2) \text{curl } dJ/dt \quad (15)$$

It can also be argued that

$$B = (-m/ne^2) \text{curl } J \quad (16)$$

Equations (13) and (16) are the London equations; the former describes the resistanceless state of the superconductor, because there is no electric field inside unless the current is changing, and the latter describes the diamagnetism. A result of these is that one finds that if a uniform magnetic field of flux density  $B_a$  is applied parallel to the surface, the flux density at a distance  $x$  inside,  $B(x)$ , will be



$$B(x) = B_a \exp \left( \frac{-x}{\sqrt{\frac{m}{\mu_0 n e^2}}} \right) \quad (17)$$

Equation (17) shows that the flux density dies away exponentially inside the superconductor. At a distance

$$\lambda = \sqrt{\frac{m}{\mu_0 n e^2}} \quad (18)$$

the flux density will be 1/e of its value at the surface. The distance  $\lambda$  is referred to as the London penetration depth [11]. The value of  $\lambda$  can be calculated knowing the values of the lower and upper critical fields and the coherence length [12]. The coherence length and penetration depth are very important parameters in Josephson junctions. For example, if the junction barrier exceeds the superconducting coherence length, there will not be a supercurrent across the junction.

## B. Josephson junctions

### 1. Tunneling phenomena in SIS junctions

The barrier in a Josephson junction can be an insulating material (an SIS junction) or a normal conducting material (SNS junction). Superconducting materials which have well-defined gaps are used in SIS junctions. Conduction through the barrier of such junctions occurs by electron and pair tunneling. Both quasiparticles and superconducting electrons may tunnel if the barrier is thin enough (15-20 Å), although the probability of single-particle tunneling is greater because the matrix element for simultaneous tunneling of two electrons will depend on the square of that for single-particle tunneling. However, the magnitude of the single-particle tunneling current decreases exponentially with temperature because quasiparticles are normal electrons and obey Fermi-Dirac statistics. Cooper-pair tunneling is independent of temperature, because there is an infinite reservoir from which to draw them due to the Bose-Einstein condensation. Consequently, there is a greater probability of observing two-particle tunneling at lower temperatures than at higher ones. Similarly, by reducing the barrier thickness, the proportion of two-particle to single-particle tunneling should increase [13].

Tunneling of electron pairs through a barrier was first predicted by Brian Josephson as a graduate student in 1962 [14]. He won the Nobel Prize in Physics in 1973 for his efforts. The result of that work is that the current density through the junction will be given by:

$$J = J_C \sin \phi \quad (19)$$

where  $\phi$  is the phase difference between the two wavefunctions on either side of the junction. It is important to note that because a maximum occurs when  $(\sin \phi) = 1$ , the greatest current flow across the junction will occur when the two wavefunctions

are out of phase with each other by  $\pi/2$ . It should also be noted that this current flow occurs without the application of any bias voltage. If a voltage is applied, the Cooper pairs will radiate their excess energy by becoming oscillators [2].

By contrast, a bias voltage is necessary to cause quasiparticle tunneling. At 0 K, all of the electrons are superconducting, and the band diagram and density of states for two identical superconductors separated by a thin insulator is shown in Figure 5. If a voltage is applied to the system, there will be no current flow until the voltage difference is as large as the gap itself, when quasiparticles, which are formed from the splitting of Cooper pairs, can tunnel from the "valence" band (condensed superelectron states) shown on the left in Figure 6 into the available states of the "conduction" band (excited quasiparticle states) on the right. There will then be a sharp rise in current, as shown in the I-V characteristic in Figure 7. The vertical line at zero voltage depicts the critical current due to Cooper pair tunneling. At finite temperatures, there will be some thermally excited electrons which can tunnel into empty states when some voltage lower than the gap voltage,  $2\Delta/e$ , is applied. The quasiparticle I-V curve then has some curvature, as shown in Figure 8.

If the two superconductors have different gaps, such as those in Figure 9(a), the behavior is altered. At thermal equilibrium and some finite temperature, there will be some thermally excited electrons (quasiparticles) on either side of the insulator, although there will be more in superconductor 1 (left side) because it has a smaller gap. An applied voltage will cause a current to flow, and more thermally excited electrons in superconductor 1 will tunnel across to available states in superconductor 2. This occurs until the applied voltage is equal to  $(\Delta_2 - \Delta_1)/e$  (Figure 9(b)), when the current begins to decrease because the number of electrons capable of tunneling is unchanged but the density of available states is lower. When the voltage becomes equal to  $(\Delta_1 + \Delta_2)/e$ , however, as in Figure 9(c), current begins to increase rapidly, because electrons below the gap can begin to tunnel. The I-V

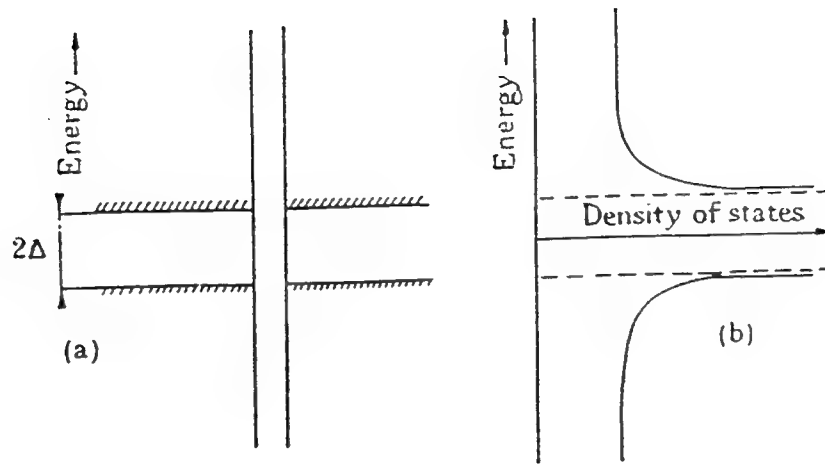


Figure 5. (a) Energy band diagram for two identical superconductors separated by a thin insulator. (b) Density of states for the superconductor [2].

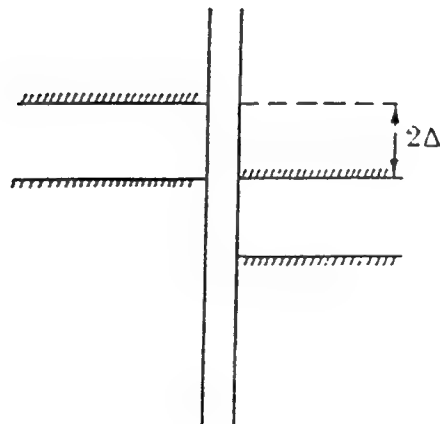


Figure 6. Energy band diagram for two identical superconductors and an insulator with an applied voltage of  $2\Delta/e$  [2].

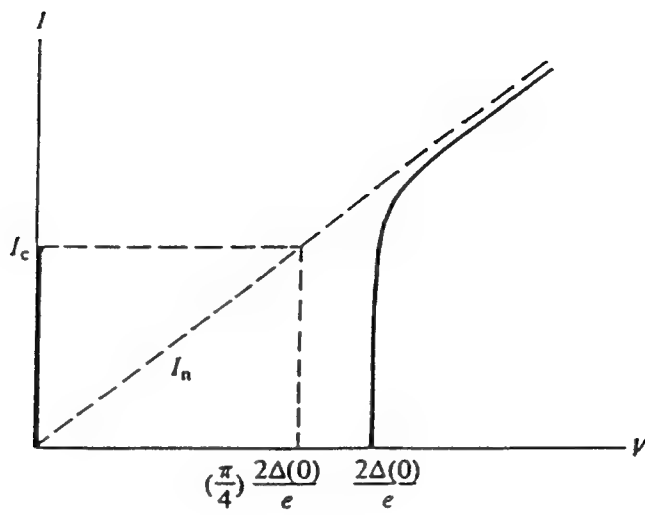


Figure 7. I-V characteristic for an SIS Josephson junction at  $T=0$  [15].

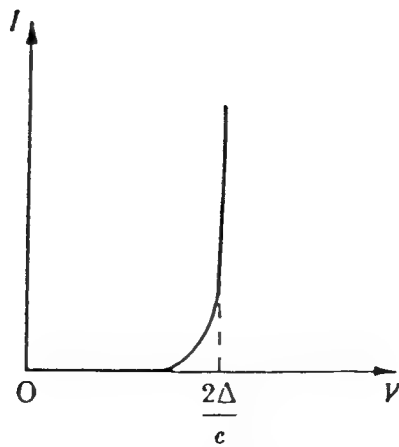


Figure 8. I-V characteristic for an SIS Josephson junction at  $T>0$  [2].

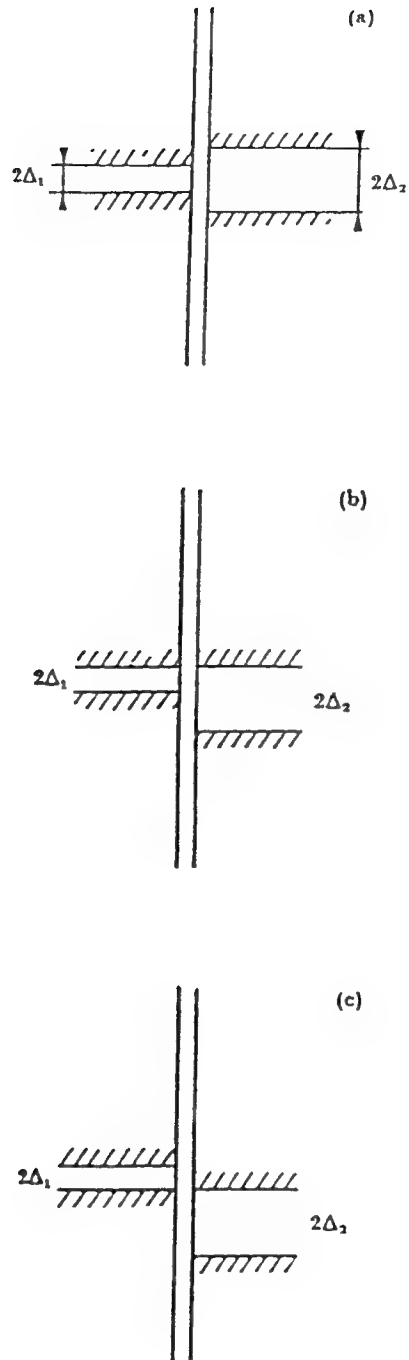


Figure 9. Energy band diagram for two different superconductors separated by a thin insulator at (a)  $V=0$  (b)  $V=(\Delta_2-\Delta_1)/e$  (c)  $V=(\Delta_1+\Delta_2)/e$  [2].

characteristic for this system is shown in Figure 10.

## 2. Circuit analog

When a resistor is placed in parallel with an SIS junction, the circuit will have the same I-V curve as an SNS junction (see Figure 11). The circuit equivalent of these constitutes the RSJ model (resistively-shunted junction) which has a current given by

$$I = I_c \sin \phi + GV + C(dV/dt) \quad (20)$$

and is shown in Figure 12. The mechanical analog of this model is that of a swinging pendulum. The torque on the pendulum is analogous to the current flow through the junction. The critical current of the junction is similar to the gravitational force which drives the pendulum, the capacitance can be compared to a moment of inertia which determines response time, and the resistance acts as a damping constant in a viscous medium. When the pendulum is at  $90^\circ$  from the vertical position, there is enough torque on it to flip it over, which is analogous to switching voltage states from "0" to "1".

## 3. SNS junctions

Conductivity through an SNS junction occurs by the proximity effect, in which superconductivity is induced in the normal conducting material by the superconducting electrodes on either side. The barrier must be thin enough so that overlap of the wavefunctions occurs. A schematic of the variation of the wavefunction through the SNS junction is shown in Figure 13. The decay length of the superconducting wavefunction in the normal region, denoted  $\xi_N$ , is inversely proportional to the

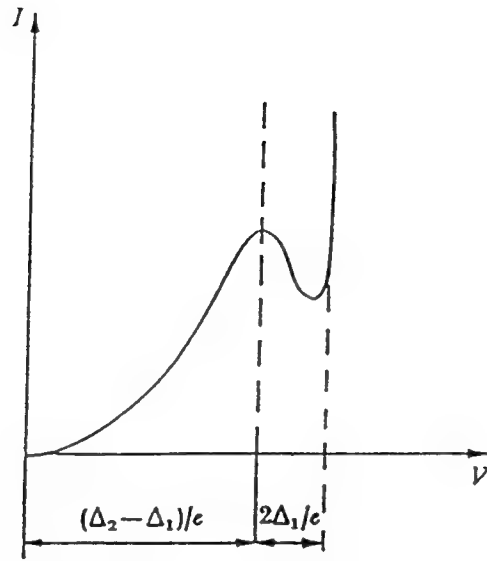


Figure 10. I-V characteristic for two different superconductors separated by a thin insulator. There is a negative resistance region for  $(\Delta_2 - \Delta_1)/2e < V < (\Delta_1 + \Delta_2)/2e$  [2].

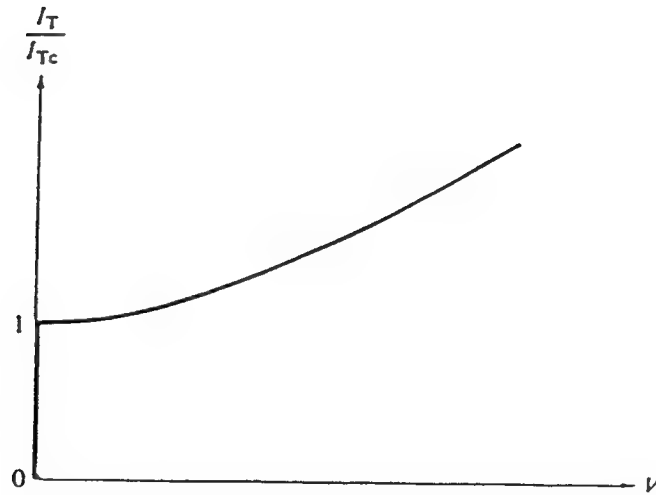


Figure 11. I-V characteristic for an SNS Josephson junction [16].



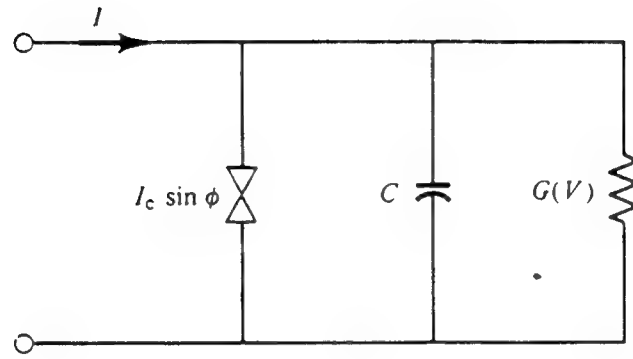


Figure 12. The circuit equivalent for a Josephson junction [17].

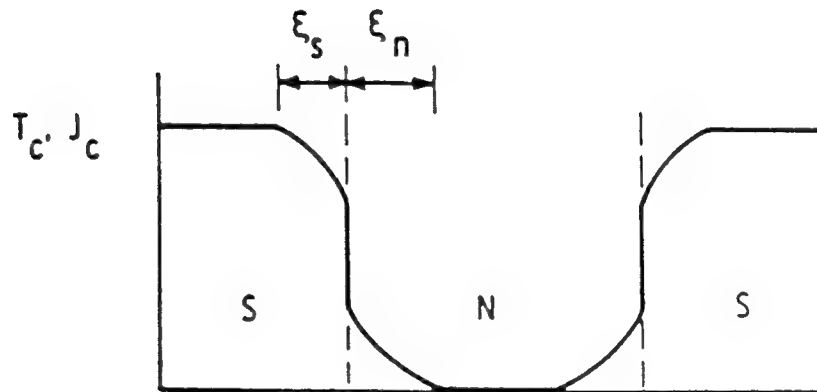


Figure 13. Schematic of the spatial dependence of  $T_c$  and  $J_c$  vs. the superconducting wavefunction for an SNS junction [18].

resistivity of the normal region, so it is desirable to use highly conductive materials for the barrier. This allows the use of a thicker barrier.

#### 4. Magnetic field effects

Josephson junctions are characterized with respect to their overall dimensions as being "short" or "long". Short means that the junction is small enough that the current is uniform across the junction and there are no self-field effects. In a junction, the critical current density tends to be on the order of  $10^3$  A/cm<sup>2</sup>, as opposed to  $10^6$  A/cm<sup>2</sup> in films. A larger area, with linear dimensions exceeding the Josephson penetration depth, is needed to obtain a high enough current across the junction to nucleate a vortex. This will occur in long junctions or if a magnetic field is applied to short junctions. In the latter case, the maximum current will have the form [19]:

$$i = I_c \left| \frac{\sin \pi \frac{\Phi_J}{\Phi_0}}{\pi \frac{\Phi_J}{\Phi_0}} \right| \quad (21)$$

where  $\Phi_J$  = flux through the junction and  $\Phi_0$  = a flux quantum =  $\pi\hbar c/e = 2.1 \times 10^{-7}$  gauss·cm<sup>2</sup>. The current density distribution for varying applied magnetic fields across a short junction is shown in Figure 14, and the resulting junction response of current vs. applied field is shown in Figure 15. The latter is analogous to a single slit, Fraunhofer diffraction pattern. A long Josephson junction will incur self-field effects, which will introduce Josephson vortices. These vortices are distinguished from Abrikosov vortices in that they do not possess normal cores, but the supercurrent in their centers is zero and they do dissipate energy when they move. The current

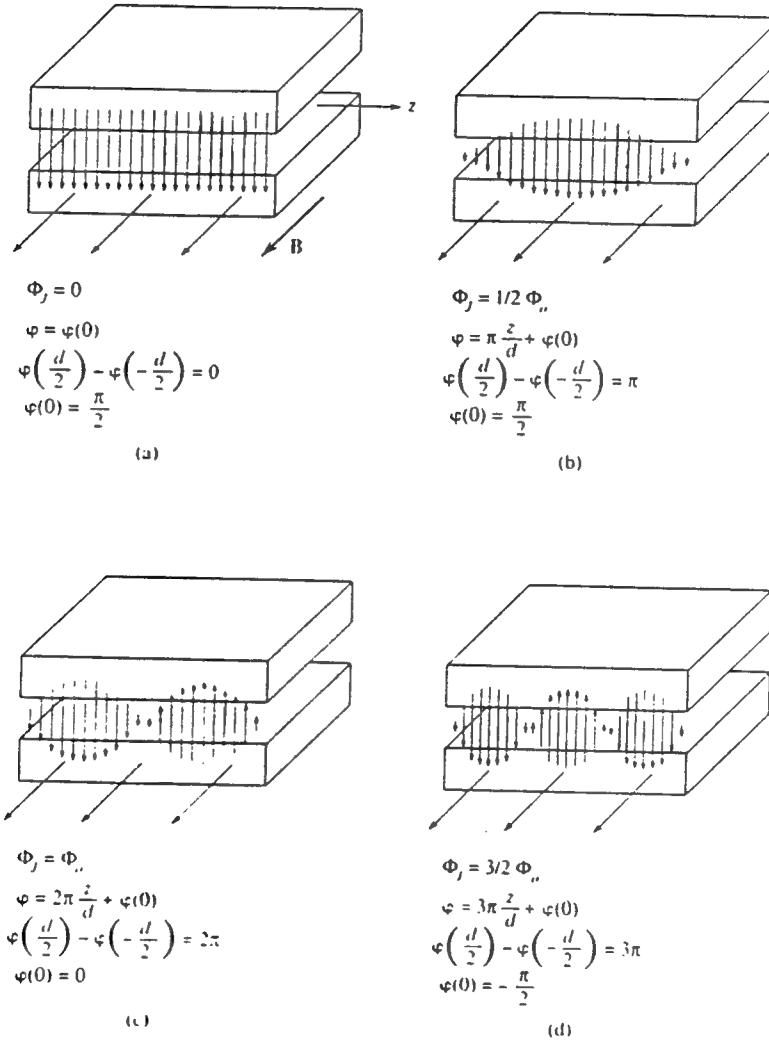


Figure 14. The current density distribution for a single, short Josephson junction with an applied magnetic field. The current density is maximized in each case.  $\Phi_J$  is the flux in the junction,  $\Phi_0$  a flux quantum,  $d$  the length of the junction, and  $\varphi$  the phase difference [19].

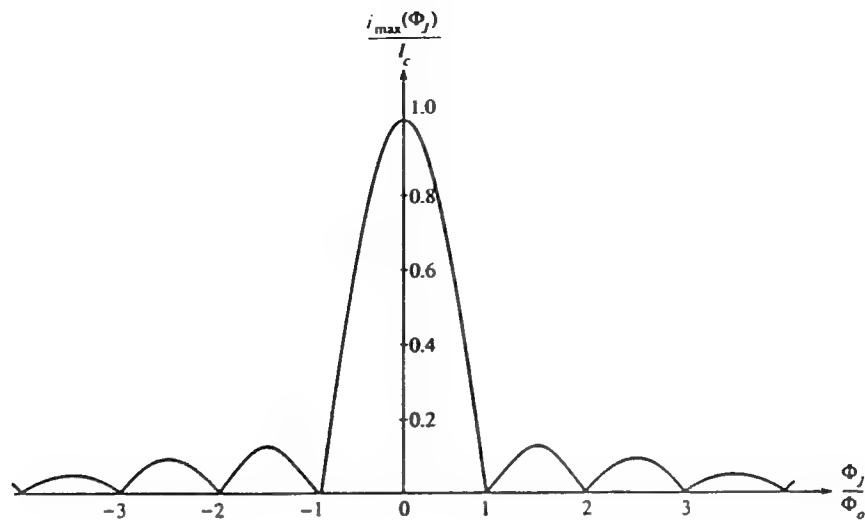


Figure 15. Current vs. applied magnetic field response of a single, short Josephson junction with no self-fields [19].

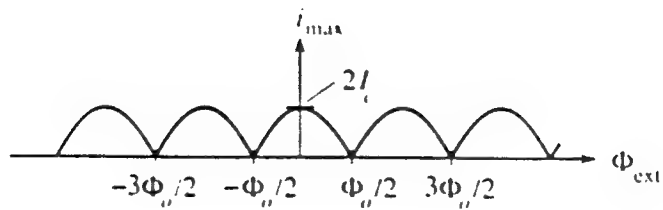


Figure 16. Current vs. magnetic field response of a SQUID [19].

distribution shown in Figure 14(d) is similar to that in a long Josephson junction, although there would be more nodes and regions of reversed current, so that the circuit equivalent would be one of many Josephson junctions in parallel. Such a configuration simulates the behavior of a SQUID (superconducting quantum interference device) loop, which has the same current density no matter how many integral multiples of a flux quantum are present in the loop. This is because the maximum supercurrent is a periodic function of the magnetic flux and is given by:

$$i_{\max} = 2I_c \left| \cos\left(\frac{\pi\Phi_{\text{ext}}}{\Phi_0}\right) \right| \quad (22)$$

A superconductor with a hole, upon being cooled in a magnetic field, will have currents which circulate around the periphery of the hole in the opposite direction of those on the outer surface of the superconductor. The superconducting loop will have no flux in its interior, but flux will be trapped in the hole when the field is turned off. This is how a flux quantum is introduced into a superconducting loop such as a SQUID, which causes the device to switch from a 0 to a 1 voltage state. The trapped flux is always an integral multiple of a flux quantum irrespective of the initial value of the applied field [20]. The current vs. magnetic field response for such a junction is shown in Figure 16.

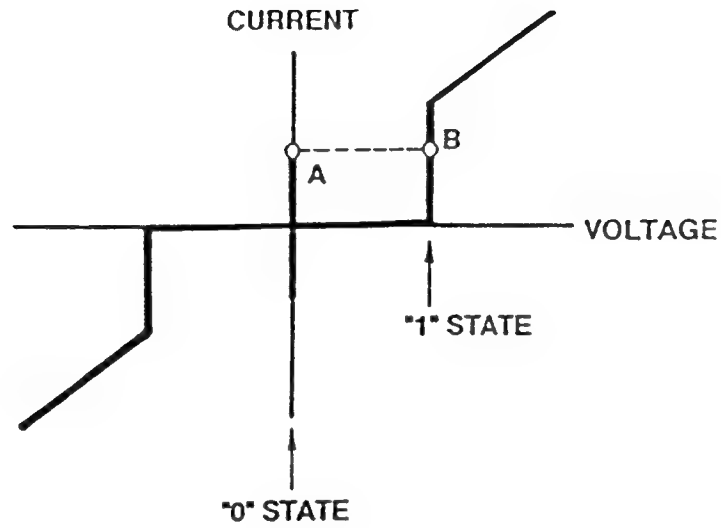
## 5. Applications

Josephson junctions have switching times typically in the picosecond range, which is three orders of magnitude faster than standard CMOS (semiconductor) devices. In addition, superconducting devices pass current at millivolt levels as compared with the several volts required for semiconducting devices. This 1000:1 voltage ratio means that semiconductor circuits require thousands of times more

power to operate, which not only costs more but also creates a great deal of heat, which is a major concern in densely-packed circuits. Superconductors dissipate less heat and are operated at much lower temperatures, thus offering the advantage of closer proximity on a circuit board. Their lack of resistance and operation at lower temperatures results in less electronic noise than that found for semiconductors. However, because of the higher levels of integration of silicon technology (there are 100 times more active devices in silicon microprocessors as in Josephson ones) as well as the lack of a credible superconducting memory [21], it would be advantageous to integrate the two technologies, by fabricating hybrid systems (superconducting device/semiconducting memory) as well as hybrid circuits (Josephson junction/CMOS). This has been demonstrated for superconducting flux flow devices used as read-outs for CMOS memory cells, for which a 4.5-ns access time was obtained [22].

- Applications for Josephson junctions include both analog and digital technologies (as well as A/D converters and as a basis for the standard volt). Digital technology includes latching logic (0 or 1 voltage output) as shown for SIS and SNS junctions in Figure 17 and also single-flux quantum logic, which is used in SQUID loops (for shift registers, magnetometers, magnetoencephalography, etc.). It also includes MVTL (modified variable threshold logic), which is used in shift registers, and SAIL (Series Array Interferometer logic). Analog applications of superconductors include mixers, in which two frequencies applied to a nonlinear I-V curve will generate harmonics at sum frequencies, allowing conversion and detection of radiation, as in radio astronomy; oscillators; x-ray detectors; and bolometers, which are thermometers based on changes in resistance as a function of temperature. Superconductive components are also used in microwave circuits, as antennas, and in transmission and delay lines because of their small losses [24].

(a)



(b)

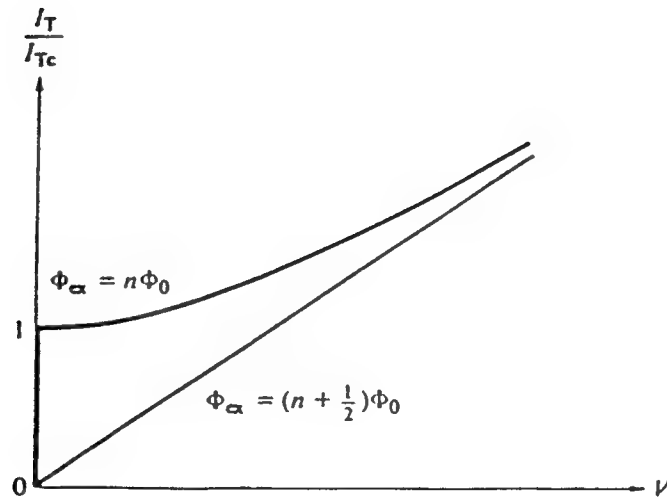


Figure 17. (a) I-V characteristic of an SIS Josephson junction, showing "zero" and "one" states [23] (b) I-V characteristic of a SQUID loop for integer and half-integer multiples of the flux quantum in the loop, showing "zero" and "one" states [16].

## Chapter II. Literature Review

### A. Historical background of superconductivity

Superconductivity was first observed by Heike Kamerlingh Onnes in 1911. He used liquid helium, which he was the first to liquefy in 1908, to cool mercury to 4.2 K and observed a disappearing resistance. To his surprise, the resistance disappeared altogether (or to within experimentally determinable values of zero resistance). The next year, he discovered superconductivity in tin (at 3.7 K) and lead (7.2 K). Work was continued until it was found that over one-fourth of the elements superconduct. Niobium was found to have the highest  $T_C$  of 9.5 K among elemental superconductors [4].

With the subsequent synthesis of superconducting alloys, of which there are now thousands, niobium compounds were regarded with a great deal of interest because of the high  $T_C$  of the element. In 1930, Walther Meissner found superconductivity above 10 K in NbC. Superconductivity in NbN at 16 K was first reported in 1941. As the number of known superconducting alloys increased, Bernd Matthias developed a set of empirical rules from compounds synthesized in the 1950's and found that the number of valence electrons in the atoms of the material was very significant. Materials with averages of five and seven electrons-per-atom resulted in the highest-temperature superconductors [25]. The combination of this knowledge with the observation that certain high-symmetry crystal structures, such as the "A15" structure, shown in Figure 18, exhibited higher  $T_C$ 's, led to a great deal of activity in the 1960's and 1970's to optimize alloy chemistry. This led scientists to break the 20 K limit, which allowed the use of liquid hydrogen rather than liquid helium as a coolant. In 1973, a Nb<sub>3</sub>Ge thin film was synthesized by John Gavalier of



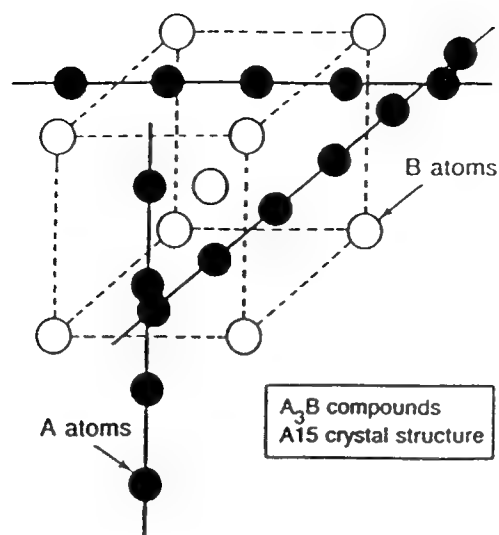


Figure 18. The A15 crystal structure for  $A_3B$  compounds [26].

Westinghouse using sputtering [27]. This compound becomes superconducting at 23 K, and it remained the highest- $T_C$  superconductor until 1986.

It was in that year that a  $T_C$  of 35 K was obtained by Johannes Bednorz and Karl Müller in  $La_{1.85}Ba_{0.15}CuO_4$ . This created quite a stir, but the subsequent discovery by C.W. Paul Chu and coworkers in January 1987 that  $YBa_2Cu_3O_7$  became superconducting at 93 K, above the liquefaction temperature of nitrogen, led to an explosion of new and renewed interest in the field. Transition temperatures were then raised to 110 K with  $Bi_2Sr_2Ca_2Cu_3O_{10}$  and 125 K with  $Tl_2Ba_2Ca_2Cu_3O_{10}$ . Recently, superconductivity at 250 K in a multilayer Bi-Sr-Ca-Cu-O compound with eight  $CuO_2$  layers in each building block was announced [28]. A drop in resistivity at 250 K was seen as well for two  $HgBa_2Ca_{n-1}Cu_nO_{2n+2+d}$  compounds, Hg-1223 and Hg-1245, implying that they or another phase present may become superconducting at this temperature [29].

During the search for new superconducting compounds with higher transition temperatures, studies of the oxides became prevalent. The oxide superconductors with  $T_C$ 's below 15 K, which were mostly discovered between 1964 and 1975, are listed in Table I. The  $BaBi_{1-x}Pb_xO_3$  system is the most notable of those listed.

Table I. Oxide Superconductors with  $T_c$  below 15 K [29]Oxide superconductors with  $T_c$  below 15 K\*

Compound	$T_c$ (K)	Synthesis method
NbO	1.4-1.6	Normal
TiO	0.7-1.1	Normal
SrTiO <sub>3-x</sub>	0-0.5	Normal
Na <sub>0.3</sub> WO <sub>3</sub> (tetragonal)	0.5	Normal, electrodeposition
Na <sub>0.2</sub> WO <sub>3</sub> (tetragonal)	3.0	Normal, electrodeposition
Ca <sub>0.1</sub> WO <sub>3</sub> (hexagonal)	3.4	Normal
Sr <sub>0.08</sub> WO <sub>3</sub> (hexagonal)	4.0	Normal
Ba <sub>0.14</sub> WO <sub>3</sub> (hexagonal)	2.2	Normal
In <sub>0.11</sub> WO <sub>3</sub> (hexagonal)	2.8	Normal
Tl <sub>0.30</sub> WO <sub>3</sub> (hexagonal)	2.1	Normal
K <sub>0.30</sub> WO <sub>3</sub> (hexagonal)	5.7	Deintercalation
Rb <sub>0.30</sub> WO <sub>3</sub> (hexagonal)	6.6	Deintercalation
Cs <sub>0.30</sub> WO <sub>3</sub> (hexagonal)	4.8	Deintercalation
Li <sub>0.30</sub> WO <sub>3</sub> (hexagonal)	2.2	Normal
Na <sub>x</sub> WO <sub>3</sub> (hexagonal)	5.4	Normal
(NH <sub>4</sub> ) <sub>0.33</sub> WO <sub>3</sub> (hexagonal)	3.2	Normal
K <sub>x</sub> MoO <sub>3</sub> (tetragonal)	4.2	High pressure
K <sub>x</sub> ReO <sub>3</sub> (hexagonal)	3.6	High pressure
Li <sub>0.9</sub> Mo <sub>6</sub> O <sub>17</sub>	~2	Normal
Li <sub>0.45</sub> NbO <sub>2</sub>	5.5	Deintercalation
Ag <sub>7</sub> O <sub>8</sub> X (X = NO <sub>3</sub> , HF <sub>2</sub> , ClO <sub>4</sub> , BF <sub>4</sub> )	1.4	Electrodeposition
LiTi <sub>2</sub> O <sub>4</sub>	13.7	Normal
BaBi <sub>1-x</sub> Pb <sub>x</sub> O <sub>3</sub>	13	Normal

\*Superconductors with an oxygen-to-metal ratio of less than 1 are not listed.

Studies of this compound by Arthur Sleight and coworkers showed that superconductivity existed in the Pb-rich composition range  $0.05 \leq x \leq 0.3$  in  $\text{BaPb}_{1-x}\text{Bi}_x\text{O}_3$  (BPBO) [31]. The maximum  $T_c$  of  $\sim 13$  K was obtained near  $x = 0.25$ . A metal-semiconductor transition was observed near  $x = 0.35$ .

Electronic-structure calculations [32] explain the semiconducting behavior of  $\text{BaBiO}_3$  and how Pb doping increases conductivity. Further calculations [33] indicated that this semiconductor-like gap could be suppressed as well by doping substitutionally on the Ba rather than Bi sites. Studies were done with a combination of K and Pb doping [34] but only resulted in  $T_c$ 's of  $\sim 12$  K. Some very important observations were made as a result of these experiments, however. The authors pointed out the following, for example, for BPBO and other superconductors with alkaline or alkaline earth constituents:

- (1) superconductivity occurs only over a limited range of  $x$  (as in  $\text{BaPb}_{1-x}\text{Bi}_x\text{O}_3$ ),  
between a conducting and semiconducting phase
- (2)  $T_c$  increases rapidly as  $x$  approaches the semiconducting phase boundary and  
disappears abruptly beyond the phase boundary
- (3) all of the compounds have atoms occupying octahedral sites with six oxygen  
nearest neighbors.

These observations established principles which were considered in further exploration of possible superconducting compounds and indeed were found to be true for BKBO as well.

Emphasis was then placed on substituting alkali metals for Ba. Superconductivity was subsequently observed with transitions of  $\sim 15$  K for  $\text{Ba}_{0.9}\text{Rb}_{0.2}\text{BiO}_3$  and  $\sim 20$  K for  $\text{Ba}_{0.9}\text{K}_{0.2}\text{BiO}_3$  [35]. Yet higher  $T_c$ 's in these compounds were predicted [36] and observed ( $T_c$  onset  $\sim 30$  K) in the latter (BKBO) [37].

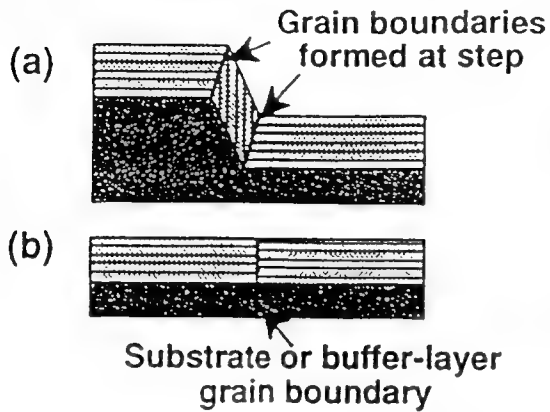
## B. Historical background of Josephson Junction development

Tunneling in junctions was first observed by Ivar Giaever in 1960 [38]. He received the Nobel Prize in Physics in 1973 for his efforts. The first tunnel junction with Al and Pb electrodes was fabricated in 1960 [39], and SIS tunneling with tin and lead electrodes was demonstrated in 1963 [40]. These low-temperature superconducting materials were used to fabricate early SIS edge junctions. This geometry was chosen to address the need to decrease junction area and hence lower capacitance. A small capacitance is necessary to increase switching speed and to eliminate hysteresis from the I-V curve for fast, nonlatching logic and magnetometry applications. Several combinations of materials were studied in the edge configuration. An Sn/Ge/Pb system resulted in junctions with a critical current density of  $10^5$  A/cm<sup>2</sup> [41]. A silicon substrate/SiO<sub>2</sub>/Nb/ Nb<sub>2</sub>O<sub>5</sub>/Pb junction yielded  $2 \times 10^4$  A/cm<sup>2</sup> [42], and the In/InO<sub>x</sub>/Pb system,  $10^3$  A/cm<sup>2</sup> [43]. Nb/Al<sub>2</sub>O<sub>3</sub>/Pb-Bi junctions resulted in  $10^6$  A/cm<sup>2</sup> [44], and Nb/Nb oxide/PbIn [45] junctions,  $3 \times 10^4$  A/cm<sup>2</sup>.

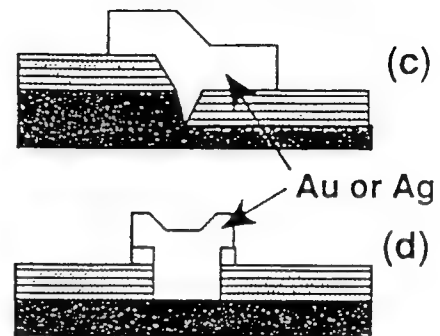
The later discovery of oxide superconductors such as YBCO afforded the opportunity to use higher-temperature superconductors as the electrodes of the junction. The use of normal-conducting materials as the barrier allows the use of a thicker barrier and is possible with the advent of nonhysteretic logic, such as single-flux quantum logic, which has a rapid response time. The edge configuration in this case is not only desirable for lowering capacitance but also for taking advantage of the longer coherence lengths in the *a* and *b* directions of *c*-axis-oriented YBCO (or other high-T<sub>c</sub> oxide) films. This configuration is shown in Figure 19.

YBCO is presently believed by the superconductivity community to be the most desirable material for edge junctions. YBCO edge junctions with the following barriers have been studied: plasma-treated YBCO [46], plasma-damaged, normal

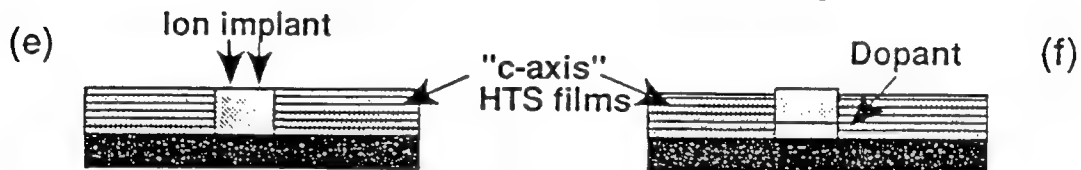
### GRAIN BOUNDARY WEAK LINKS



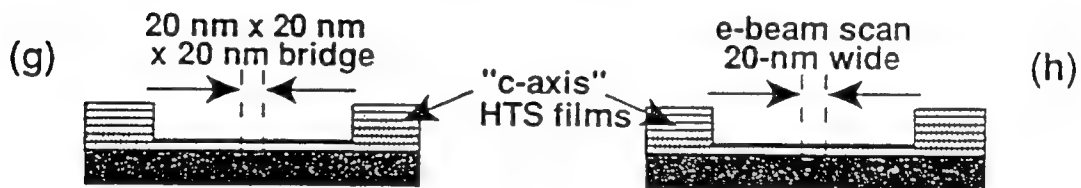
### PLANAR S-N-S



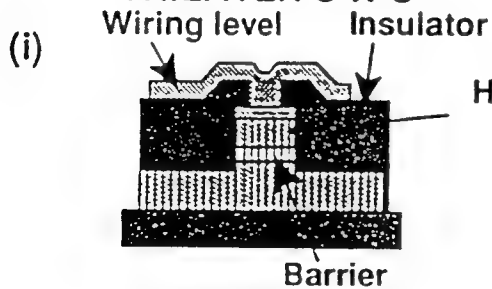
### "POISON STRIPE" WEAK LINKS



### S-S'-S NANOBRIDGES



### TRILAYER S-N-S



### EDGE S-N-S

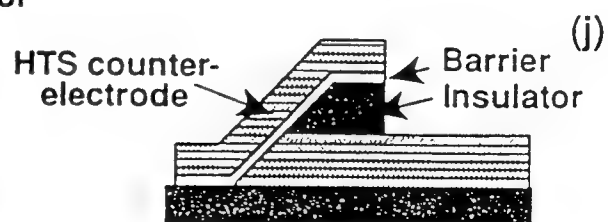


Figure 19. Schematic of various types of SNS and SS'S Josephson junctions.

YBCO [47], MgO [48],  $\text{PrBa}_2\text{Cu}_3\text{O}_{7-\delta}$  (PBCO) [49],  $\text{CaRuO}_3$  [50],  $\text{Y}_2\text{O}_3$  [51],  $\text{SrRuO}_3$  [52], and  $\text{La}_{0.5}\text{Sr}_{0.5}\text{CoO}_3$ ,  $\text{La}_{1.4}\text{Sr}_{0.6}\text{CuO}_4$ ,  $\text{Y}_{0.7}\text{Ca}_{0.3}\text{Ba}_2\text{Cu}_3\text{O}_{7-x}$  (Ca/YBCO), and  $\text{YBa}_2\text{Cu}_{2.79}\text{Co}_{0.21}\text{O}_{7-x}$  (Co/YBCO) [53].

Other junction configurations which exist are grain-boundary junctions, in which a grain boundary is formed at a step or discontinuity in a substrate, planar SNS, in which the barrier is deposited in a break in the superconducting film, or "poison stripe" weak links, in which the barrier region is a doped or ion-implanted one, and trilayer junctions.

BKBO junctions have been fabricated with YBCO base electrodes and a natural [54] or artificial [55] insulating barrier. BKBO SIS trilayer junctions have been produced using  $\text{BaBi}_2\text{O}_y$  [56],  $\text{KNbO}_3$  [57],  $\text{SrTiO}_3$  [58], and MgO [59] barriers. Bicrystal junctions which introduce a grain boundary between the electrodes have been studied [60], and an Au/BKBO/ $\text{SrTiO}_3(\text{Nb})$  superconducting-base transistor has been fabricated [61]. Most of these junctions, however, are highly resistive and exhibit leakage. The challenge with all of these materials is to fabricate junctions reproducibly.

### C. Introduction to BKBO properties

#### 1. Structure

As an oxide possessing a perovskite structure, BKBO is similar to other high- $T_c$  superconductors. Common among BKBO and the other high-temperature superconductors is an extreme sensitivity of the materials to oxygen stoichiometry [62][63]. The superconducting phase, however, is cubic, thus making BKBO similar to the isotropic lower- $T_c$  superconductors such as the Nb compounds. Its parent structure is  $\text{BaBiO}_3$ , and the superconductor contains potassium which occupies the barium sites in the structure shown in Figure 20. Superconductivity occurs only in

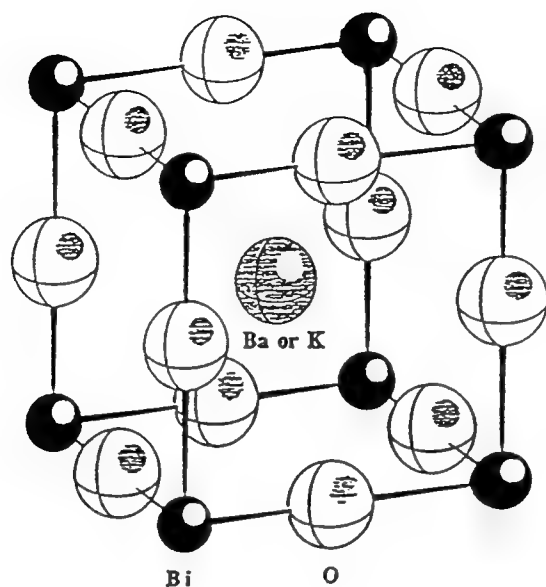


Figure 20. The structure of BKBO [64].

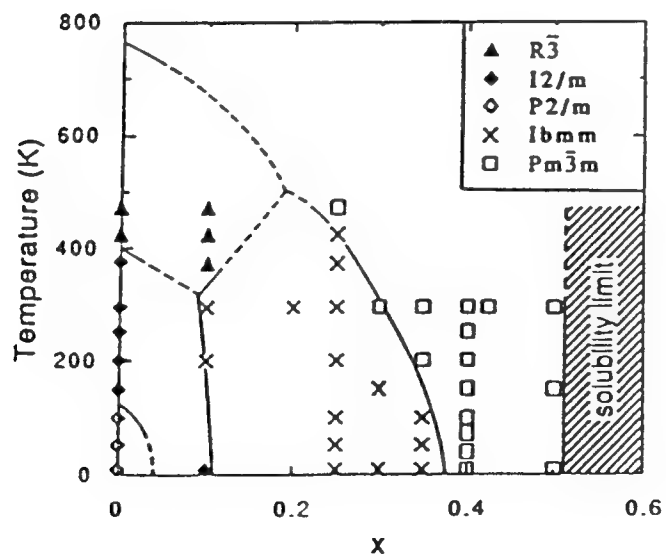


Figure 21. "Phase" diagram for  $\text{Ba}_{1-x}\text{K}_x\text{BiO}_3$  as a function of potassium content,  $x$  [65].

the cubic perovskite phase (with a space group of  $\text{Pm}\overline{3}\text{m}$ ) which exists for  $0.37 < x < 0.5$  in  $\text{Ba}_{1-x}\text{K}_x\text{BiO}_3$  [65]. A structural "phase" diagram of crystal structures present as a function of temperature and K content is shown in Figure 21. Each phase is a derivative structure, so the transitions represent higher-order ones. The diagram shows that too little potassium results in an orthorhombic  $\text{Ibmm}$  phase, whereas too much causes a second phase,  $\text{KBiO}_2$ , to precipitate [66][67]. Figure 22 shows how the monoclinic  $\text{BaBiO}_3$  with tilted  $\text{BiO}_6$  octahedra becomes cubic for  $\text{Ba}_{0.6}\text{K}_{0.4}\text{BiO}_3$ .

The x-ray diffraction pattern of polycrystalline BKBO is shown in Figure 23. This compound has not been widely studied and there is little information available on its basic properties. There was no JCPDS card and it was therefore necessary to generate the structure factor calculations as detailed in Appendix I.

It has been found that the lattice parameter of  $\text{Ba}_{0.6}\text{K}_{0.4}\text{BiO}_3$  at 295 K is 4.283 Å [65]. The same authors have determined that the lattice parameter scales linearly with potassium content, as shown in Figure 24. From this diagram, one can see that in the range of  $x=0.37$  to  $x=0.5$  the lattice parameter varies from 4.289 Å to 4.270 Å, respectively. It is helpful to use the lattice parameter determined from x-ray diffraction data to predict the potassium content as an indication of whether the film may be superconducting. This prediction is not necessarily straightforward, however, because lattice parameter changes with oxygen content as well [70][71]. If one considers the stoichiometry  $\text{Ba}_{1-x}\text{K}_x\text{BiO}_{3-\delta}$ , it has been found [70] that the lattice parameter of  $\text{Ba}_{0.6}\text{K}_{0.4}\text{BiO}_{3-\delta}$  changed by 0.0276 Å, a 0.64 % expansion, upon changing  $\delta$  from 0.121 to 0.464, which is an 11.9 % reduction in oxygen content. The change in lattice parameter may not seem significant, but the difference between the lattice parameters at limiting stoichiometries of the  $\text{Pm}\overline{3}\text{m}$  phase, which are 4.270 Å and 4.289 Å, is only 0.44 %. This means that a slight deficiency in



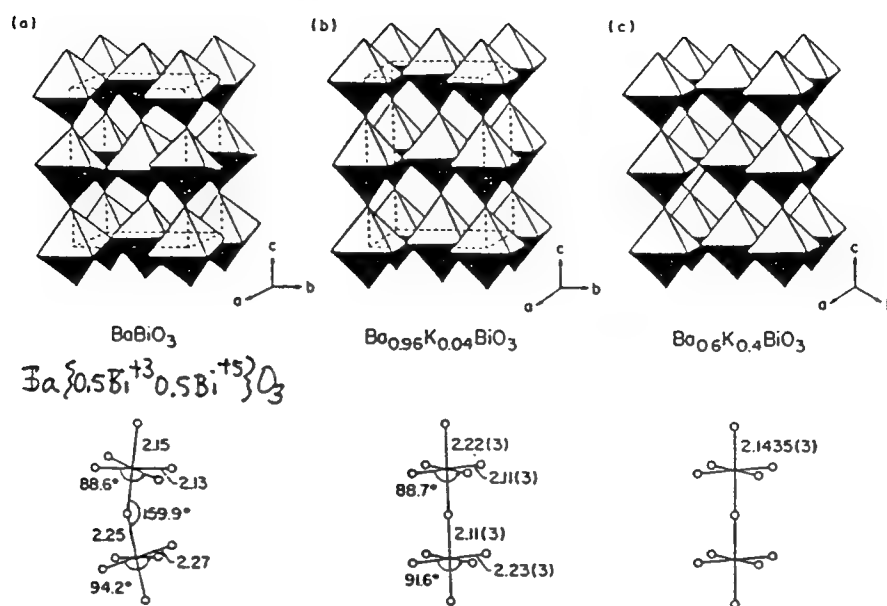


Figure 22. Crystal structures of several compounds in the BKBO series. The figures below them show the tilting of the  $\text{BiO}_6$  octahedra [68].

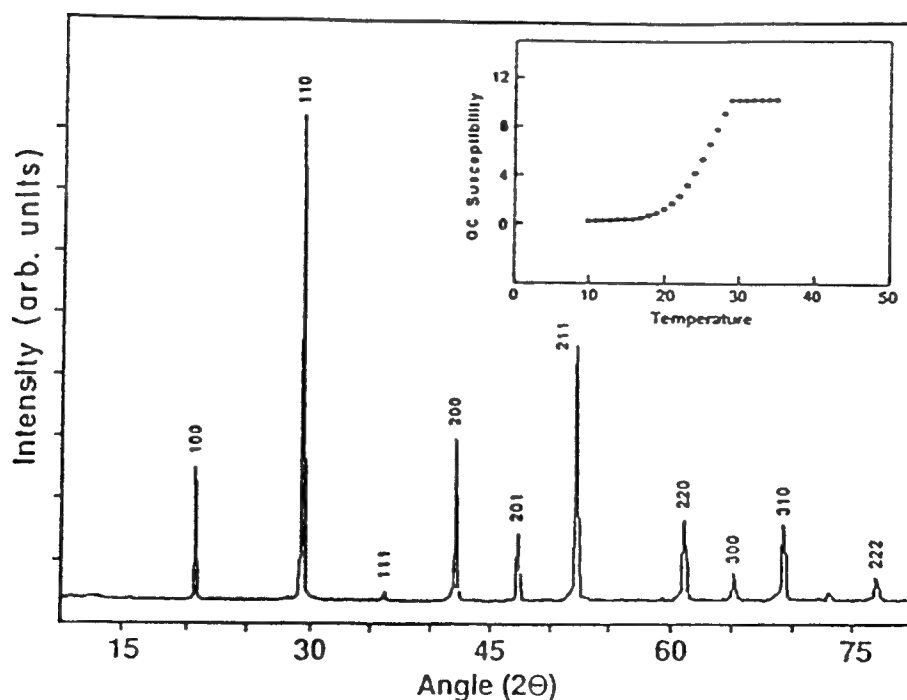


Figure 23. X-ray diffraction powder pattern of BKBO. Inset shows ac susceptibility of the sample [69].

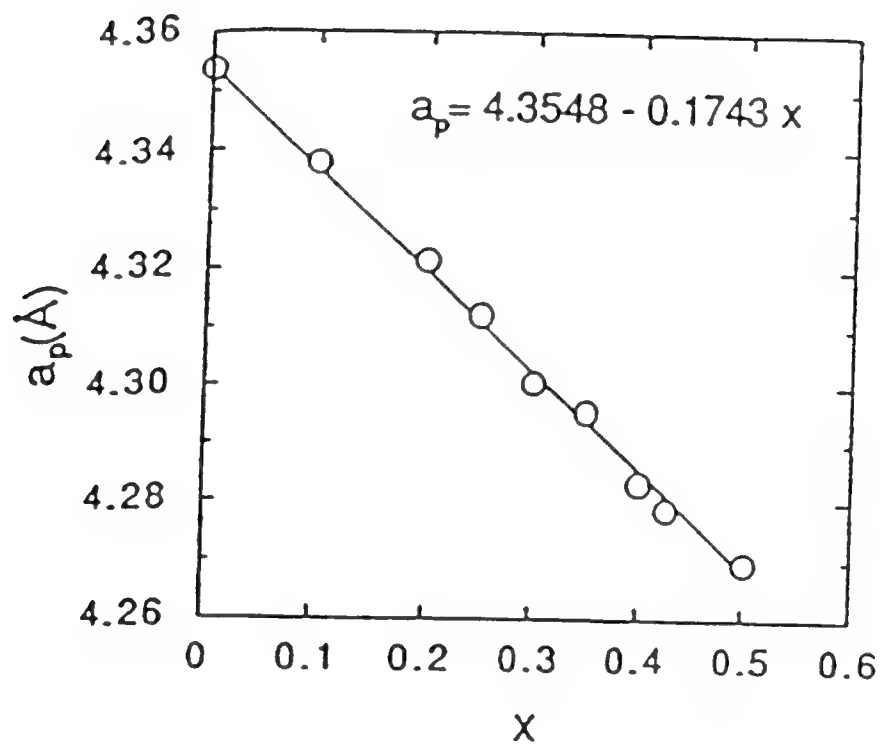


Figure 24. Pseudocubic lattice parameter change as a function of potassium content,  $x$  [65].

oxygen content could cause the films to be non-superconducting. This stresses the importance of a post-anneal in O<sub>2</sub>. It is felt that it is better to add the excess oxygen later rather than during deposition, so that enough potassium is incorporated. This is in order to maintain charge balance; if the average Bi charge is not to exceed +4, the K can only enter the compound if there are oxygen vacancies present [72].

## 2. Pairing mechanism

Tunneling measurements by tunneling spectroscopy [73], in SIN junctions [74][75][76][77], and SIS point-contact junctions [78][79] have demonstrated a superconducting energy gap with a low density of electronic states below the gap energy. The observation of the gap has led to the calculation of  $2\Delta/kT_C$ , which has yielded values of 3.7-4.0 [73][74][76][80][81][82]. These values are indicative of moderate-to-strong coupling. It is believed by many that the pairing reflects electron-phonon coupling, which has been substantiated by the results of a number of different measurements. Electron - phonon coupling is indicated by the relatively high values of the exponent  $\alpha$  obtained in measurements of the oxygen isotope effect [83][84][85][86]. Tunneling spectroscopy results [80] link optical phonons to superconducting electrons, as does Raman spectroscopy [87], and the softening of oxygen phonon modes associated with the doping of BaBiO<sub>3</sub> by potassium (and the consequent change in charge) [88] also points to this conclusion. Similarly, the gap measured by infrared reflectivity [89] is consistent with moderate coupling in BCS theory, and the oxygen atom vibrations observed by x-ray diffraction techniques indicate strong electron-phonon coupling [68][90]. The change seen in the isotropic thermal parameter at the superconducting transition [91] as well as specific heat measurements [92][93][94] show this, as does the observation of a structural transformation at the same composition as an electronic one to a superconducting

phase [65]. Calculated electron-phonon coupling strengths are in agreement with experimental observations [95][96][97][98][99].

### 3. Electronic structure

It is surprising that BKBO has such a high  $T_c$  compared to other BCS-like superconductors because of its low density of states at the Fermi energy [100]. According to BCS theory, the transition temperature is exponentially proportional to the number of states at the Fermi level. The band structure of BKBO is shown in Figure 25. It can be seen from this band diagram that the Fermi level cuts through the uppermost band of a ten-band Bi(6s)-O(2p) complex. The uppermost band is parabolic and therefore free-electron-like; such symmetry around the  $\Gamma$ , or center, point of the Brillouin zone indicates an s-like character. The flat, low-lying bands correspond to Ba 5p states, while the unoccupied bands at the top are those of Ba 5d and Bi 6p states [36].

A more simplified version of the diagram for  $\text{Bi}_2\text{O}_3$  is shown in Figure 26. In this diagram, it can be seen that the O 2p band can be considered the valence band and the Bi 6p band, the conduction band, although it should be noted that these bands all contain hybrid orbitals. The positions in energy of these bands with respect to each other is dependent on the Bi-O distance. As this distance decreases, the metal levels increase in energy relative to the oxygen levels. Thus when electrons are removed, as in  $\text{KBiO}_3$ , the Bi-O distance decreases and the Bi 6s band lies just above the O 2p band and the Fermi level. In  $\text{BaBiO}_3$ , however, only half of the Bi 6s band is above the Fermi level [101]. This is due to the disproportionation in  $\text{BaBiO}_3$ . A simple charge balance will show that the effective charge of Bi must be +4. The electronic configuration of this element, however, is  $\text{Xe}4f^{14}5d^{10}6s^26p^3$ . A valence

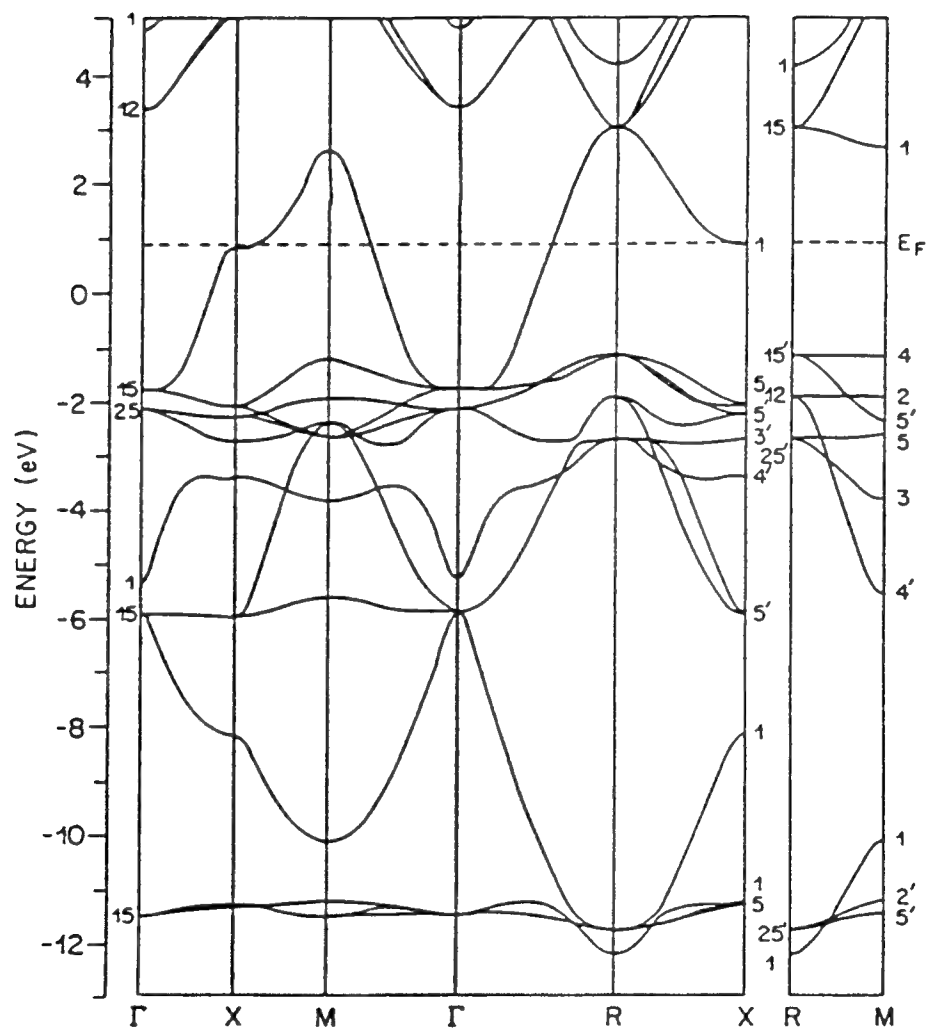


Figure 25. Energy band diagram for BKBO as a function of crystallographic direction in the Brillouin zone [36].

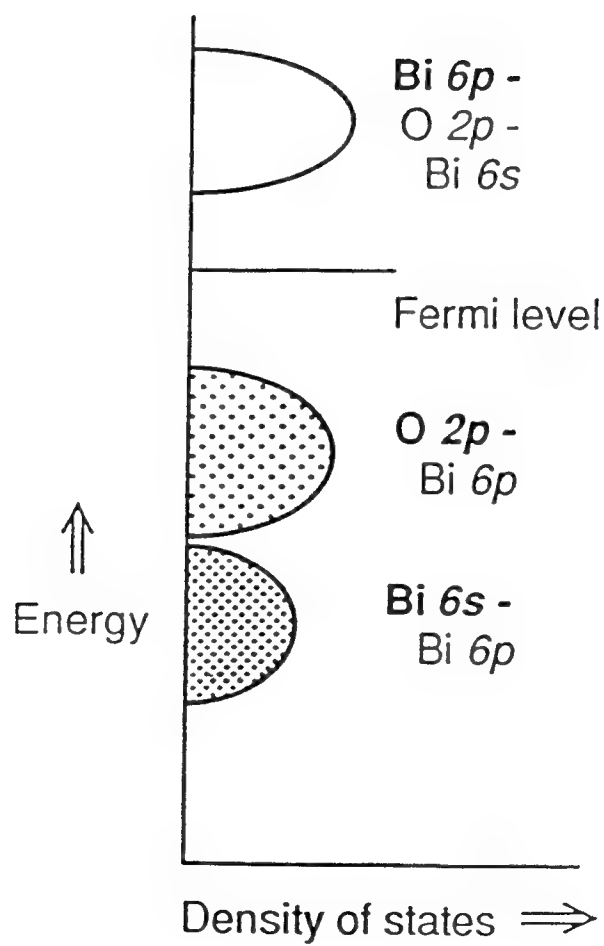


Figure 26. Schematic of density of states for  $\text{Bi}_2\text{O}_3$  [101].

of +4 for Bi would lead to a very undesirable  $6s^1$  state. It is therefore energetically favorable for charge neutrality to be maintained by Bi assuming the charges of +3 and +5, so this compound can actually be written  $\text{Ba}\{0.5\text{Bi}^{+3}0.5\text{Bi}^{+5}\}\text{O}_3$ . The band structure for this compound has the Bi 6s band at the Fermi level, and this band has split due to the two different Bi-O distances. The  $\text{Bi}^{+3}$ -O distance in  $\text{BaBiO}_3$  is 2.31 Å, while the  $\text{Bi}^{+5}$ -O distance is 2.12 Å [102]. The  $\text{Bi}^{+3}$  half of the Bi 6s band is below the Fermi level, whereas the  $\text{Bi}^{+5}$  half is above.  $\text{BaBiO}_3$  therefore exhibits a gap; conduction will occur if the reaction  $\text{Bi}^{+3} + \text{Bi}^{+5} \rightarrow \text{Bi}^{+4}$  takes place [101]. Doping is necessary for the effective charge to change. When potassium is added, the compound is depleted of electrons because  $\text{K}^{+1}$  ions occupy  $\text{Ba}^{+2}$  sites. At the composition  $\text{Ba}_{0.6}\text{K}_{0.4}\text{BiO}_3$ , for example, the effective charge on Bi is 4.4, so with increasing K concentration, the Bi valence approaches +5. This closes the energy band gap and increases conduction.

The oxidation of  $\text{Bi}^{+3}$  to  $\text{Bi}^{+5}$  upon addition of K has been demonstrated experimentally [103]. This result would lead one to believe that the electrons freed as a result of this oxidation would then be available for conduction. Hall Effect measurements have determined BKBO to indeed be n-type [85][104][105][106][107], which indicates that electrons rather than holes are responsible for conduction.

#### 4. Transition temperature

The highest onset transition temperature obtained for bulk BKBO is 34 K [108]. This allows devices made with BKBO, which would be operated at ~15 K, to be cooled by convenient closed-cycle helium refrigeration, in which He gas is recondensed rather than requiring an endless supply of expensive liquid helium.

It has been found [107][109][110] that  $T_C$  increases with increasing pressure up to 15 kbar, but this trend only occurs up to a point, and then there is a downward slope as the  $T_C$  of the material at zero pressure increases [111].

The highest- $T_C$  thin films thus far have been deposited by off-axis rf magnetron sputtering with zero-resistance transition temperatures of 29.2 K [112]. Laser ablation has been used in growing 28 K -  $T_C$  films [76] and 27.5 K -  $T_C$  films [113]. The maximum  $T_C$  will be obtained at a potassium composition of  $x=0.37$  and  $T_C$  then decreases with increasing  $x$  as shown in Figure 27.

## 5. Resistivity

The resistivity of a polycrystalline BKBO sample fabricated by the powder-in-a-tube method with an onset  $T_C$  of 32 K was  $\sim 16,000 \mu\Omega\cdot\text{cm}$  just above the transition [114]. This sample had a very broad (10 K) transition, however, and may therefore have been rather inhomogeneous. Another melt-processed, highly-dense sample had a normal-state resistivity of  $12,000 \mu\Omega\cdot\text{cm}$  [115]. Yet another sample was estimated, from thermal-conductivity data and the application of the Wiedemann-Franz law, to be  $120 \mu\Omega\cdot\text{cm}$  [93]. The Wiedemann-Franz law states that for metals, the ratio of the thermal conductivity to electrical conductivity is directly proportional to the temperature [116], i.e.,  $K/\sigma = \pi^2/3(k/e)^2 T$ .

Metallic behavior is not always observed in BKBO superconducting thin films. There is often a rise in resistivity with decreasing temperature in the normal state, indicating semiconductor-like behavior. It is felt by some [93][104] that each BKBO sample is a mixture of both of these, which is modelled by a metal and semiconductor in series. The rise in resistivity with lowering of temperature seen in BKBO films is indicative of variable-range hopping conduction and follows a  $T^{-1/4}$  dependence [8][93][117][118][119].



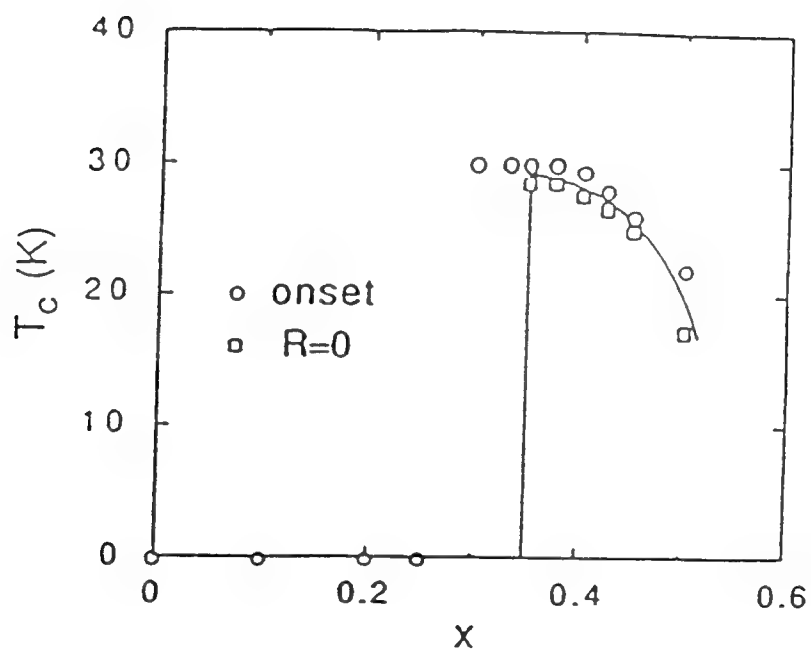


Figure 27. Variation of transition temperature of BKBO with potassium content,  $x$  [65].

It has been demonstrated [120] that in the  $\text{La}_{2-x}\text{Sr}_x\text{CuO}_2$  system, conductivity increases with increasing Sr doping up to  $x=0.34$ . The transition temperature, however, initially rises but then from Sr concentrations of  $x=0.15$  to  $0.25$ ,  $T_c$  decreases until superconductivity disappears. An analogous situation would be expected in BKBO. Conductivity increases with increasing K concentration [35], but  $T_c$  decreases as well [65], implying that a film with a higher  $T_c$  would have a higher resistivity. There have been no reports of a systematic study of this.

## 6. Magnetic properties

BKBO is obviously unlike the cuprates because it does not have two-dimensional Cu-O planes (or chains) which are believed to play a significant role in superconductivity of higher- $T_c$  compounds. In addition, there are no local moments on any of the ions involved (BKBO is diamagnetic in the normal state as well as in the superconducting state) [121].

The dependence of lower critical field,  $H_{c1}$ , on temperature is shown in Figure 28. The dependence of upper critical field,  $H_{c2}$ , on temperature has been measured by a number of groups; a summary is shown in Figure 29, and the lowest and highest slopes obtained are shown in Figures 30 and 31, respectively.

BKBO has a hexagonal flux lattice symmetry [125] and a penetration depth,  $\lambda_0$ , of 3300-3400 Å [81][126]. The value of the penetration depth will increase with increasing temperature dependence for  $T < T_c/2$  [82] according to the following relation:

$$\frac{\lambda(T)}{\lambda(0)} = 1 + \sqrt{\frac{\pi\Delta(0)}{2kT}} \exp\left(\frac{-\Delta(0)}{kT}\right) \quad (23)$$

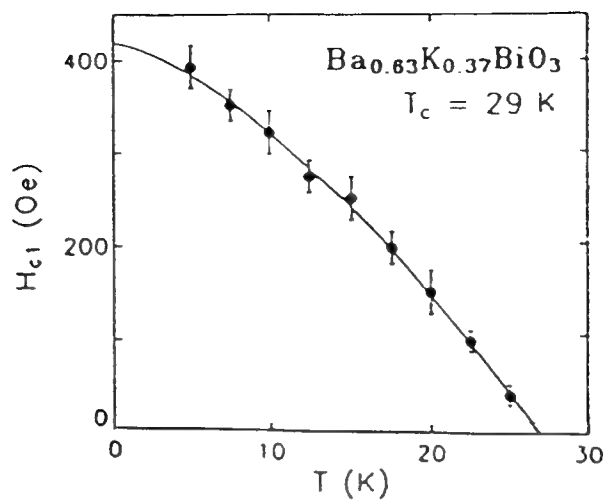


Figure 28. Lower critical field of BKBO as a function of temperature, giving  $H_{c1} = 419 \pm 24 \text{ Oe}$  and  $\lambda = 0.12 \pm 0.02 \mu\text{m}$  [122].

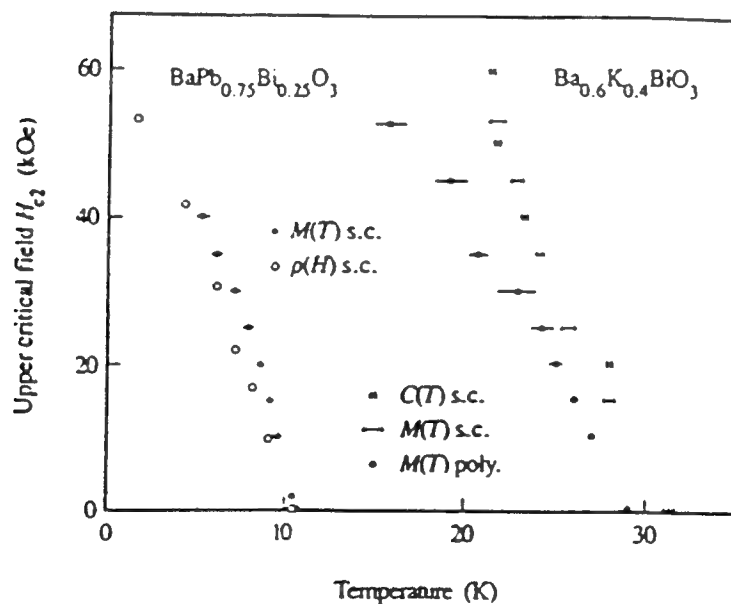


Figure 29. A summary of upper critical field values measured for BPBO and BKBO using various techniques, including magnetization, resistance, and specific heat [123].

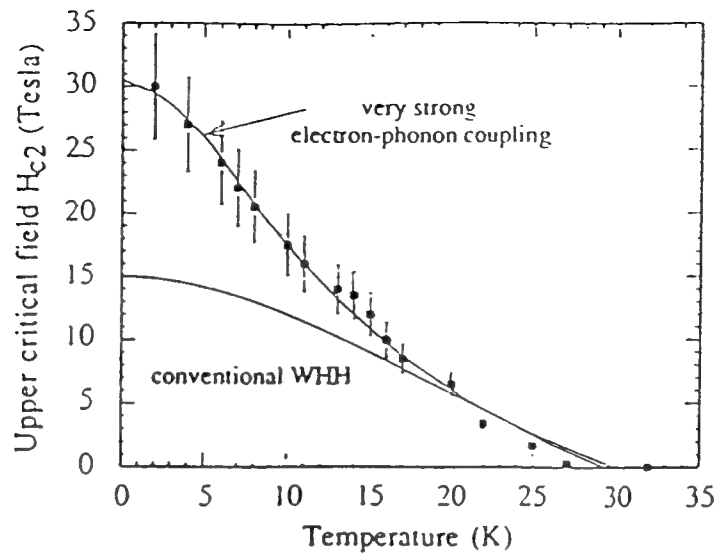


Figure 30. Upper critical field as a function of temperature measured on a BKBO single crystal in a pulsed magnetic field. The solid line is based on modelling [124].

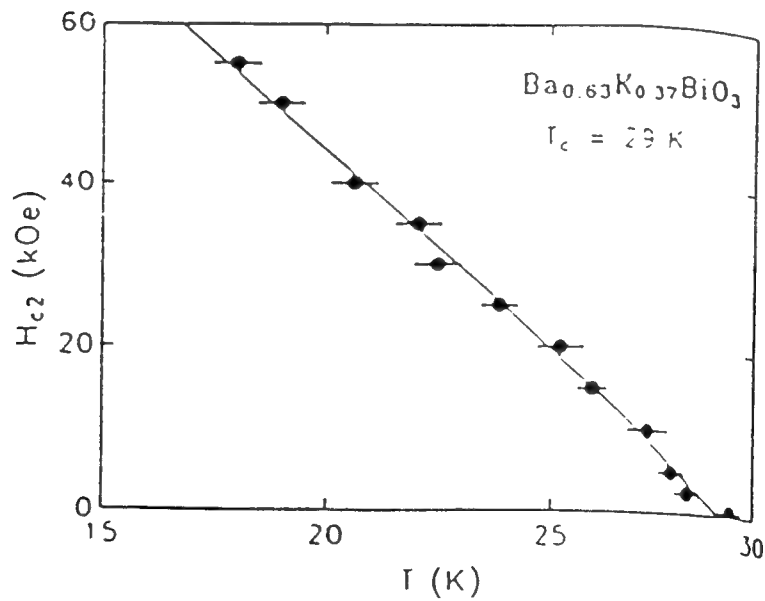


Figure 31. Upper critical field as a function of temperature for a BKBO single crystal. These results yield the values  $dH_{c2}/dT = -4.8 \pm 0.1 \text{ kOe/K}$ ,  $\xi(0) = 58 \pm 1 \text{ \AA}$ , and  $H_{c2}(0) = 96 \pm 2 \text{ kOe}$  [122].

where  $\lambda$  = penetration depth, and  $\Delta$  = gap size. At higher temperatures, the relation will be of the form [127]:

$$\lambda(T) = \frac{\lambda_0}{\sqrt{1 - \left(\frac{T}{T_c}\right)^4}} \quad (24)$$

The advantage of cubic superconductors is that they conduct electricity similarly along the three major axes. The coherence length is therefore isotropic and tends to be longer than those of the higher- $T_c$  superconductors. BKBO has a coherence length of 30-60 Å [94][122][123][124][128][129][130][131][132][133]. This value needs to be carefully considered when fabricating tunnel junctions. High-quality superconductor/ insulator interfaces are necessary so that the superconductor coherence length is not exceeded by the defect region length and so that the superconducting electron pair wavefunction does not decay before the barrier is reached, or the probability of pair tunneling will be too small and the critical current will be diminished.

#### D. YBCO properties

##### 1. Structure

The structure of YBCO is shown in Figure 32. It is based on the basic perovskite cell (the BKBO structure), with the rare-earth Y atom in the body-centered position. When fully oxygenated, the structure is tetragonal (space group P4/mmm) [134]. An orthorhombic structure (space group Pnmm) with oxygen vacancies is necessary for superconductivity, however. If oxygen is further removed so that there is a tetragonal arrangement of vacancies, the sample will no longer be

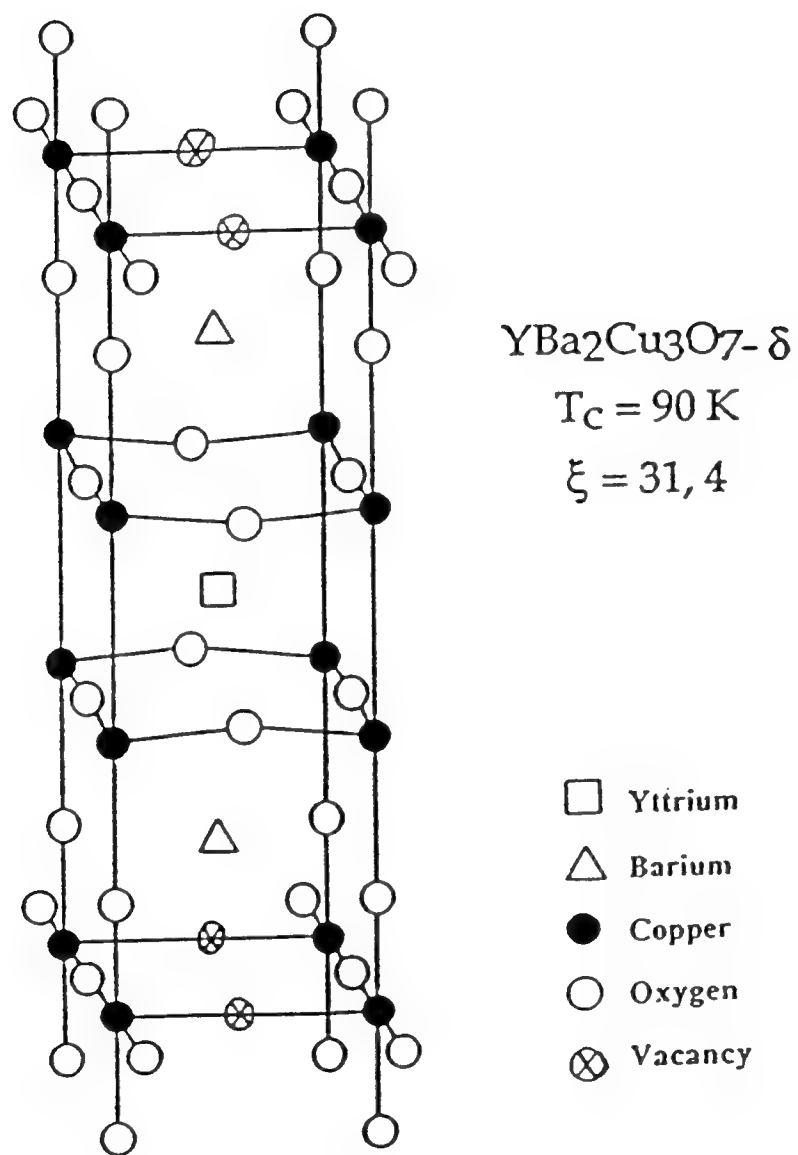


Figure 32. Structure of superconducting YBCO

Table II. Lattice parameters of superconducting YBCO

a, Å	b, Å	c, Å	reference
3.859	3.9195	11.843	Jorgensen, 134
3.822	3.891	11.677	Cava, 136
3.824	3.891	11.685	Steinfink, 137
3.820	3.885	11.683	Williams, 138
3.856	3.868	11.784	Zeng, 139

superconducting. The region over which an orthorhombic phase exists is shown in Figure 33. The lattice parameters of superconducting YBCO are given in Table II. It can be seen from Table II that there is anisotropy within the  $\text{CuO}_2$  planes in superconducting YBCO. The variation in thermal expansion coefficients is shown in Figure 34. Such a difference can lead to microcracking in films.

Synthesizing this compound in the correct stoichiometry is no simple task, because the desired phase is a line compound. The phase diagram for the YBCO system is shown in Figure 35.

## 2. Electronic structure

YBCO has a low density of states at the Fermi energy. The parent compound of YBCO, which is  $\text{YBa}_2\text{Cu}_3\text{O}_6$ , is a charge-transfer insulator. Superconductivity in this compound occurs upon introduction of charge carriers, namely oxygen [141].

The electronic structure of  $\text{YBa}_2\text{Cu}_3\text{O}_7$  has occupied O 2s bands at -16 eV below the Fermi energy, occupied Ba 5p bands at -10 eV, a nearly-full set of 36 Cu 3d- O 2p bands from -5.8 to +1.7 eV, and empty Ba 5d and Y 4d bands above

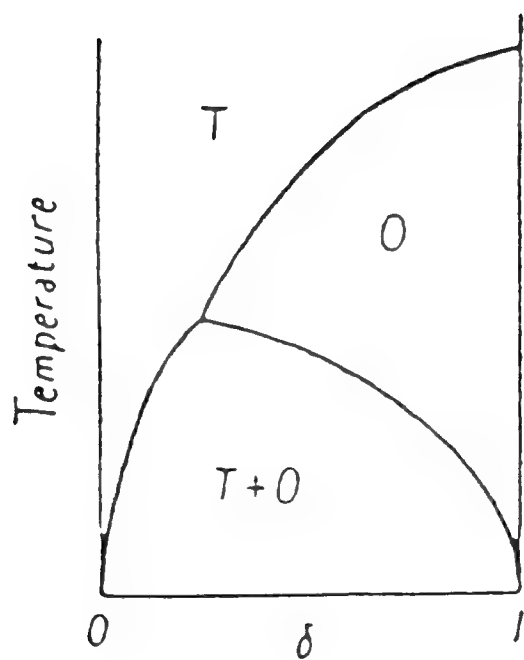


Figure 33. Possible phase diagram of  $\text{YBa}_2\text{Cu}_3\text{O}_{6+\delta}$  assuming only tetragonal and orthorhombic phases are present [135].



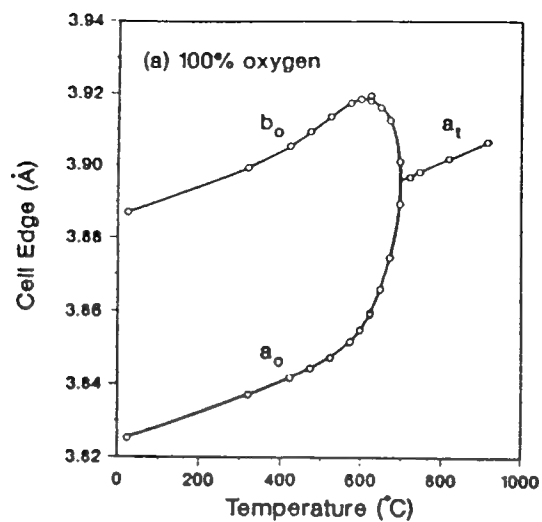


Figure 34. The  $a$ - and  $b$ -axis lattice parameters of YBCO vs. temperature for samples heated in 100% oxygen [134].

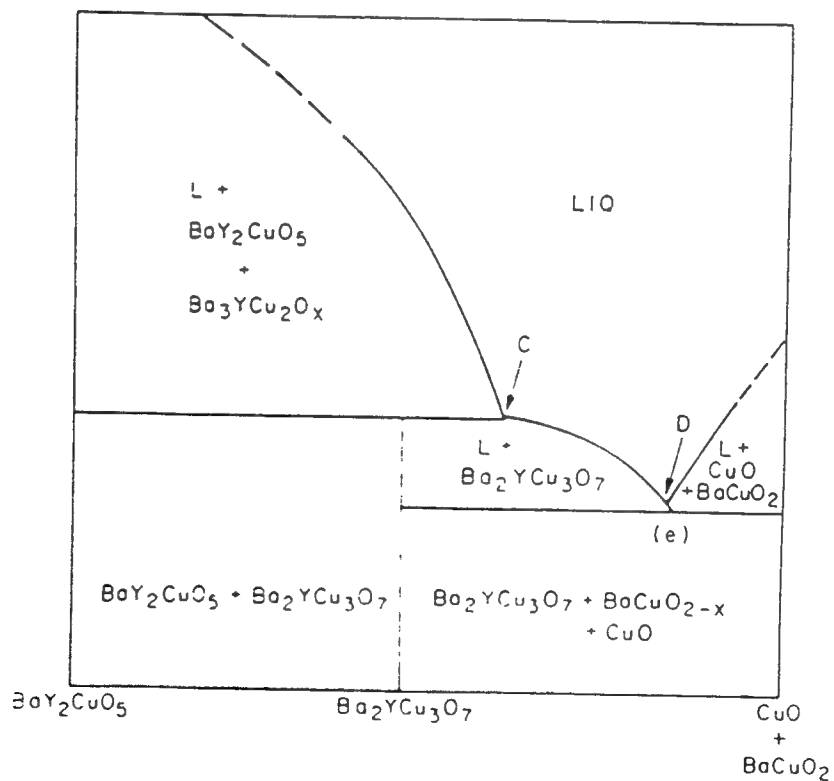


Figure 35. Possible phase diagram for binary cut through the  $\text{CuO}$ - $\text{YO}_{1.5}$ - $\text{BaO}$  phase diagram [140].

3.4 eV. The Cu 3d - O 2p bands are of primary interest and are shown in Figure 36. There are many broad,  $\sigma$  p-d bands in this set crossing many narrow, non-bonding  $\pi$  p-d states. There are no states in the conduction band region from the Y layer, which indicates that it forms an insulating tunneling barrier and that the Cu-O layers are decoupled [142].

### 3. Conduction mechanism

Figure 37 shows the YBCO structure divided into layers. The structure consists of conduction layers (CuO<sub>2</sub> layers) and charge-reservoir layers. The number of carriers is determined by the chemistry of the system and the charge transfer between layers. The amount of charge transferred depends on the structure, the available oxidation states of the atoms, and the competition between charge transfer and oxidation or reduction of metal atoms in the charge reservoir layer. The number of carriers in the conduction layer apparently controls superconductivity; varying the oxygen content can change the YBCO from insulating to superconducting. When the oxygen content is varied, there is a charge transfer between the charge reservoir layer and the conduction layer. Holes are created in the conduction layer when electrons are transferred to the charge reservoir layer. An effective change in the oxidation state of the copper atoms in the conduction planes occurs as a consequence. The change in Cu-O bond lengths can be observed from structural data [143].

The CuO<sub>2</sub> conduction planes control the unit cell dimensions while the intercalating metal-oxide (charge reservoir) layers are stretched to match them. The excess space can hold interstitial defects such as oxygen atoms or substitutional defects on the metal sites, both of which affect superconductivity [143].

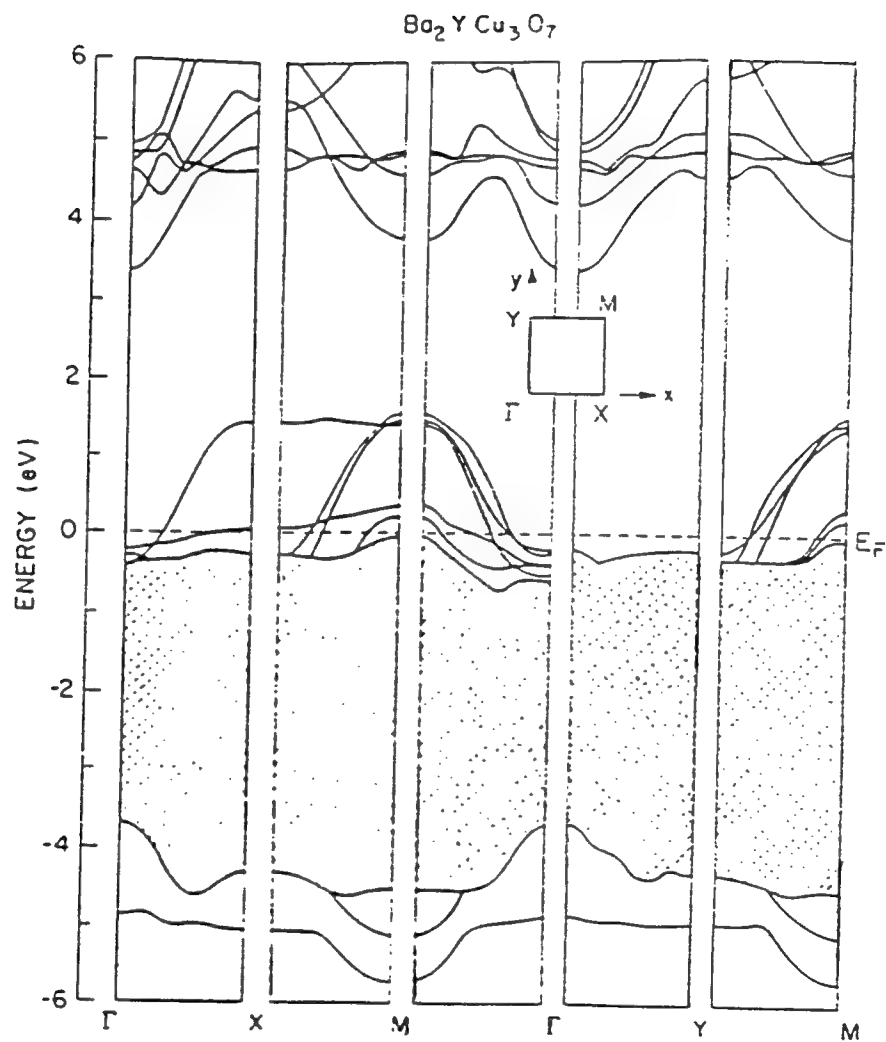


Figure 25. Energy band diagram for YBCO as a function of crystallographic direction in the Brillouin zone. The cross-hatched area denotes a large number of weakly bonded Cu-O bands [142].

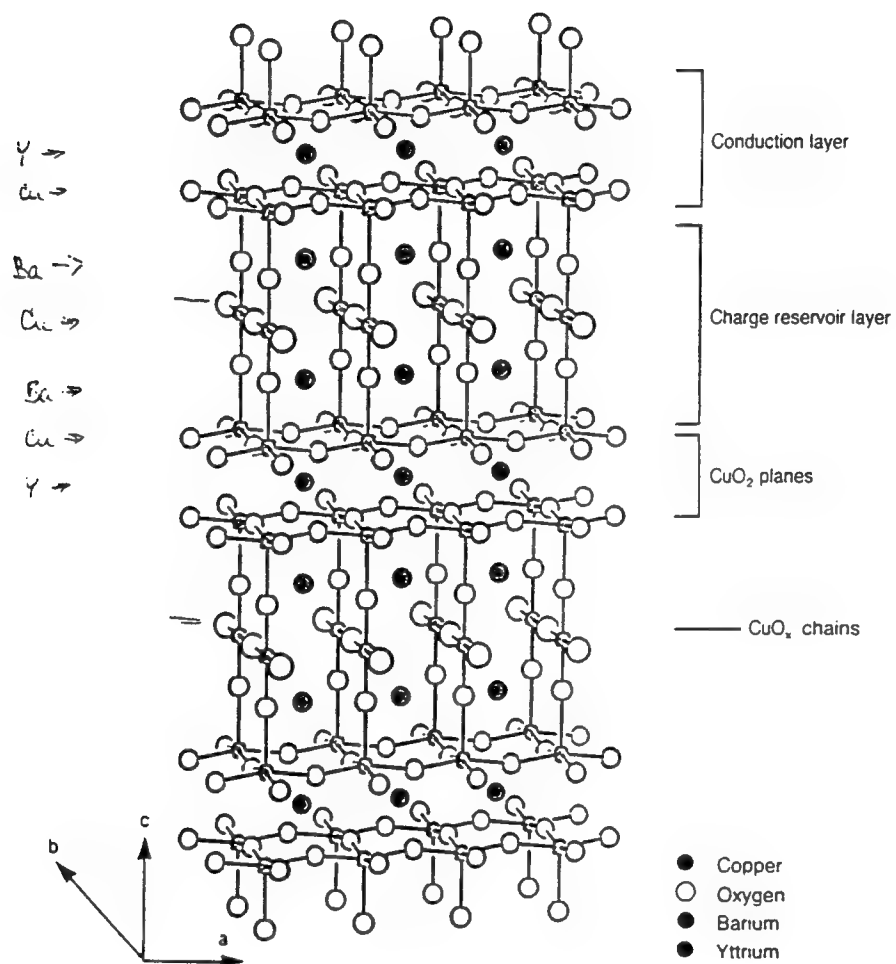


Figure 37. YBCO structure showing alternating conduction layers and charge reservoir layers. The conduction layers consist of two  $\text{CuO}_2$  planes separated by yttrium atoms. The charge reservoir layers consist of  $\text{CuO}_x$  chains along the  $b$  direction and also Ba and O atoms. The oxygen content near the copper chains is variable:  $x$  ranges from 0 to 1 [143].

#### 4. Transition temperature

The variation of transition temperature with oxygen content is shown in Figure 38. This plot demonstrates the importance of oxygen content to superconductivity. It also demonstrates how  $T_c$  can be varied with oxygen content. This can be very useful in junction applications, for example. An oxygen-deficient YBCO film would have a depressed  $T_c$  and could be used as a barrier in an SNS junction.

#### 5. Resistivity

Figure 38 shows the effect of oxygen composition on resistivity in this compound. The anisotropy of resistivity measured on a YBCO single crystal is shown in Figure 39. Resistivity in YBCO has been found to be both metallic and semiconducting.

The Hall coefficient in the cuprates is strongly temperature-dependent, as shown in Figure 40. In addition, the Hall coefficient is very sensitive to oxygen content; there is a rapid increase with increasing oxygen deficiency. The Hall coefficient is positive, indicating that holes are responsible for conduction in this material [144].

#### 6. Magnetic properties

The flux lattice of YBCO has fourfold symmetry for measurements with the magnetic field parallel to the YBCO  $c$  axis. Such symmetry was attributed to pinning by twin planes. When the magnetic field was placed at  $45^\circ$  from the  $c$  axis, a distorted hexagonal pattern was observed [125].

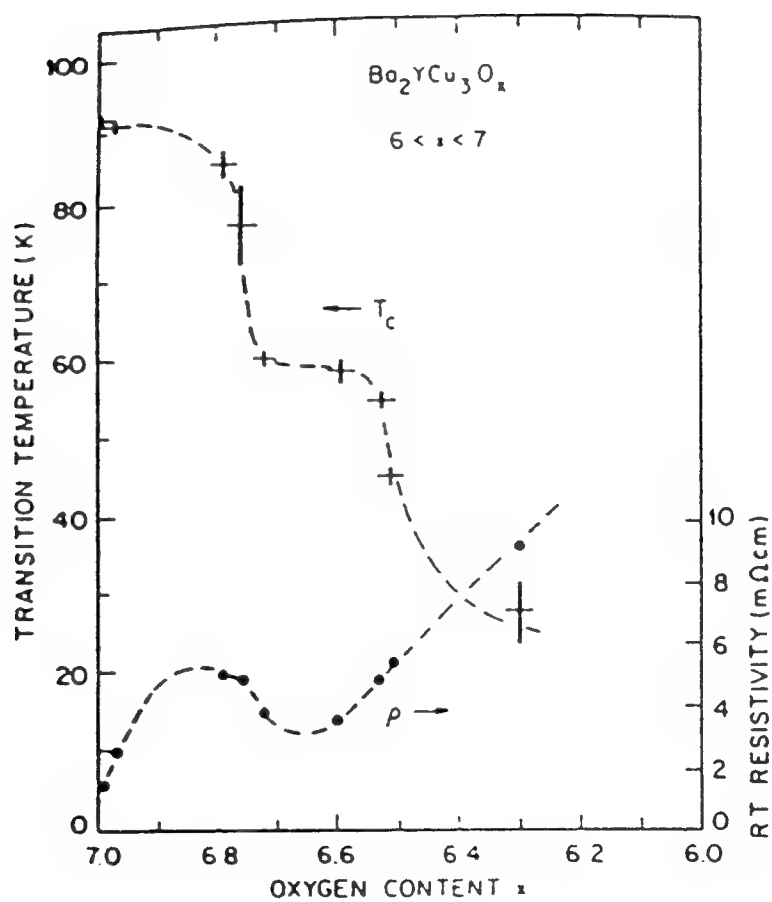


Figure 38. Dependence of  $T_c$  and  $\rho$  on oxygen content of YBCO. The +'s represent the range of the resistive transition [136].

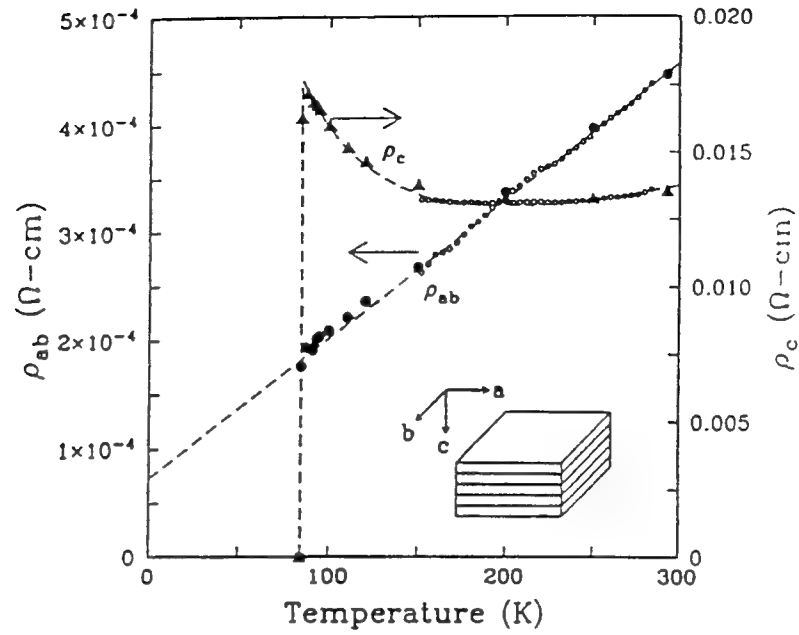


Figure 39. In-plane resistivity  $\rho_{ab}$  and perpendicular resistivity  $\rho_c$  of a YBCO single crystal as functions of temperature. The former shows metallic behavior and the latter, semiconductor-like [144].

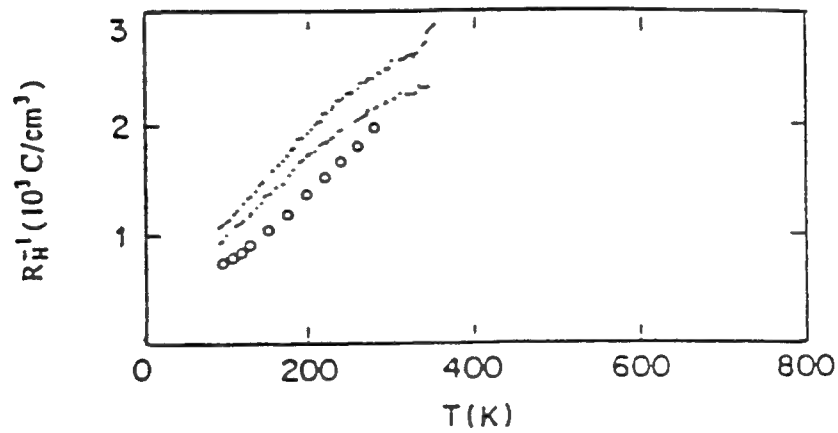


Figure 40. Inverse of the Hall coefficient measured on three YBCO crystals. There is a strong temperature dependence which is most pronounced when  $T_C$  is optimized [141].

The coherence length of YBCO is  $31 \text{ \AA}$  in the  $a$  and  $b$  directions and  $4 \text{ \AA}$  in the  $c$  direction [145]. This difference is significant because there is almost an order of magnitude difference in the conduction capabilities. In addition, in anisotropic superconductors such as YBCO, excitation of "pancake" vortex sections are possible due to extremely short  $c$ -axis coherence lengths. The penetration depth is  $270 \text{ \AA}$  in the  $a$  and  $b$  directions and  $1800 \text{ \AA}$  in the  $c$  direction [145]. A summary of data obtained for the upper and lower critical fields is shown in Tables III and IV.



Table III. A summary of experimental data on the upper  
critical fields of YBCO [144]

Group	Ref.	$-dH_{c1}^{\perp}/dT$ (kOe/K)	$-dH_{c2}^{\perp}/dT$ (kOe/K)	$\xi_{ab}(0)$ (Å)	$\xi_c(0)$ (Å)	Comments
<b>[YBa<sub>2</sub>Cu<sub>3</sub>O<sub>7-δ</sub>]</b>						
ISSP (Tokyo U.)	[25,55,64]	8.8	33	25	6.3	Y, Gd and Ho
ISSP (Tokyo U.)	[65]	11	38	22	6.5	pulse field up to 380 kOe
IBM	[62]	4.6	23	34	7	
	[66]	5.4	38	30	4.3	
NTT	[70]	7	30	27	6	EuBa <sub>2</sub> Cu <sub>3</sub> O <sub>7-δ</sub>
NTT	[67,69]	5.6	33	31	5.1	
NTT/Osaka U.	[71]	4.1	38	35	3.8	pulse field up to 500 kOe
MIT	[68]	11	36	23	6.3	two types of samples
		9.6	40	23	5.6	
Grenoble/Renne	[72]	7.7	32	26	6.3	TmBa <sub>2</sub> Cu <sub>3</sub> O <sub>7-δ</sub>
<b>[(La<sub>1-x</sub>Sr<sub>x</sub>)<sub>2</sub>CuO<sub>4</sub>]</b>						
IMS	[59]	5		40		(mid-point)
		2		80		(La <sub>1-x</sub> Ba <sub>x</sub> ) <sub>2</sub> CuO <sub>4</sub>
NTT	[73]	12	63	47	8.9	(x ~ 0.04)
<b>[Bi<sub>2</sub>Sr<sub>2</sub>CaCu<sub>2</sub>O<sub>8+x</sub>]</b>						
Tokyo U.	[74]	5	45-50	35	3.3	(mid-point)
IMR (Tohoku U.)	[75]	3.9	73	39	2.1	(mid-point)
AT&T	[76]	5.5	45	31	4	(extrapolation to R = 0)

Table IV. A summary of experimental data on the lower  
critical fields of YBCO [144]

Group	Ref.	$H_{c1}^{\perp}$ (Oe)	$H_{c1}^{\parallel}$ (Oe)
<b>[YBa<sub>2</sub>Cu<sub>3</sub>O<sub>7-δ</sub>]</b>			
IBM	[93]	4000	600
	[95]	4000	200
	[96]	950	230
Argonne	[94]	690	120

## Chapter III. Research objectives

### A. Necessary junction properties

This thesis research is concerned with the development of BKBO and YBCO superconductors for microelectronic devices and the understanding of the structural, chemical, and electronic behavior of these devices. In particular, BKBO and YBCO have been targeted for use in Josephson junctions. The following section is a discussion of the properties that junction components need to possess.

#### 1. Tunnel Junctions (SIS)

- (a) *Superconducting films* - The superconducting electrodes need to be of good quality with few defects, particularly at the superconductor-insulator interface. This interface should be atomically smooth in order to ensure a uniform barrier thickness and thus a reproducible critical current density,  $J_c$ . Isotropic superconductors such as BKBO are advantageous because a [100] orientation will give the same electrical response as an [001]. In addition, an isotropic gap is important for tunneling characteristics.

The characteristic distance for decay by  $1/e$  is the superconducting coherence length,  $\xi$ . Materials with longer coherence lengths are preferred for junctions so that the electron pair wavefunction remains coherent over longer distances and even through grain boundaries, which act as weak links to current transport in oxide superconductors, defects such as dislocations, twin boundaries, and insulating barriers.

- (b) *Barrier* - There is an exponential decay of the transmitted supercurrent through the barrier. It must therefore be thin enough to allow tunneling without entirely diminishing the electron wavefunction. Tunneling probability is determined by

both barrier height and thickness, as described in the Simmons Model (see Appendix II). The barrier must be grown uniformly and without pinholes. The latter could cause shorts, which are undesirable conduction paths in parallel with the junction. Barriers should be closely lattice-matched with the superconductor in order to ensure good epitaxy. This will give the electrons a cleaner path at the superconductor/insulator interface rather than introducing obstacles to conduction such as misfit dislocations or high-angle grain boundaries, which will effectively shorten the coherence length or, if long enough, will cause superconducting electron pairs to break apart.

Many oxides have a relative dielectric constant of 10-30. These are acceptable, but it is desirable to have a barrier with a lower dielectric constant in order to lower the capacitance of the junction. The higher the capacitance for a junction of fixed area, the slower the junction switching time will be.

- (c) *Substrate* - For epitaxial films to be grown, the substrate material must be well lattice-matched with the superconductor. It should be chemically compatible with the superconductor, have a similar coefficient of thermal expansion, and be capable of being fabricated in large wafers. Substrates should be uniform (as should be all of the layers deposited on it) so that junctions can be reliably patterned (for example, the twinning that occurs in  $\text{LaAlO}_3$  makes it difficult to pattern films on it). Table V shows some typical substrates with their lattice parameters, thermal expansion coefficients, and dielectric constants compared to those of BKBO. It can be seen that MgO has the closest lattice match to BKBO as well as a low dielectric constant.  $\text{SrTiO}_3$  has the same space group and a close match in thermal expansion but a somewhat larger lattice mismatch and a very high dielectric constant.

Table V. Properties of typical substrate materials compared to those of BKBO

substrate	crystal syst. or space group [146]	pseudocubic lattice [146] param. (Å)	% lattice mismatch to BKBO	coeff. of thermal expansion ( $\times 10^{-6}/K$ )	dielectric constant at RT [151]
LaAlO <sub>3</sub>	R3m→cubic (at 400°C)	$d_{100}(c)=$ $d_{012}(h)=$ 3.792	11.5	31.8 [147]	16-23
MgO	$Fm\bar{3}m$	4.212	1.7	10.5 [148]	8-10
NdGaO <sub>3</sub>	orthorhomb.	$d_{110}(0)=$ $d_{100}(c)=$ 3.855	10	9.96 [149]	24
Al <sub>2</sub> O <sub>3</sub>	hexagonal	$a=b=4.758$ $c=12.991$	11.1	5.4 [148]	8.5-11.5
SrTiO <sub>3</sub>	$Pm\bar{3}m$	3.905	8.8	11 [148]	200-300
BKBO	$Pm\bar{3}m$	4.283 [65]	----	10 [150]	----

## 2. Edge junctions (SNS)

The edge junction configuration is desirable because it takes advantage of the greater conduction in the  $a$  and  $b$  directions of anisotropic superconductors. In addition, the small area of the junction serves to reduce junction capacitance. This is important for increasing junction switching speed as well as in eliminating hysteresis from the I-V characteristic.

- (a) *Base electrode* - As in SIS junctions, the substrate and superconducting film should be well lattice-matched and have similar coefficients of thermal expansion. An anisotropic superconductor such as YBCO has several disadvantages compared to isotropic ones such as BKBO. The coherence length in the  $a$  and  $b$  directions is much longer than that in the  $c$  direction (31 Å as opposed to 4 Å).

The greater conduction in the  $a$  and  $b$  directions make  $c$ -axis-oriented films much better for in-plane conduction and therefore transport across an edge junction or to other devices, whereas  $a$ -axis-oriented films are better for conduction through a trilayer junction. An anisotropic coherence length influences thermal dissipative response. In anisotropic superconductors, excitation of "pancake" vortex sections are possible due to extremely short  $c$ -axis coherence lengths. These can be quite deleterious as a source of noise in superconducting circuits. Physical properties are also of great importance; anisotropic thermal expansion coefficients have been suggested to be responsible for microcracking in polycrystalline YBCO.

The superconducting films must be well-oriented, because the material present in the grain boundaries of YBCO has been found to be non-superconducting [152], and even the cleanest high-angle grain boundaries cause a reduction in critical current by a factor of 50 [18]. The base electrode needs to be several penetration depths thick in order to lessen inductance effects. The frequency in a resistanceless LC circuit equals  $1/(LC)^{1/2}$  [153], so a low inductance is preferable. It is important, however, not to exceed a thickness of 4000 Å [154], or the possibility of nucleating  $a$ -axis grains will arise.

- (b) *Insulator* - The insulator must grow epitaxially and uniformly so that the junction does not short. It must be a material that can be deposited within a reasonable amount of time and should possess a relatively low dielectric constant in order to lessen switching speed. It must be able to withstand ion-milling without degradation.
- (c) *Barrier* - The barrier must be thin enough so that the normal-material coherence length,  $\xi_n$ , is not exceeded. This is the distance over which a weakly superconducting layer is created in the normal metal by the diffusion of superconducting electrons and is inversely proportional to the resistivity of the

normal region. It is therefore desirable to use a highly conductive material for the barrier. This allows the use of a thicker barrier, which alleviates the concern about pinholes. There must, however, be epitaxy between the base electrode and the barrier. The effective coherence length,  $\xi_n$ , will be shortened by any interfacial chemical reaction, strain, or defects present at the interface. A barrier material such as gold is desirable because it is highly conductive, but it does not grow epitaxially. A conductive material which is closely lattice-matched with the base electrode, does not create a high surface resistance at the interface, grows uniformly even at thicknesses of 100-200 Å, and which can be patterned would be an ideal candidate.

- (d) *Counter electrode* - The counter electrode needs to grow epitaxially on the barrier in the edge junction configuration and must grow uniformly. In SNS edge junctions, it is of the same material as the base electrode. This material must be able to withstand ion milling and patterning without degradation. It may not degrade during deposition of subsequent layers nor upon exposure to the atmosphere. Table VI shows a comparison of YBCO to some typical substrate, insulator, and barrier materials used in YBCO edge junctions.

BKBO has the great advantage of possessing isotropic properties. It has the disadvantage, however, of requiring the much-more-expensive liquid helium as a cryogen. Many of the challenges of working with YBCO have been overcome. Growing *c*-axis-oriented YBCO films, which can be done rather easily, as long as a thickness of 4000 Å is not exceeded [154] or impurities or surface roughness are not present, all of which tend to nucleate *a*-axis grains, allows one to utilize the longer coherence length in the *a* and *b* directions for conduction across the edge junction barrier. The greater expense of lower operating temperatures for BKBO can only be justified if BKBO junctions can be made more reproducibly than YBCO ones. This

Table VI. Properties of typical substrate, insulator, and barrier materials compared to those of YBCO

material	purpose	$T_c$	pseudocubic lattice param (Å)	coeff. of thermal exp. ( $\times 10^{-6}/K$ )	dielectric constant at RT
LaAlO <sub>3</sub>	substrate	----	$d_{100}(c)=$ $d_{012}(h)=$ 3.792 [146]	31.8 [147]	16-23 [151]
NdGaO <sub>3</sub>	substrate	----	$d_{110}(o)=$ $d_{100}(c)=$ 3.855 [146]	9.96 [149]	24
SrTiO <sub>3</sub>	insulator	----	3.905 [146]	11 [148]	200-300 [151]
PBCO	barrier	----	$a=3.864$ $b=3.911$ $c=11.694$ [155]	----	----
Co/YBCO	barrier	53 [156]	$a=b=3.8675$ $c=11.684$ [156]	----	----
YBCO	electrodes	93 [157]	$a=3.827$ $b=3.877$ $c=11.708$ [157]	11.8 [158]	----

is greatly inhibited by the degradation of BKBO upon exposure to the atmosphere as well as the difficulty in deposition of this material due to the volatility of the potassium and the inconsistency and degradation of sputtering targets made from this material.

## B. Methods

The purpose of this project is to study the structural, chemical, and electronic properties of superconducting BKBO and YBCO thin films and junctions and to obtain an understanding of device physics.

1. Of great importance is the determination of whether there is a substrate-film reaction. Auger depth profiling was used to study this.
2. It is important to study surface morphology and composition of the base electrode (superconducting film) because a smooth, clean surface without high resistance is necessary for junction uniformity. The techniques used in this determination were reflective high-energy electron diffraction (RHEED), low-energy electron diffraction (LEED), scanning electron microscopy (SEM), atomic force microscopy (AFM), energy-dispersive x-ray spectroscopy (EDXS), and x-ray photoelectron spectroscopy (XPS). The entire film must be epitaxial with respect to the substrate and well-oriented so that there are no high-angle grain boundaries present and so that the electrons have a clean path through the film. In-plane and growth-direction orientation were determined by x-ray diffraction (XRD), and resistivity was measured using the van der Pauw technique. In addition, films were patterned for critical current-density measurements.
3. Uniform barrier growth is another important consideration for device quality. The barrier was observed by RHEED and LEED and studied by electronic measurements of the junction (pinholes will result in shorting) as well as by modelling of the I-V data. The barrier may not react with the superconductor; interfacial chemistry was determined by XPS. In addition, the barrier must grow epitaxially. XRD was used to observe its orientation.
4. The counter electrode must possess the same qualities as the base electrode and must be epitaxial with respect to the barrier and well-oriented. XRD was used in this determination. A van der Pauw measurement of the entire trilayer structure is representative of the resistivity of the top electrode only, if there are no pinholes in the barrier. Measurements of I-V characteristics and conductance curves across the patterned junction yield information about junction behavior,



i.e., which conduction mechanisms are governing the junction behavior. For example, from the I-V curve, one can see whether there are leakage currents present, whether the junction is highly resistive ( $I_C R_N$  products are an indication of junction quality), whether the junction has a great deal of capacitance, and whether the junction is RSJ-like or flux-flow-like. The I-V data can be incorporated into the Simmons model, discussed in Appendix II, to determine barrier height and thickness. Radiation can be applied to see if there are Shapiro steps present in the I-V curve. These occur as a result of the ac Josephson effect, in which the addition of radiation causes the superconducting electrons to become oscillators, as discussed in Chapter I. Such a response is shown in Figure 41.

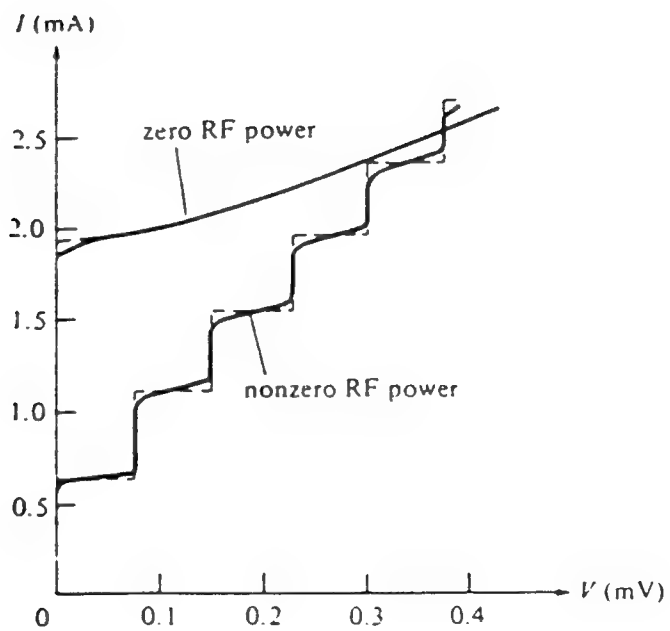


Figure 41. I-V characteristic for a junction with 35 GHz applied rf power. Solid lines show experimental results. Broken lines give results of calculations without noise [159].

## Chapter IV. Experimental techniques

### A. Review of experimental methods

#### 1. *rf magnetron sputtering*

In this technique, power at radio frequency is used to generate a signal of alternating polarity. This signal is applied to the target, so that positive ions and electrons are alternatively accelerated toward the insulating target (such as  $\text{Ba}_{0.6}\text{K}_{0.6}\text{BiO}_x$ ), which acts as the cathode. A magnetic field is used to confine the plasma to a space near the target so that there is a greater efficiency of electrons bombarding the target and knocking off target atoms. The plasma consists of electrons, atoms sputtered from the target, and also atoms, ions, and free radicals of the sputtering gas (in the case of BKBO, this is argon and oxygen; for YBCO, this is Ar,  $\text{O}_2$ , and  $\text{H}_2\text{O}$ ). The material which is removed from the target is subsequently deposited on the substrate. Figure 42 depicts the sputtering process.

The first chamber used in the deposition of BKBO films and junctions is shown in Figure 43. It is a Riber system with capabilities for sputtering, electron-beam evaporation, and *in-situ* analysis by XPS, RHEED, and LEED. The second chamber, used for BKBO, YBCO, and Co/YBCO films, was constructed by me and is depicted in Figure 44. A motor attached to a pulley and crankshaft at the top of the chamber provided  $180^\circ$  rotation of the heater assembly every hour. The heater assembly, to which a substrate-mounted block was attached, is spring-loaded with grooves in which the block rests. A thermocouple was threaded through this assembly so that the thermocouple was in close proximity to the back of the block. The sputtering configuration was an off-axis one; this means that the heater assembly and sputtering gun were at  $90^\circ$  to each other. A vacuum was obtained by

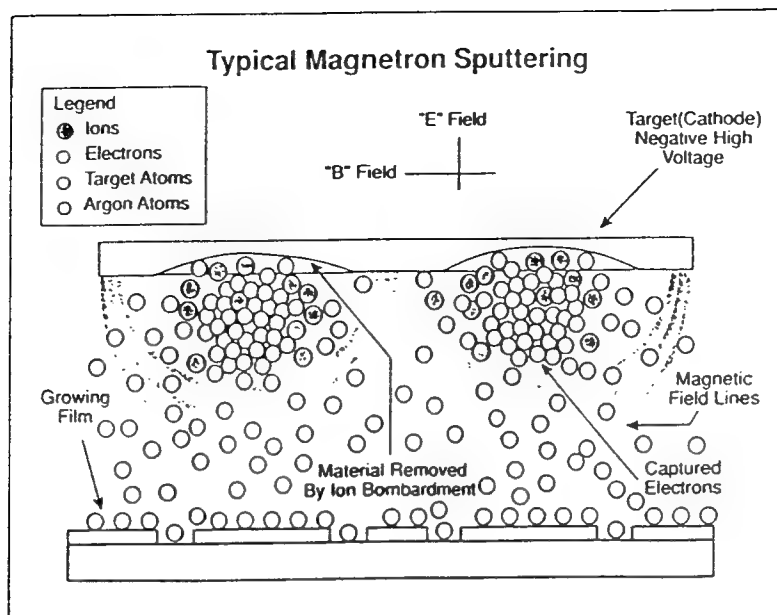


Figure 42. Depiction of magnetron sputtering process [160].

### SUPERCONDUCTOR DEPOSITION AND ANALYSIS FACILITY

- Five UHV chambers
- Vacuum transfer

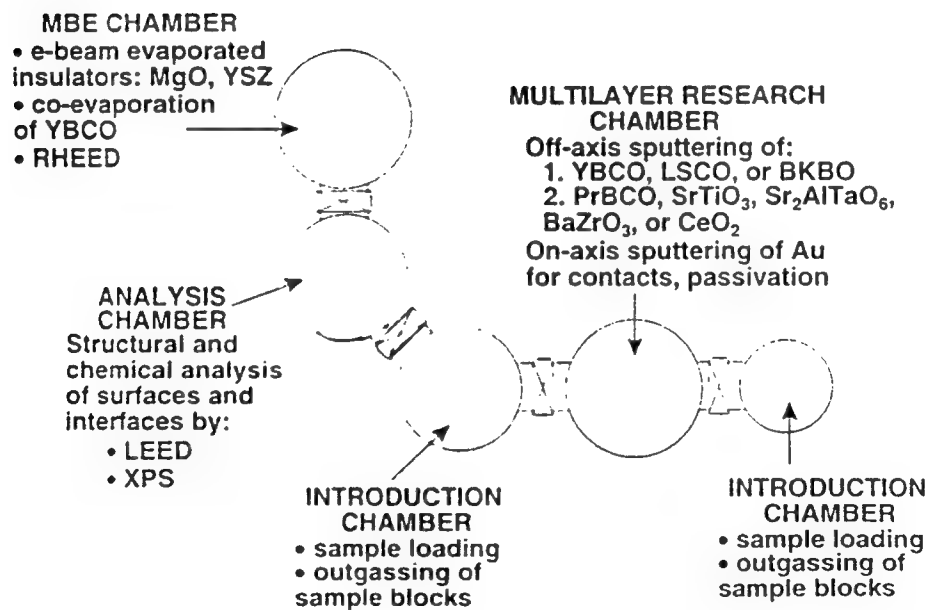


Figure 43. Ribier chamber with sputtering and evaporation capabilities and *in-situ* RHEED, LEED, and XPS.

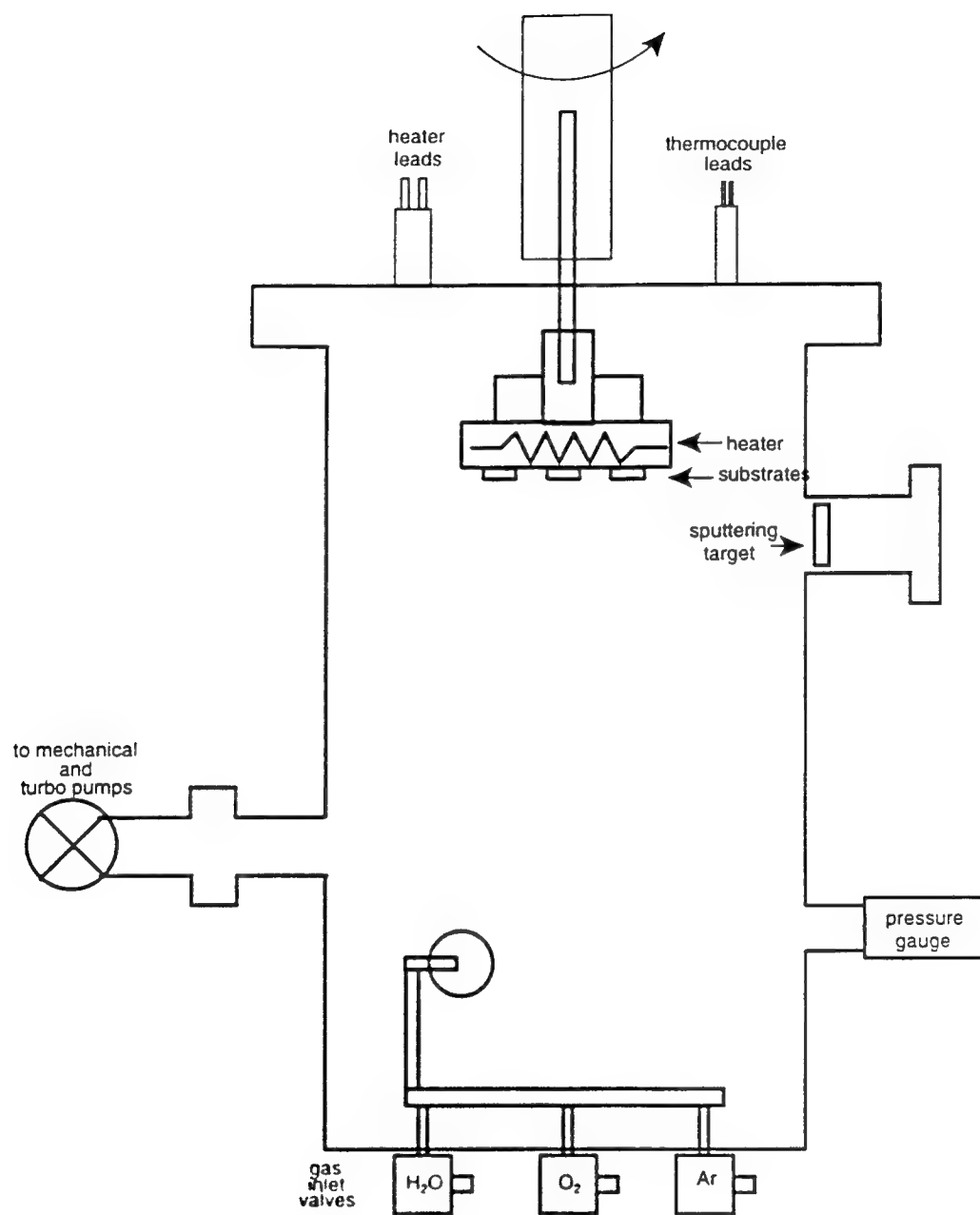


Figure 44. The chamber used for sputter deposition of BKBO and YBCO films.

roughing with a mechanical pump (from atmospheric pressure to  $\sim 20$  mTorr) and then using a turbo pump to reach pressures of  $\sim 1 \times 10^{-5}$  Torr. Both Baratron (which senses a plate displacement) and ionization (detecting the number of ions) gauges were used in pressure determination.

## 2. XPS

Surface analysis by x-ray photoelectron spectroscopy involves the irradiation of a sample *in-situ* with monoenergetic x-rays (either Mg K $\alpha$  x-rays of 1253.6 eV or Al K $\alpha$  x-rays of 1486.6 eV). These x-rays interact with the constituent atoms by the photoelectric effect and cause the emission of characteristic photoelectrons. The emitted electrons have kinetic energies given by  $KE = h\nu - BE - \phi_s$  where  $h\nu$  is the energy of the photon,  $BE$  is the binding energy (ionization energy) of the atomic orbital from which the electron originates, and  $\phi_s$  is the spectrometer work function. In addition, Auger electrons are emitted by the relaxation of energetic ions left after photoemission. Figure 45 shows ionization processes for iron and uranium. The Fermi level corresponds to zero binding energy. The depth beneath it is the binding energy of the particular electron. The lengths of the lines indicate the relative probabilities of the various ionization processes. The p, d, and f levels become split upon ionization, leading to holes in the  $p_{1/2}$ ,  $p_{3/2}$ ,  $d_{3/2}$ ,  $d_{5/2}$ ,  $f_{5/2}$ , and  $f_{7/2}$  states in the ratios of 1:2 for p levels, 2:3 for d levels, and 3:4 for f levels, respectively.

Scans are done qualitatively by sweeping the entire spectrum and identifying the resulting peaks in order to determine composition. A typical survey scan is shown in Figure 46. Spectra can also be used somewhat more quantitatively by sweeping certain energy windows, which are chosen by selecting predominant peaks for each of the constituent elements (for example, the highest Ba are the 3d peaks at binding energies of 779.65 and 795.05 eV, so one would choose this as one window,

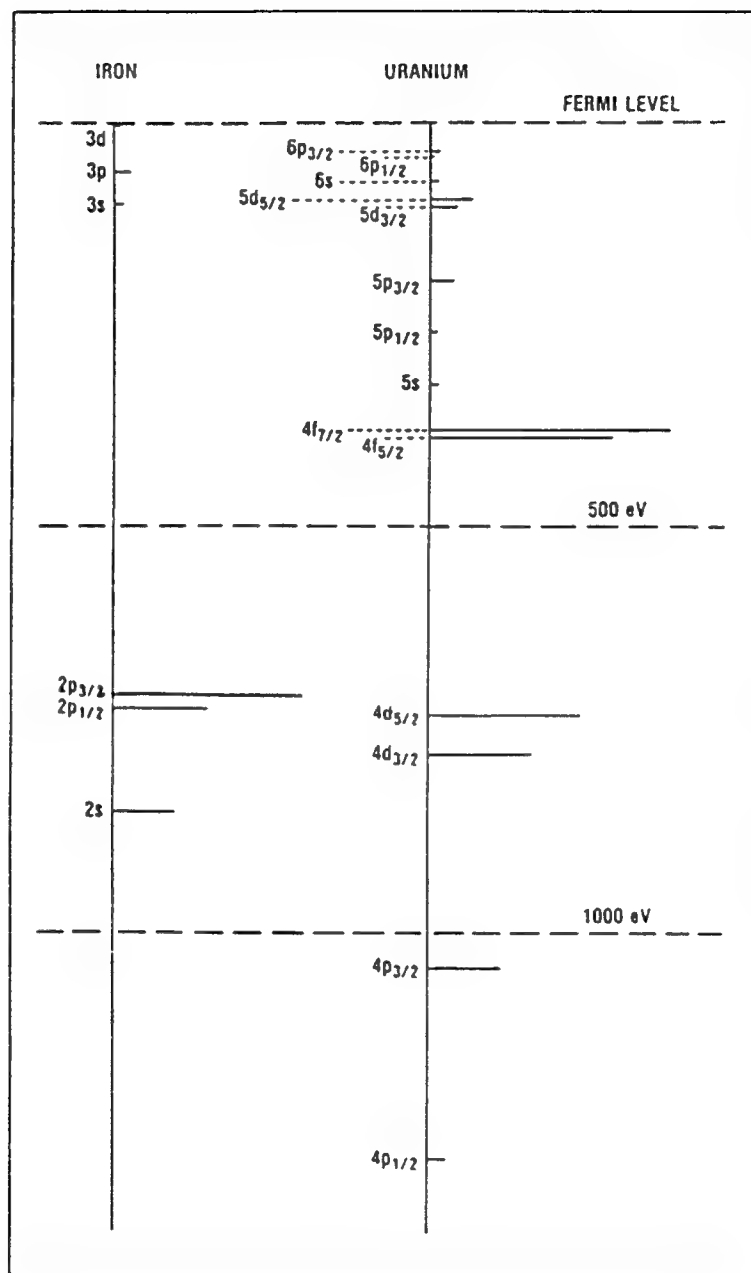


Figure 45. Ionization energies for iron and uranium, where the depth of the state below the Fermi level is proportional to the ionization energy [161].

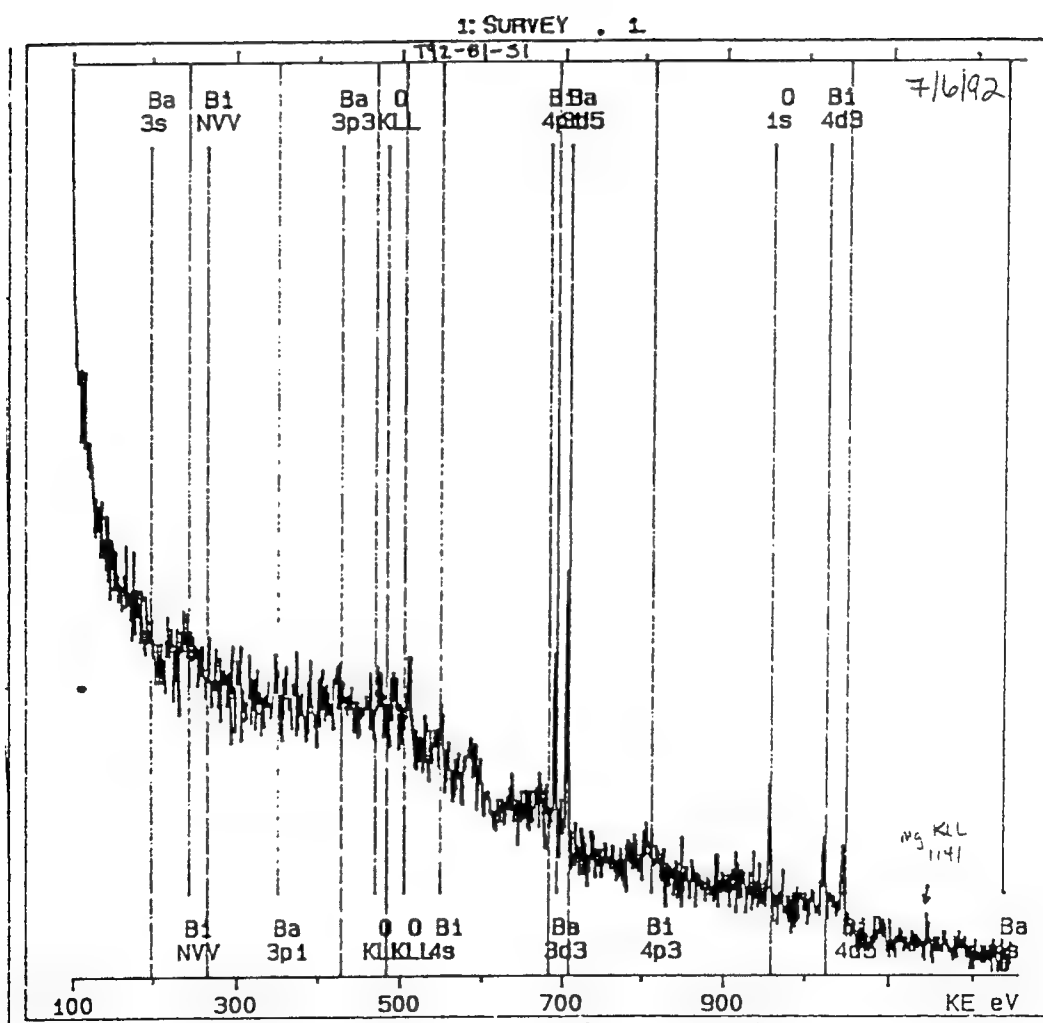


Figure 46. XPS survey scan of a BKBO film with Ba, Bi, and O lines identified.



the K 2p peaks at ~294 eV for a second, the Bi 4f peaks at ~160 eV as another, and the O 1s peak at 531.6 eV as a fourth; see Figure 47). The peak heights obtained in each window cannot be directly compared without considering Atomic Sensitivity Factors in the following manner [161]:

$$\frac{n_1}{n_2} = \frac{I_1 / S_1}{I_2 / S_2} \quad (25)$$

where  $n_i$  = the number of atoms of the element per  $\text{cm}^3$  of sample,  $I_i$  = the number of photoelectrons per second in a specific spectral peak, and  $S_i$  = the atomic sensitivity factor, which accounts for the fact that radiation from less-energetic elements can be absorbed more easily by the matrix. In addition, a scan with the same energy windows of the sample under a different condition (for example, after annealing) could be compared to the previous scan. The difference in peak heights could be compared to determine relative variations in composition. Peak positions can also be compared from one scan to another in order to determine whether a chemical reaction has occurred. For example, an oxidation reaction will shift the peaks to higher binding energies, whereas a reduction reaction will cause a lowering of peak energies.

### 3. EDXS

EDXS is another compositional analysis technique. It probes farther into the sample than XPS, which is merely surface-sensitive. EDXS involves the bombardment of the sample with electrons and consequent ejection of characteristic x-rays. When the electron beam strikes an atom, an inner-shell electron may be ejected. To return the atom to its lowest energy state, an outer-shell electron (of

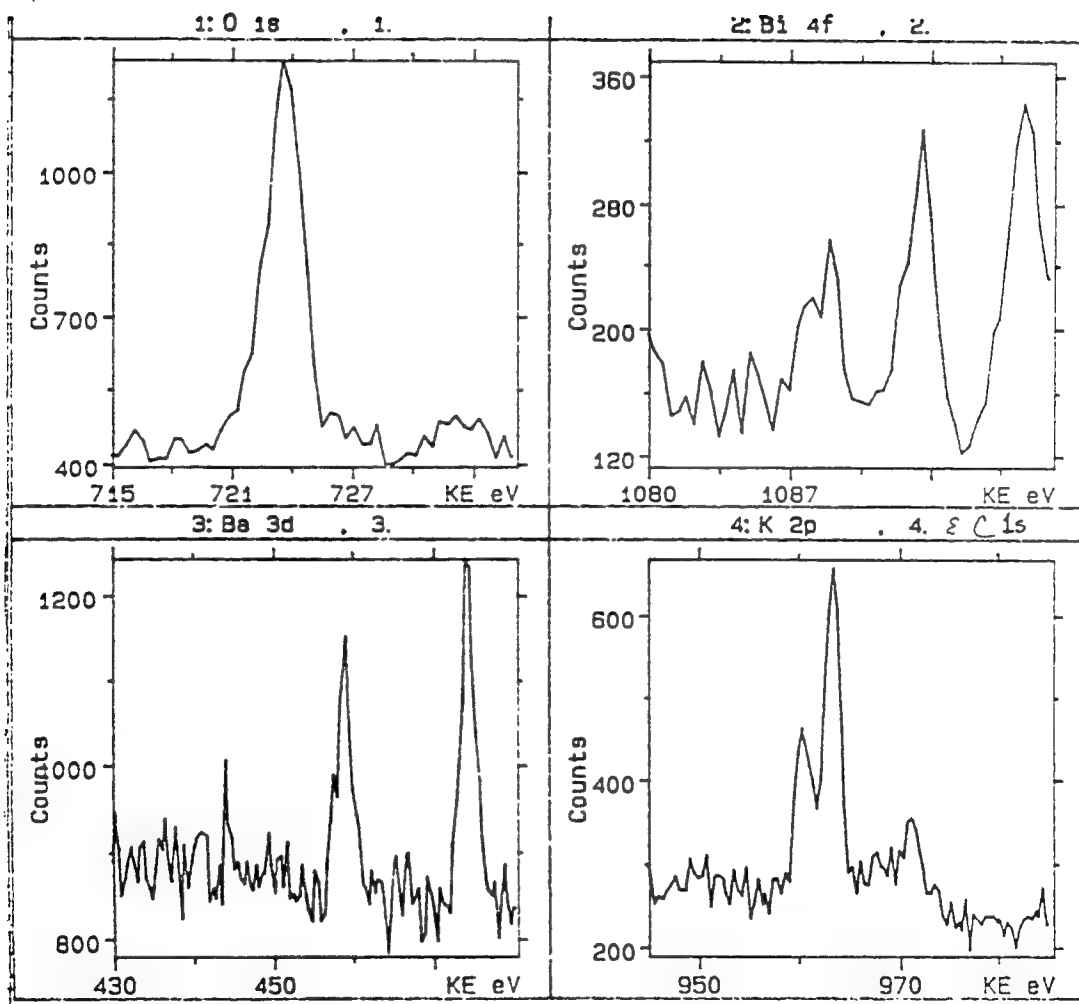


Figure 47. XPS scan with distinct energy windows for the elements present in the BKBO film observed.

greater energy) will drop down to fill the vacancy in the lower-energy shell. This process will release an x-ray with energy equal to the difference between the initial and final energy of the electron which has dropped. The energy will be characteristic of the element for which the transition occurs. Figure 48 depicts this process.

Both qualitative and quantitative analysis can be done with EDXS. The former is used to determine which species are present in the sample; the latter tells the amount of each present. For thin films, the "standardless" analysis is typically used. A background is subtracted from the spectrum before it is analyzed by the software. Peaks are deconvoluted, a "ZAF" correction is applied (where Z = atomic number, A = absorption, and F = fluorescence) and atomic sensitivity factors are taken into account. Then the atomic percent of each element present is given [162].

#### 4. RHEED and LEED

Electron diffraction from a lattice is often represented in a reciprocal lattice configuration using the Ewald sphere construction. These constructions for LEED and RHEED are shown in Figures 49 and 50. The Ewald sphere represents conservation of energy of the incident electron beam and can be depicted by either wavelength- ( $\lambda_{in} = \lambda_{out}$ ) or by momentum conservation ( $|k_0| = |k|$ ). The superposition of the Ewald sphere on the reciprocal lattice portrays the Laue condition,  $S = G_{hkl}$ , where  $S = k - k_0$  is the momentum transfer which occurs during elastic scattering of radiation from the rigid crystal, and  $G_{hkl}$  is a reciprocal-lattice vector (distance between points in the reciprocal lattice). When this condition exists, the points in the reciprocal lattice which are intersected by the Ewald sphere will be diffraction spots observed in the electron diffraction pattern [163]. An explanation of the indexing of such patterns is given in Appendix III. Analysis by LEED and RHEED was done *in-situ* so that each junction layer could be observed without

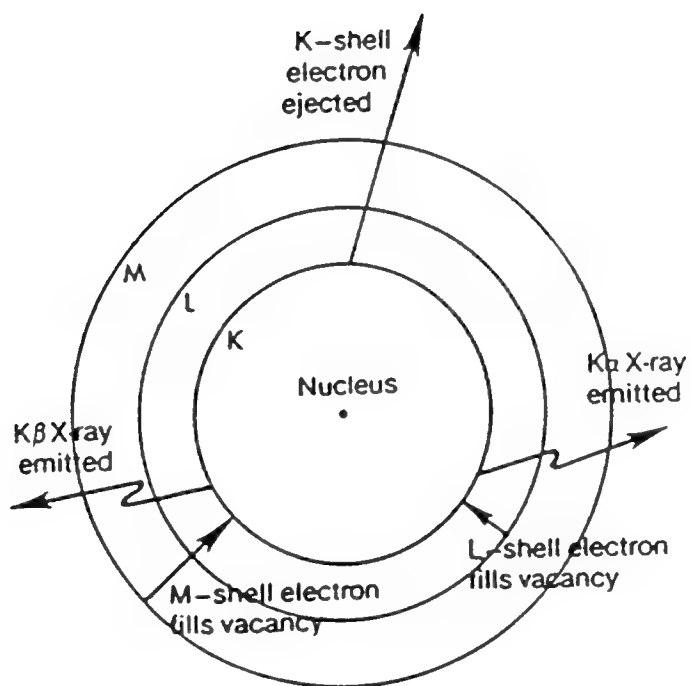


Figure 48. Depiction of the generation of x-rays by interaction of electromagnetic radiation with an atom, using the Bohr model of the atom [162].

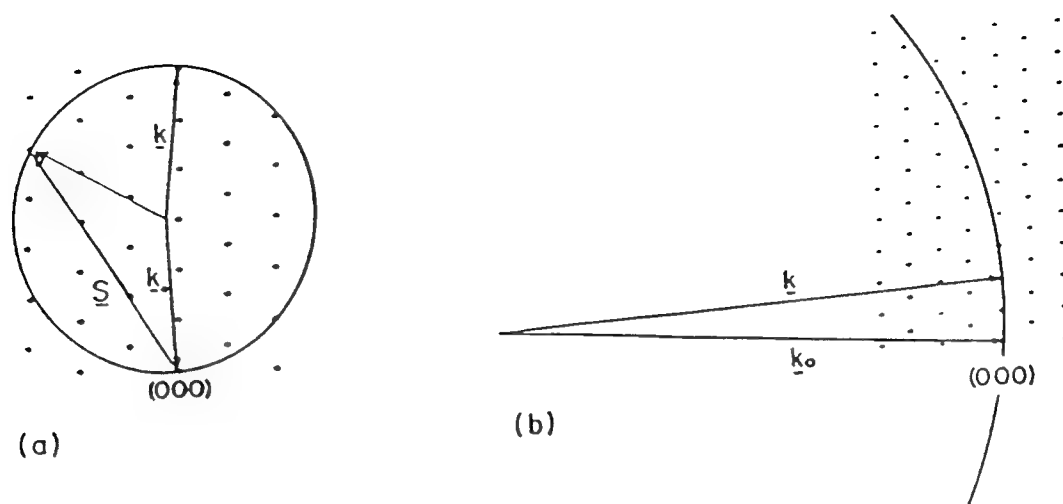


Figure 49. Reciprocal lattice and Ewald sphere constructions. Diffraction geometry and momentum shown are appropriate for (a) LEED (b) RHEED [163].

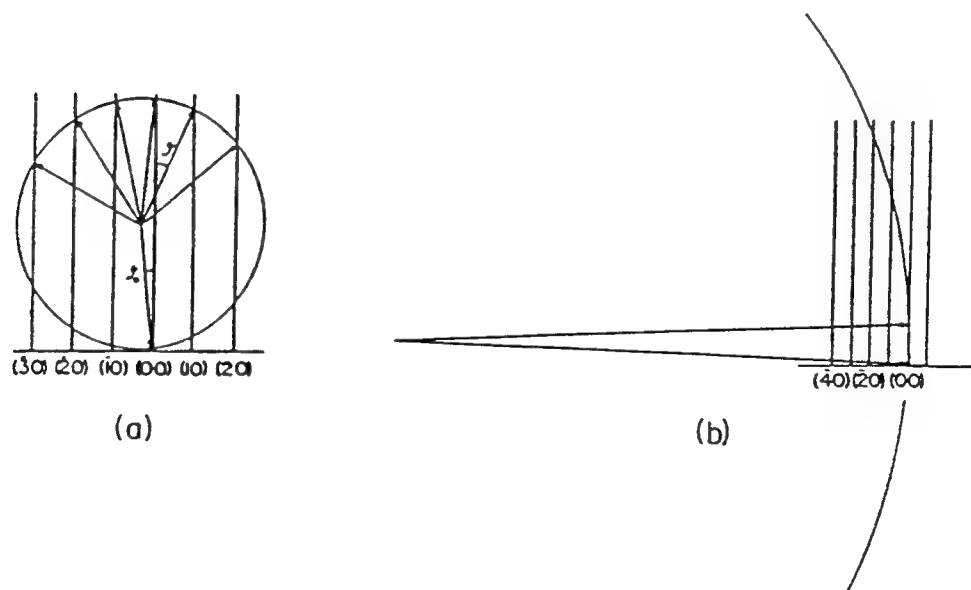


Figure 50. Reciprocal lattice for a single plane of atoms, for which the reciprocal lattice is a set of rods normal to the plane of the layer, and Ewald construction for (a) LEED (b) RHEED [163].

breaking vacuum.

## 5. X-ray diffraction

In a normal two-circle diffractometer, any movement of the sample must be accompanied by a concomitant movement of the detector by twice as much. For example, if the sample is tilted by  $5^\circ$ , the detector must be moved by  $10^\circ$  in order to ensure that the angle of incidence (angle between the source and sample, which has become  $(\theta + 5^\circ)$ ) equals the angle of reflection (which is the angle between the sample and detector). This type of diffractometer is thus referred to as a  $\theta - 2\theta$  type.

The Philips "X-Pert" System, however, incorporates a four-circle diffractometer which allows  $\omega$  to be varied independently of  $2\theta$  by moving the detector with respect to the source. In addition,  $\phi$  and  $\psi$  may be varied by rotating the sample  $360^\circ$  about the vertical and by tilting the sample stage about the horizontal, respectively. These angles as well as the allowed measurement region are depicted in Figure 51. The parallel-beam optics shown in Figure 52 allow measurements of phase composition, twinning, texture, and stress.

In order to determine the region of reciprocal space to be studied and what the optimum  $\omega$ ,  $2\theta$ , and  $\phi$  should be, one can utilize the reciprocal space map shown in Figure 53. From the allowed areas, one chooses a certain (hkl) to be measured. As shown in Figure 54,  $\omega$  is the angle between the incident beam from the source and the horizontal. The detector is at an angle  $2\theta$  from the projected incident beam (where it would be were it able to go through the sample). The (303) plane is at  $45^\circ$  from the vertical in real space, and the ray in Figure 54 points to where this reflection would be found on the reciprocal space map. The length of the ray (distance from the point to the origin) is determined by the d-spacing of the planes in the crystal and

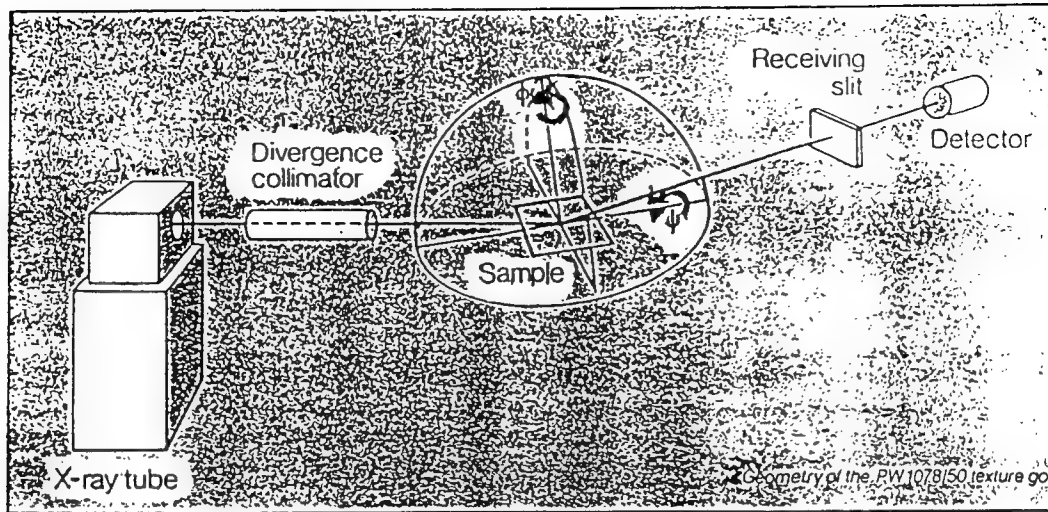


Figure 51. Allowed volume of measurement in diffraction space with  $\phi$  and  $\psi$  angles depicted [164].

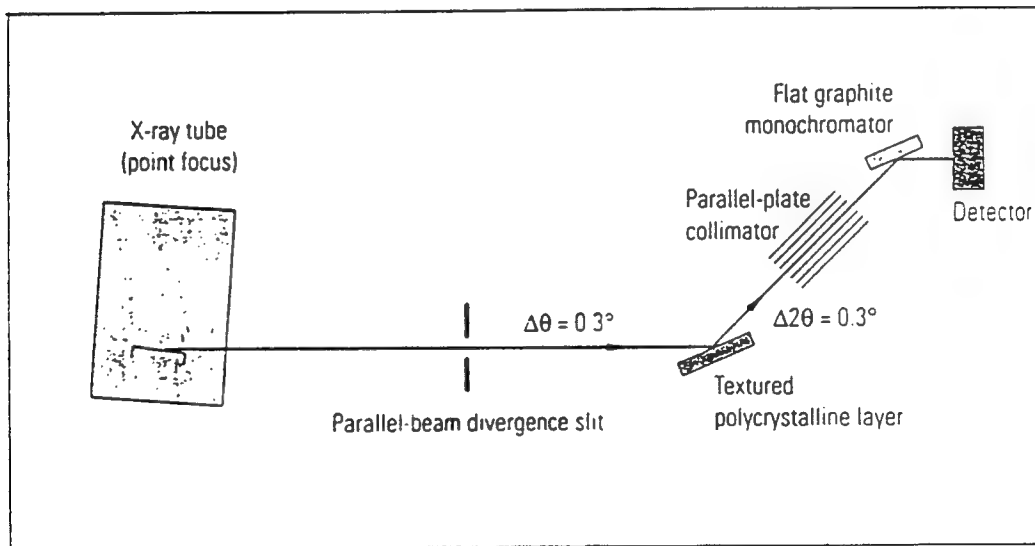


Figure 52. Schematic of instrument with parallel beam optics employed in measurement of highly textured films [164].

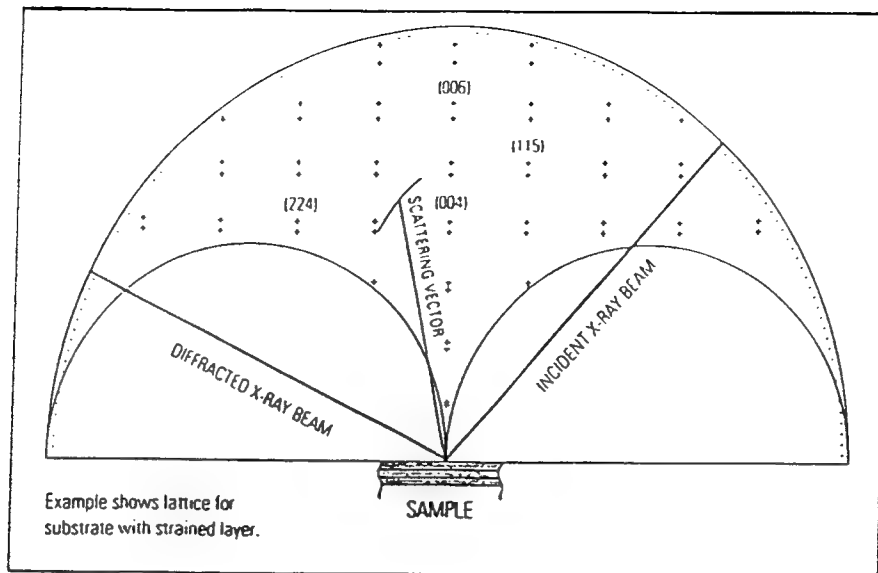


Figure 53. Reciprocal space map used in determination of measurement parameters.

One chooses the desired (hkl) with the cursor in the allowed region and is presented with the optimum  $2\theta$ ,  $\omega$ , and  $\phi$  angles based on a pre-defined unit cell of expected dimensions [164].

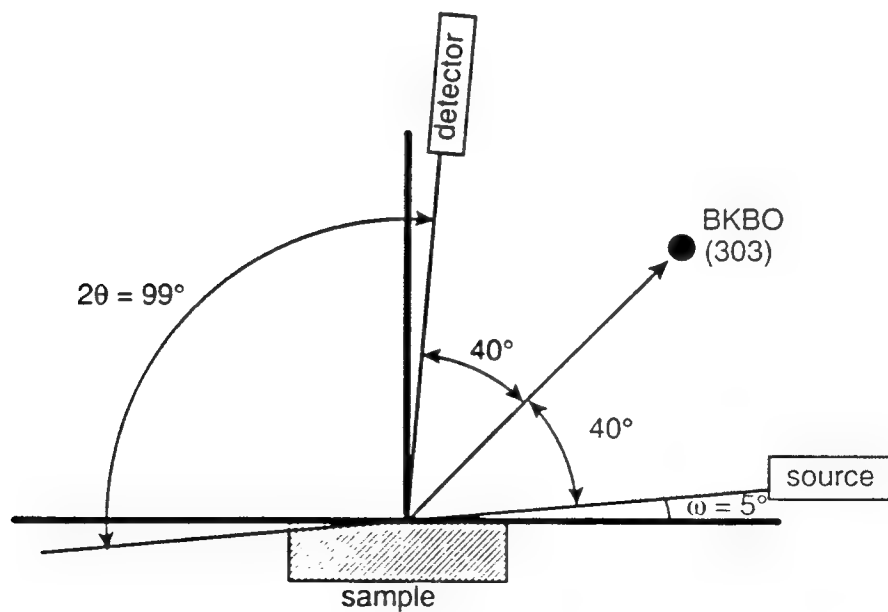


Figure 54. Diagram of diffractometer positions for a BKBO (303) reflection to be observed.



the orientation of the ray represents that of the plane in the crystal. The angle between the source and the ray must equal the angle between the ray and the detector, so that the angle of incidence equals the angle of reflection. Since  $2\theta$  is set by the d-spacing,  $\omega$  must be adjusted so that these requirements are met.

If  $\omega$  is fixed at  $1/2(2\theta)$ , then only planes parallel to the film surface are observed. When  $\omega$  can have some other relationship to  $2\theta$ , then any reflections within the allowed region of reciprocal space may be observed. Scanning  $\omega$  will yield information about rocking curve widths. The mosaic spread in the vertical direction,  $\Delta\omega_1$ , is found by keeping  $2\theta$  constant and scanning  $\omega$ . This gives an indication of the deviation of grains whose axes are not parallel to the plane normal. Fixing  $2\theta$ ,  $\phi$ , and  $\psi$  and scanning  $\omega$  allows one to observe the mosaic spread in the plane of the film,  $\Delta\omega_2$ . Tilting  $\psi$  allows one to take a plane at some arbitrary angle and tilt it until it is vertical. Rocking  $\omega$  will then show variations from the vertical which are actually deviations from an in-plane direction. The two types of rocking-curve widths are shown in Figure 55.

Varying  $\phi$  allows one to scan all of the  $\{hkl\}$ 's in  $360^\circ$ , for example, the  $(101)$ ,  $(011)$ ,  $(\bar{1}01)$ , and  $(0\bar{1}1)$ . If one compared  $\phi$  scans of similar peaks for the substrate and film, one could determine the epitaxial (or lack thereof) relationship between the two. Orientation of the film in the growth direction can be determined by a  $2\theta$  scan, and a calculation of the lattice parameter can be made from this scan as well. Area scans of  $2\theta$  vs.  $\omega$  and also  $\psi$  scans are useful in studying anisotropic compounds; for example, the former would be helpful in determining the  $a$  and  $b$  lattice parameters for an orthorhombic material. This would be done by finding the optimum  $2\theta$ , then using Bragg's Law,  $n\lambda = 2d \sin \theta$ , to obtain the d-spacing and then using the equation below for an orthorhombic material [165]:

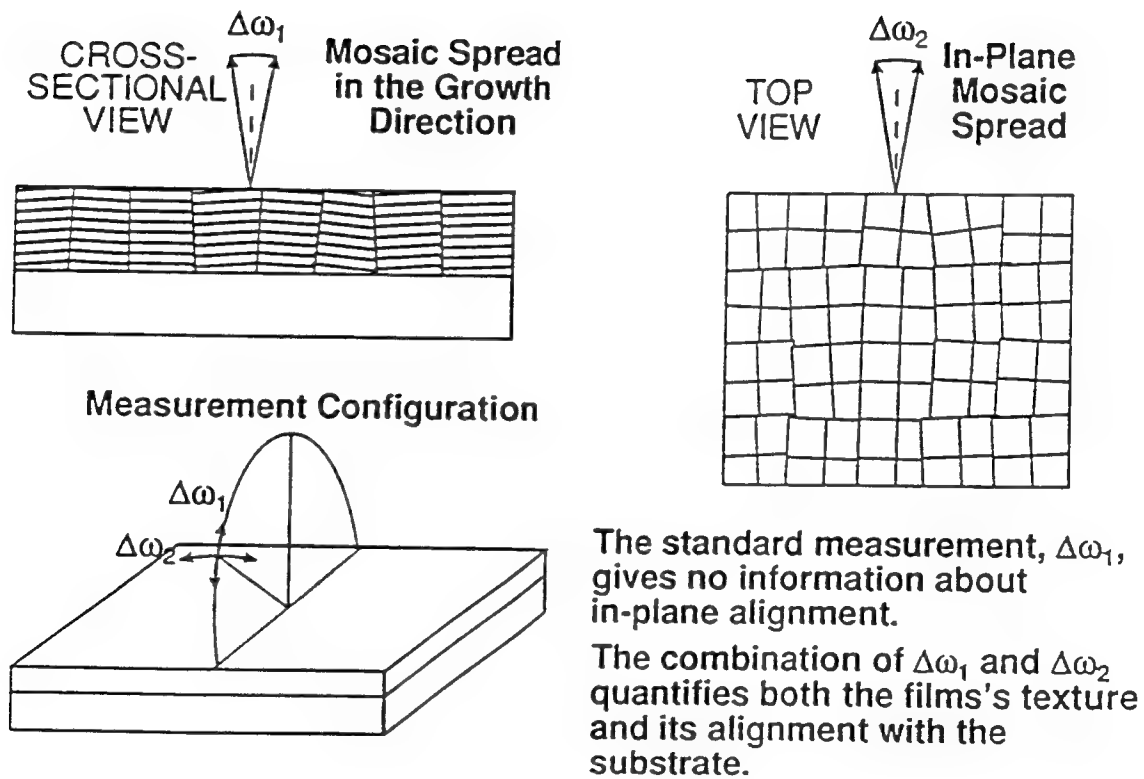


Figure 55. Schematic of rocking curve width measurements for the growth direction and in the plane of the film.

$$\frac{1}{d^2} = \frac{h^2}{a^2} + \frac{k^2}{b^2} + \frac{l^2}{c^2} \quad (26)$$

A  $\psi$  scan could be used to discover whether a film of such a material was oriented with all  $c$ -axes parallel to the growth direction. A  $\psi$  scan of YBCO, for example, will show the (104) peak at  $37^\circ$  for  $c$ -axis-oriented grains and at  $54^\circ$  for  $a$ -axis oriented grains.

#### 6. Resistivity measurements

The van der Pauw technique was used in resistivity vs. temperature measurements. This method is based on the premise that the resistivity of an arbitrary shape can be measured without knowing the current path as long as the following considerations are met:

- (a) the contacts are at or very near the edge(s) of the sample
- (b) the contacts are sufficiently small
- (c) the sample thickness is homogeneous
- (d) the sample does not have isolated holes

Define  $R_{AB,CD}$  to be the resistance resulting from the potential difference between the contacts D and C per unit current through the contacts A and B. Then the following equation holds [166]:

$$\exp(-\pi R_{AB,CD}d/\rho) - \exp(-\pi R_{BC,DA}d/\rho) = 1 \quad (27)$$

where  $d$  is the sample thickness and  $\rho$  is the resistivity of the material. It follows that to measure resistivity of a flat sample, one needs to make four small contacts along

the circumference of the sample and to measure the thickness of the sample and the resistances  $R_{AB,CD}$  and  $R_{BC,DA}$ . The resistivity will be of the form given below:

$$\rho = \frac{\pi d}{\ln 2} \frac{(R_{AB,CD} + R_{BC,DA})}{2} f\left(\frac{R_{AB,CD}}{R_{BC,DA}}\right) \quad (28)$$

where  $f$  is a function of the ratio  $R_{AB,CD}/R_{BC,DA}$  only and satisfies the relation

$$\frac{R_{AB,CD} - R_{BC,DA}}{R_{AB,CD} + R_{BC,DA}} = f \operatorname{arccosh} \left\{ \frac{\exp(\ln 2 / f)}{2} \right\} \quad (29)$$

If the contacts are made at a distance  $d$  inside the circumference of the sample, the error in resistivity obtained will be the following [166]:

$$\frac{\Delta \rho}{\rho} = \frac{-d^2}{2D^2 \ln 2} \quad (30)$$

where  $D$  is the diameter of the sample.

In the measurements reported in this document, a default current of 100  $\mu\text{A}$  was used. The polarity of the contacts was switched every 3-5 seconds in order to cancel the effects of thermally induced electric fields. Silver paint was applied to the sample for contacts and Cu-alloy clips which could be tightened were used as the probe contacts. The entire probe was lowered into a dewar of liquid helium in order to decrease the temperature.

## *7. Inductance measurements*

Inductance vs. temperature was used as an additional means of measuring the superconducting transition temperature. A copper coil was placed directly over the sample and received a 100 kHz signal from a lock-in amplifier. When the sample becomes superconducting, currents circulate on the surface of the material (around each grain) in order to expel magnetic flux. This will change the inductance in the copper coil.

The resistive transition occurs at a higher temperature than the inductive. As soon as any superconducting electrons find a continuous path across the sample, a resistive transition is seen. The whole sample must become superconducting, however, before an inductive transition occurs.

## *8. Critical current density measurements*

A typical mask drawing used to pattern films for  $J_c$  measurements is shown in Figure 56. Patterning was done by Ar ion milling. The two I and two V contacts of the  $T_c$  probe were placed separately on different pads of the patterned film in order to measure  $J_c$  as a function of temperature.

A current of 1  $\mu\text{A}$  was applied to the sample. The criterion for establishing the value of the critical current was that it would be the value found at ( $I_c$ , 1  $\mu\text{V}$ ) on the I-V curve if and only if 1  $\mu\text{V}$  were less than a corresponding resistivity of  $10^{-11} \Omega \cdot \text{cm}$ .

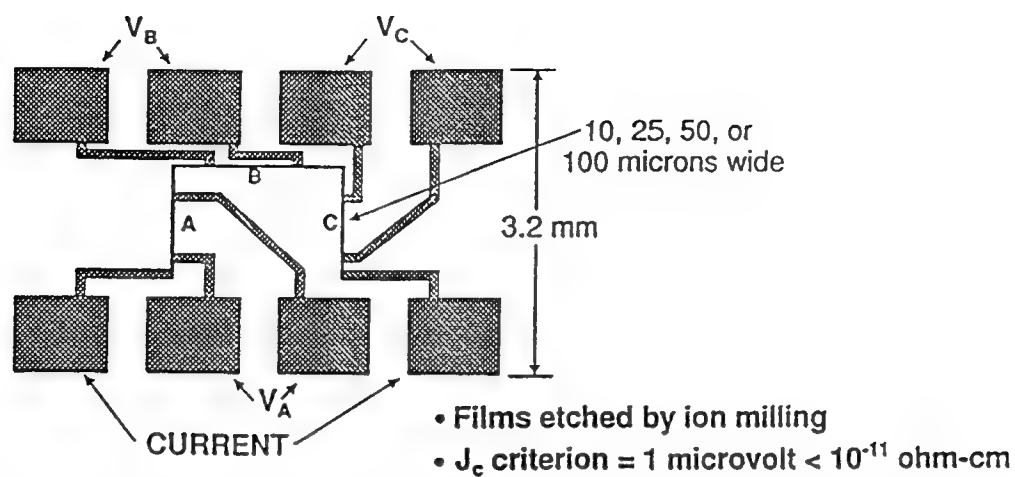


Figure 56. Configuration of the mask used to pattern films for critical current density measurements.

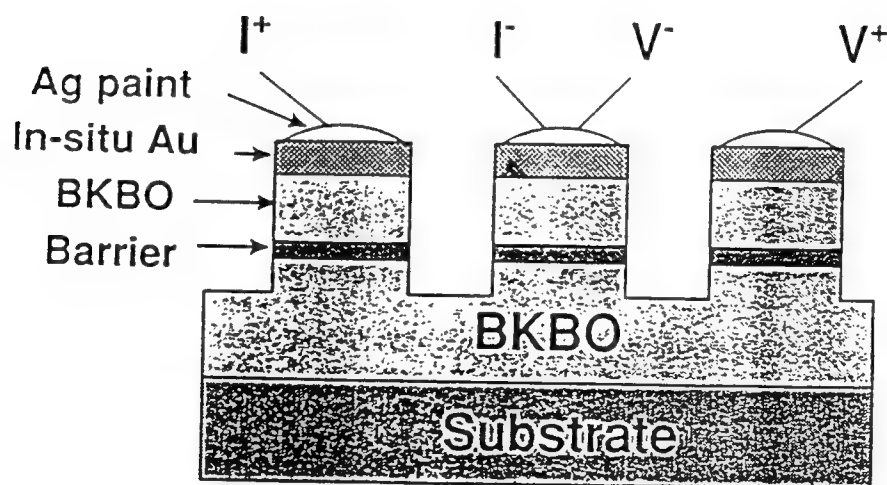


Figure 57. Schematic of the configuration used in BKBO tunnel junction measurements [171].

## 9. *Junction measurements*

Measurements of the electrical properties of BKBO junctions were done by utilizing the same probe used for  $T_c$  measurements. One set of I and V contacts (I+, V+), were placed on the same junction area while the other contacts (I- and V-) were placed separately on different areas. This is shown in Figure 57. In such a configuration, which was patterned by Ar ion milling, one can measure the resistance through the junction as well as across the BKBO base electrode. A current supply was used to generate the signal in order to measure the I-V characteristic. In addition, a lock-in amplifier and differential amplifier were used when measuring conductance curves. The lock-in amplifier works by sending out a weak periodic signal (in this case, the frequency used was 105 Hz). The weak signal is amplified to distinguish it from noise and is then phase-detected relative to the modulating signal [167].

More sophisticated photolithography was used to pattern YBCO junctions. The gold contacts on these junctions were wire-bonded to gold pads on a disk in a twisted-pair arrangement which avoids noise from outside magnetic fields. This assembly was mounted on a probe and a current supply and oscilloscope were used to measure the I-V characteristics. A microwave oscillator was utilized in the observation of Shapiro steps.

### B. Film Fabrication

The substrates used included  $\text{LaAlO}_3$  (001),  $\text{MgO}$  (001),  $\text{Al}_2\text{O}_3$  ( $1\bar{1}02$ ),  $\text{NdGaO}_3$  (110) or (001),  $\text{SrTiO}_3$  (001), and  $\text{SrTiO}_3$  (011). These were mounted on a Ni block with silver paint. The block was then heated at  $\sim 100^\circ\text{C}$  for one hour, and at  $\sim 140^\circ\text{C}$  and  $\sim 210^\circ\text{C}$  for 20 minutes each on a hot plate to secure the adhesion and

ensure uniform thermal contact of the substrates to the block. The blocks were heated resistively in the chamber, first to  $\sim 800^{\circ}\text{C}$  in order to clean the substrates and then to the appropriate deposition temperature. All films were deposited by rf magnetron sputtering from pressed and sintered ceramic targets. Samples were rotated throughout the entire run in each case. A post-anneal in 1 atmosphere of oxygen at  $400^{\circ}\text{C}$  followed every deposition. It is important that this anneal be carried out at a relatively low temperature in order to retain the volatile potassium and to prevent precipitation of the  $\text{KBiO}_2$  phase, which occurs at  $500^{\circ}\text{C}$  for  $\text{Ba}_{0.6}\text{K}_{0.4}\text{BiO}_3$ [168].

The first BKBO films were deposited by rf magnetron sputtering in an off-axis configuration with a stoichiometric ( $\text{Ba}_{0.6}\text{K}_{0.4}\text{BiO}_3$ ) target used in conjunction with a  $\text{KO}_2$  target. Pressures of 20 mTorr  $\text{O}_2$  and 30 mTorr Ar (and variations of these), a gun power of 40 W, and deposition temperatures of  $200\text{--}400^{\circ}\text{C}$ , as well as room temperature, were used. The films were unstable in air and despite the use of a second source of potassium were determined by EDX to be potassium-deficient. The use of a quartz crystal monitor showed the flux from the  $\text{KO}_2$  target to be very small, so a KOH evaporation source was used instead. This also resulted in K-deficient films. A target with a stoichiometry of  $\text{Ba}_{0.6}\text{K}_{1.2}\text{Bi}_{1.4}\text{O}_x$ , which had been used successfully in fabricating SIN junctions [77], was then used in a position  $45^{\circ}$  from the substrates. This target along with pressures of 1 mTorr  $\text{O}_2$  and 50 mTorr Ar and a deposition temperature of  $\sim 350^{\circ}\text{C}$  were used to successfully fabricate superconducting films with 15.2 K transition temperatures (at  $R=0$ ). This target degraded over time, however, and results were not reproducible. The later use of higher pressures and the same configuration again produced superconducting films. The ratio of oxygen to argon pressures was varied from 1/4 to 2/3 to 1; the latter produced films with the highest  $T_c$  of the three, which was 15.7 K. A substrate



temperature of  $\sim 400^\circ\text{C}$  was used.. However, a new target of the same composition never yielded superconducting films.

Finally, a  $\text{Ba}_{0.6}\text{K}_{0.6}\text{BiO}_x$  target was used to grow superconducting films in an off-axis configuration at pressures of 100 mTorr  $\text{O}_2$  and 200 mTorr Ar and at a deposition temperature of  $\sim 400^\circ\text{C}$ . Attempts to fabricate superconducting films at lower pressures (and thus higher sputtering rates) failed.

$\text{SrTiO}_3$  buffer layers for BKBO films were sputter-deposited at  $750^\circ\text{C}$ . Such a high growth temperature results in high-quality films.

YBCO films were grown in an off-axis configuration on  $\text{LaAlO}_3$  and  $\text{NdGaO}_3$  substrates. The sputtering gas mixture consisted of 40 mTorr  $\text{O}_2$ , 100 mTorr Ar, and 7 mTorr  $\text{H}_2\text{O}$ . Water vapor has been found to increase the  $T_c$  of the resulting films [169]. The substrate temperature was  $\sim 700^\circ\text{C}$  throughout the deposition and the power to the gun was 80 Watts. The same conditions were used for growing Ca- and Co-doped YBCO films.

After every deposition, the heater power was turned down so that the films cooled to  $\sim 400^\circ\text{C}$  in 20 Torr of  $\text{O}_2$ . The heater was then turned off and the films cooled slowly to room temperature in oxygen. This was done to allow oxygen sufficient time to enter the films; it has been found that the exchange of oxygen in YBCO is quite rapid above  $500^\circ\text{C}$  but slows considerably below this temperature, where it is believed that gas-phase diffusion becomes rate-controlling [170]. The importance of oxygen content to superconductivity and its effect on  $T_c$  can be seen in Figure 38.

### C. Junction fabrication

The first junction fabricated was an SIN one (superconductor-insulator-normal metal) [171]. The base electrode was a 3500 Å-thick BKBO film grown on  $\text{SrTiO}_3$

(011). BKBO forms a native surface insulating layer upon exposure to the atmosphere; this layer was used as the junction barrier. Silver paint was used as the metal counter electrode.

All thin-film multilayer structures were then grown for junction measurements. They consisted of a BKBO base electrode of 1500 Å, a 30-60 Å-thick barrier of evaporated MgO or sputtered SrTiO<sub>3</sub>, and a 200 Å BKBO counter electrode capped with 500 Å of gold to ensure good electrical contact to the superconductor. The SrTiO<sub>3</sub> layer was deposited at ~400°C, 80 W, and in 40 mTorr O<sub>2</sub> and 100 mTorr Ar. Silver paint in ~2 mm -diameter regions was applied to the gold and used as a mask in subsequent Ar ion-milling at 150 volts to isolate areas of the samples for junction measurements. A schematic view of the configuration used for tunneling measurements is shown in Figure 57. Similar multilayer structures, known as BKBO-epitaxial-tunneling-heterostructures, or BETH's, were subsequently made with thicker (nominally 200 Å) barriers of sputtered SrTiO<sub>3</sub> and 19 K-T<sub>c</sub> BKBO electrodes. These were patterned in the same manner and measured by the techniques described previously.

A BKBO grain-boundary junction was fabricated by depositing BKBO over a substrate step. The grain boundary acted as the barrier. The film was patterned and gold contacts were deposited on it. Junction properties were measured in the same fashion as for YBCO junctions.

YBCO edge junctions were deposited on NdGaO<sub>3</sub>. The YBCO base electrode, typically ~2000 Å thick, was deposited as described previously, and then a SrTiO<sub>3</sub> insulator of ~2000 Å was deposited under the same conditions used for the SrTiO<sub>3</sub> barriers in all-BKBO junctions. This structure was then Ar-ion milled at 150 V and at an angle of 60° from the normal so that a step was formed as shown in Figure 58. After ion-milling, a 5% Br-methanol solution was used for 10 seconds to clean the newly-formed edge. The barrier, a 300 Å-thick Co/YBCO layer, was

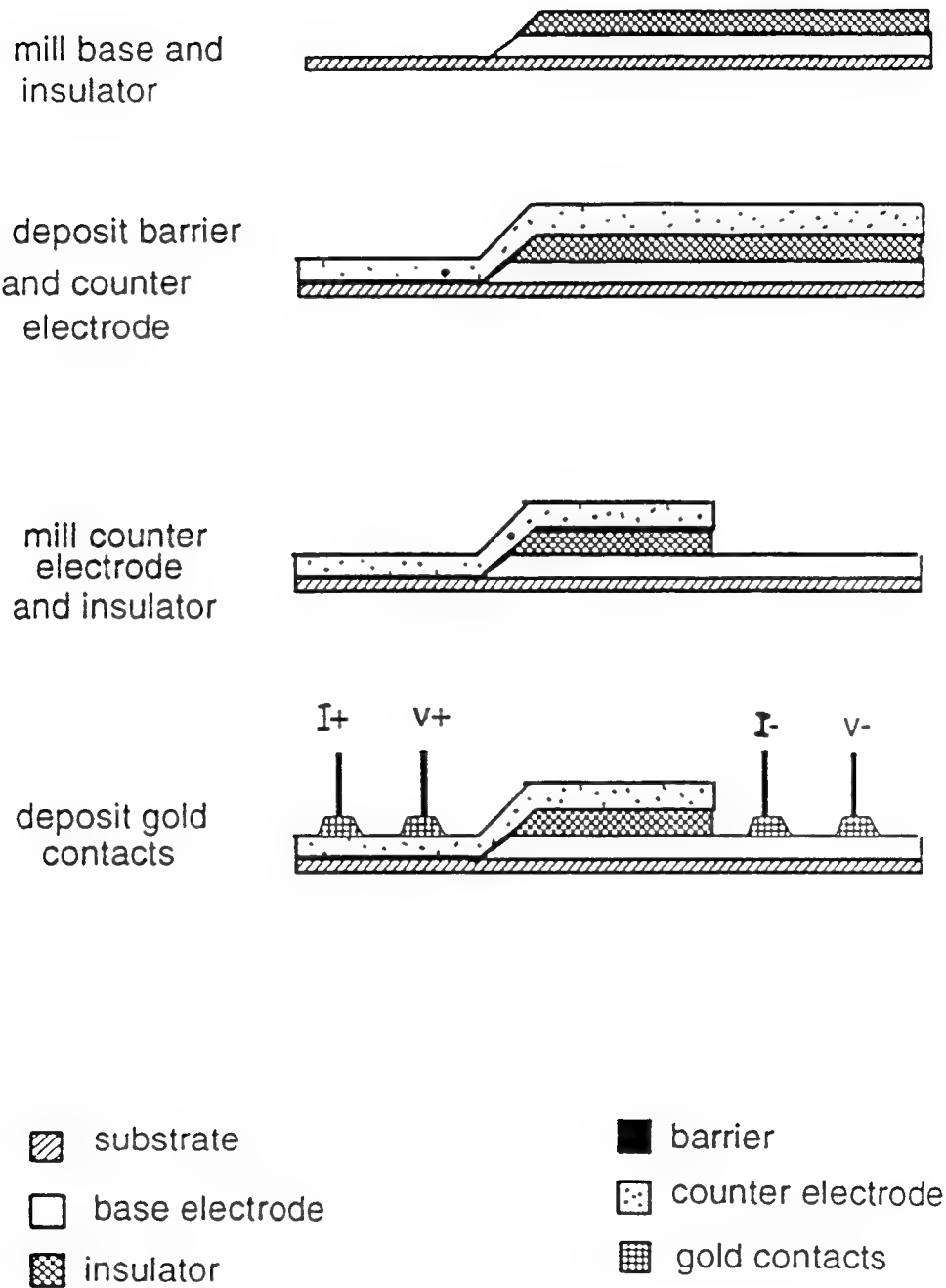


Figure 58. Procedure used in patterning edge junctions.

subsequently deposited under the same conditions as YBCO and a 2000 Å YBCO counter electrode followed. The structure was patterned and gold pads were deposited on the YBCO electrodes. The junction was then wire-bonded onto a disk containing a circular arrangement of gold pads for junction measurements. The disk was mounted into a probe, submersed in liquid nitrogen, and appropriate electrical connections were made.

## Chapter V. Results and Discussion

### A. BKBO Films

The challenge in growing these films has mostly arisen from the inconsistency of the BKBO targets. For example, one  $\text{Ba}_{0.6}\text{K}_{1.2}\text{Bi}_{1.4}\text{O}_x$  target resulted in films with  $T_c(R=0) = 15.2$  K. These were used in SIN junctions and grain-boundary junctions. This target degraded over time, however, and results were not reproducible. Another target of the same composition never allowed the production of superconducting films. Films made from this target under the same conditions used previously resulted in a great deal of microcracks or semiconducting films.

A similar trend was seen for stoichiometric targets and  $\text{Ba}_{0.6}\text{K}_{0.6}\text{BiO}_x$  targets. They degraded over time and when a new target replaced one, the optimum sputtering conditions were not the same as what they had been for the previous target. Results obtained from these unstable targets were therefore not reproducible.

These symptoms are probably a result of the difficulty in fabricating both BKBO targets and producing stoichiometric films because of the volatility of the potassium. In addition, both targets and films react with the atmosphere to form a native surface layer which was found by XPS to consist mostly of carbonates. This can be seen in Figure 59, which has a carbon peak at 969 eV; no chlorine, which was found in the surface layer of  $\text{Ba}_{1-x}\text{Rb}_x\text{BiO}_3$  films [172], was present. Figure 60 compares the superconducting transition of a film shortly after deposition to that of the same film one year later. It can be seen that the transition temperature has changed very little but that the resistivity has changed by  $\sim 50 \mu\Omega\cdot\text{cm}$ . This is indicative of a change in thickness of the superconducting material, implying that approximately the upper 250 Å has reacted and has become a non-conducting layer.

Chemical content has a profound effect on the transition temperature of BKBO films. The  $T_c$  will be highest for a potassium content of  $x = 0.375$  in  $\text{Ba}_{1-x}\text{K}_x\text{BiO}_3$

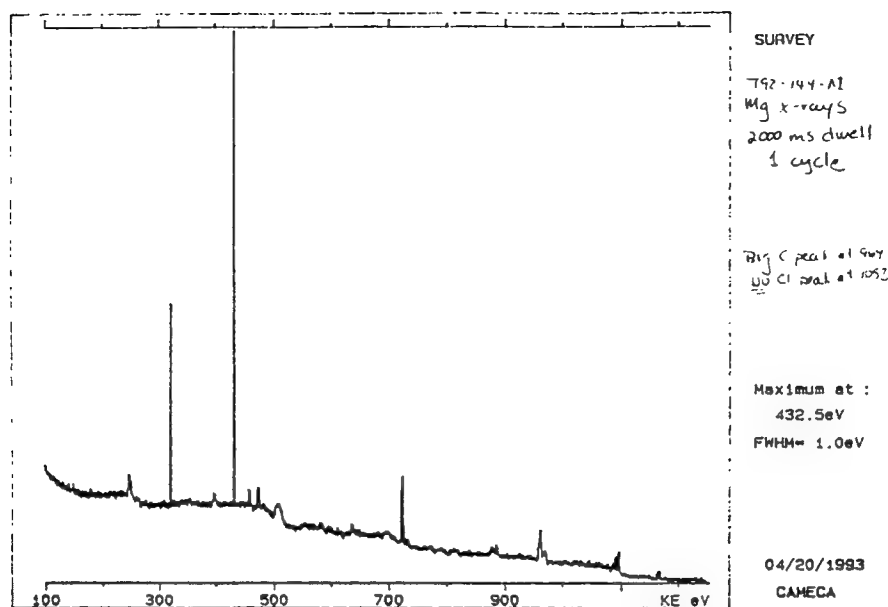


Figure 59. XPS scan of a BKBO film showing the composition of the native surface layer. Note the carbon peak at 969 eV. The other peaks are all Ba, K, Bi, or O peaks from the underlying film.

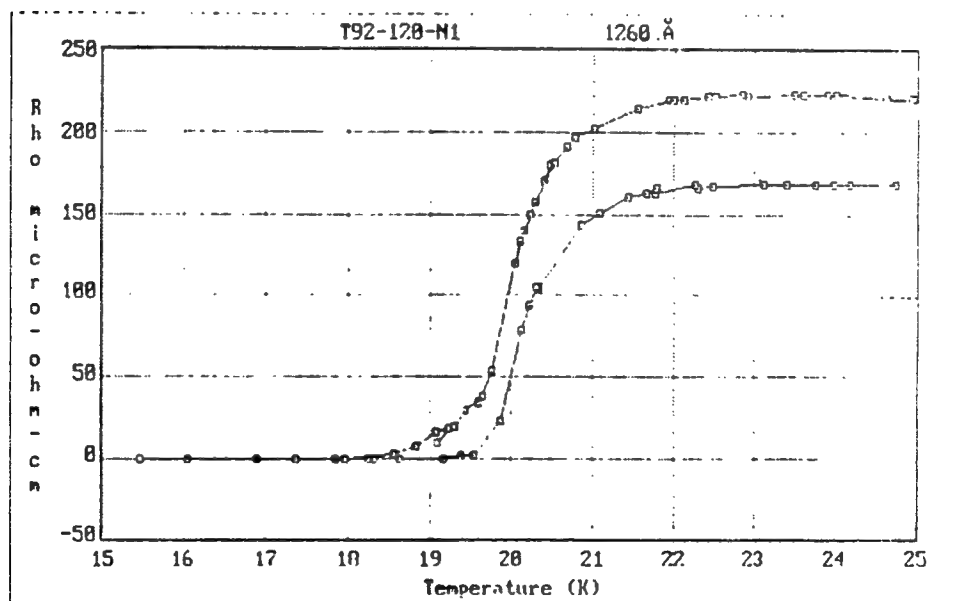


Figure 60. Comparison of the superconducting transition of a film shortly after deposition to that of the same film one year later. The transition temperature is very similar but the resistivity has changed by  $\sim 50 \mu\Omega\cdot\text{cm}$ .

and will then decrease as K content increases [65]. Energy-dispersive x-ray analysis by spectroscopy (EDXS) has been used to determine the K content. It has been useful in giving an idea of whether enough K is present for the film to possibly be superconducting (e.g., 20 atomic percent(a/o) vs. 10), but quantitative results cannot be considered accurate and should only be used in a relative sense. The inconsistency in results obtained (sometimes films known to be superconducting have as little as 13.8 a/o K, with  $K/(K + Ba) = 0.36$ , or as much as 47.7 a/o, with  $K/(K + Ba) = 0.66$ , although the range is supposed to be only from  $x = 0.375$  to 0.5 [65]), may be due to several factors. The standardless ZAF corrections used in this determination do not incorporate the effects of absorption and fluorescence in thin films, the fact that a substrate is present, and the interaction that the elements in the superconductor have. The background correction has been written for an iron alloy, not for a compound, and for a bulk material, not a thin film. The background subtracted during quantitative analysis is appropriate for the tall Bi peak but is too great for the small Ba and K peaks, thus introducing a large error and making the results unreliable. Background subtraction for a BKBO single crystal spectrum is shown in Figure 61.

Auger depth profiling showed the films to be of uniform composition without interdiffusion of the elements occurring (the sample had a BKBO film grown on a Ba-Bi-O buffer layer on a  $SrTiO_3$  substrate). These results, shown in Figure 62, agree with those of XPS, which similarly showed the layer formed on the film surface upon exposure to air to be mostly composed of carbonates.

The reason for the use of the Ba-Bi-O buffer layer is that it is felt that it would enhance epitaxial growth [173][174] and prevent any substrate-film reaction. One would actually expect the growth of potassium-deficient BKBO buffer films at high temperatures to be detrimental to epitaxy, because this will increase the pseudocubic lattice parameter from the desired 4.283 Å to 4.355 Å for a  $BaBiO_3$

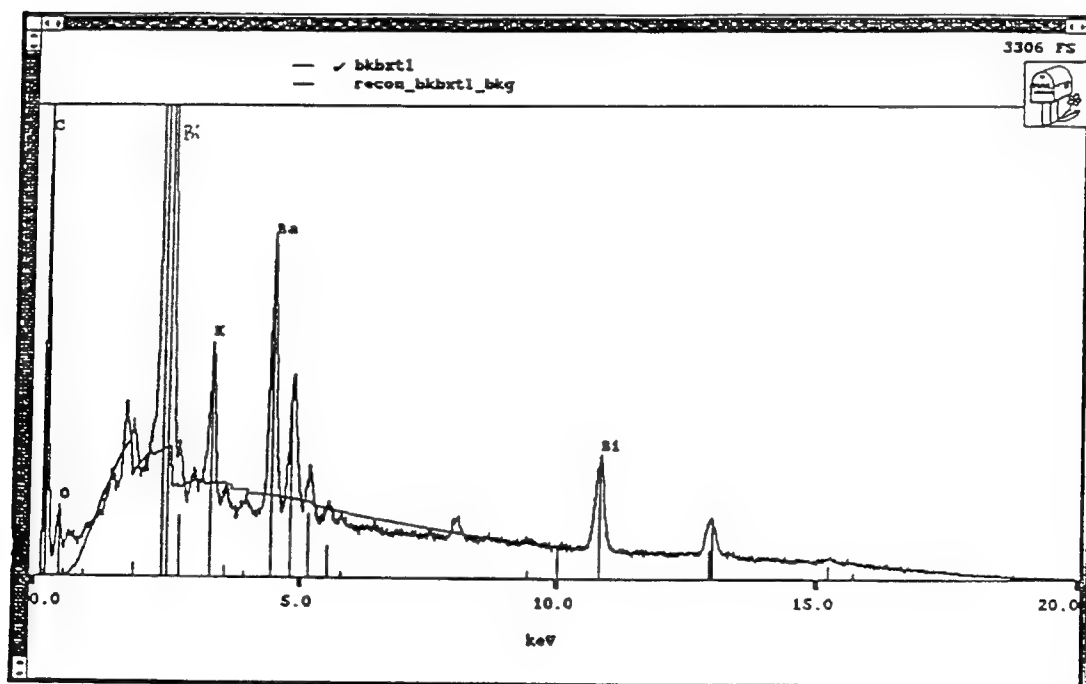


Figure 61. Background subtraction shown for a BKBO single-crystal spectrum after the standard "Fe efficiency" program was run in order to calibrate the background spectrum.



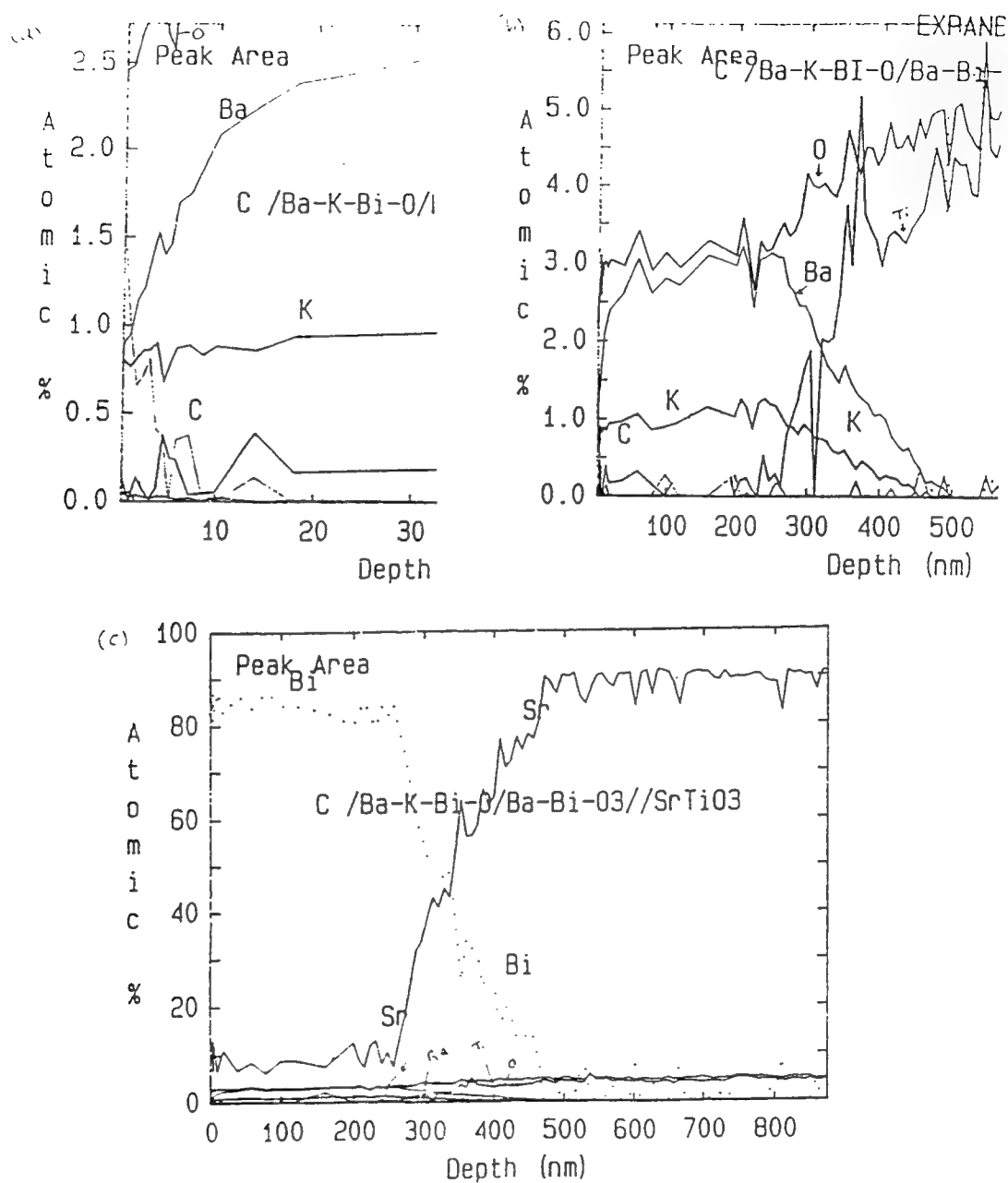


Figure 62. Auger depth profile of T91-83-S3, a 4300 Å BKBO film grown on a 190 Å BaBiO<sub>3</sub> buffer and a SrTiO<sub>3</sub> substrate. Beam used was 10 kV, 38 nA (a) expanded scale showing C and O (at top) peaks at surface (b) expanded scale for BKBO film (c) scan for entire sample

film [65]. Most of the substrates used, however, have lattice parameters smaller than that of BKBO, as listed in Table V. Our XPS and Auger results showed that a substrate-film reaction is not of concern. There was no apparent effect on orientation by using buffer layers, so we have ceased to use them.

Scanning electron microscopy showed the best-quality BKBO films to be smooth and featureless. A smooth, crystalline surface is necessary at the electrode-barrier interface in junctions. This tool was also useful in revealing microcracks in non-superconducting films, as well as some rock-like features on poor-quality films with very large  $\Delta\omega$ 's.

Similar results were seen with atomic force microscopy. Films with very low resistivities and  $\Delta\omega$ 's of  $0.6\text{--}0.7^\circ$  had small, round, pebblelike features, while films with large  $\Delta\omega$ 's had large features which looked like the rock formations found on cave walls.

Indexing RHEED and LEED patterns allows one to determine the two-dimensional symmetry of the film surface and the orientation of the film with respect to that of the substrate. An example of pattern indexing is given in Appendix III. These patterns can also yield limited information about the surface structure. For example, one set of 16.8 K films apparently had facets which were likened to greenhouse roofs or this type of pattern may be due to a vicinal surface [175][176]. This structure was indicated by the divergence of two separate reflected beams in LEED, as well as by the difference in reflections at slightly different angles in RHEED.

Typical LEED and RHEED patterns are shown in Figures 63 and 64. These techniques, especially LEED, are surface-sensitive, the figures thus show that the symmetry of the bulk of the BKBO films was evident even in the surface layer. Since RHEED patterns are representative of a surface layer  $20\text{--}50 \text{ \AA}$  thick, on the same order as the coherence length of BKBO, this indicates that the symmetry of the bulk

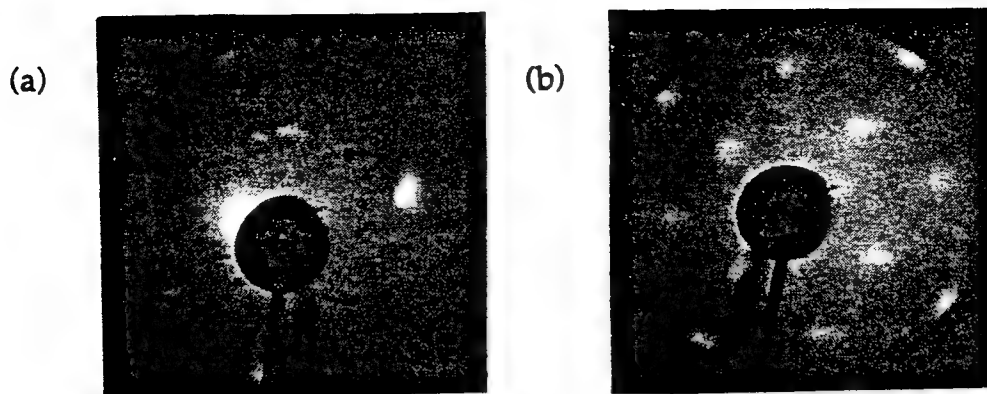


Figure 63. LEED patterns of (a) a BKBO counter electrode and (b) an MgO barrier.

The electron energies were 20.3 and 143.0 eV, respectively [171].

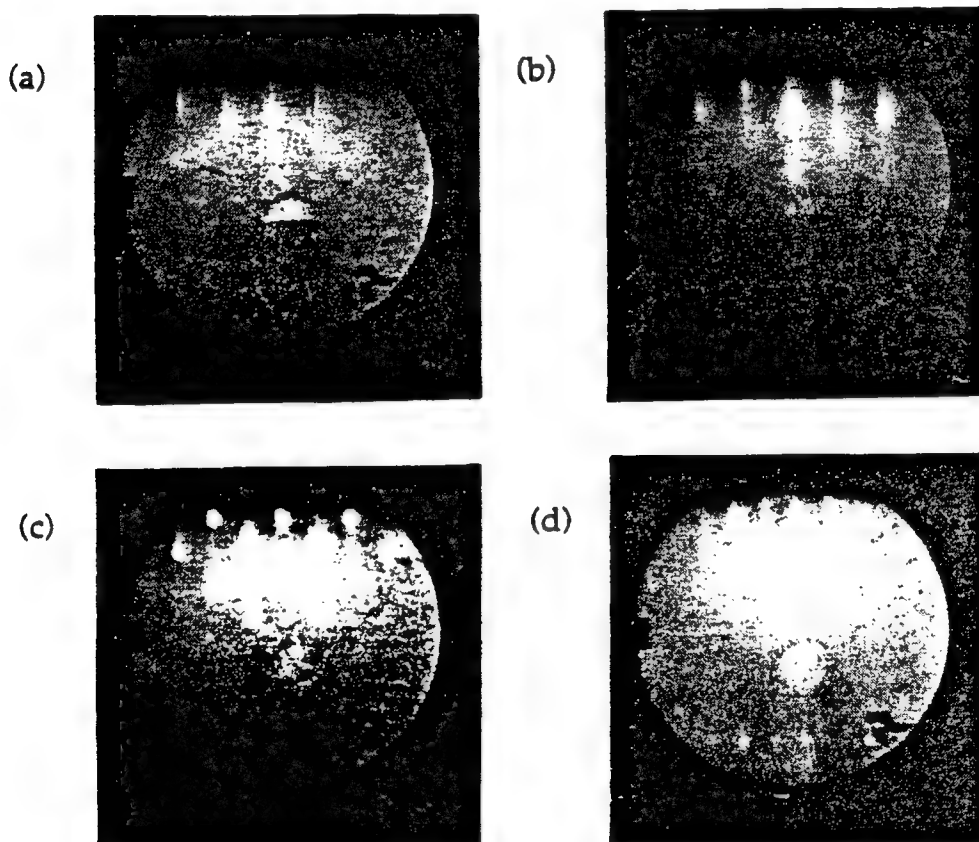


Figure 64. RHEED patterns for (a) a BKBO base electrode (b) an MgO barrier on BKBO (c) a  $\text{SrTiO}_3$  barrier on BKBO and (d) a BKBO counter electrode grown on the  $\text{SrTiO}_3$  barrier [171].

of the film was present in the surface region which determines the gap voltage and temperature dependence of the tunnel junction. This is an important consideration in junction fabrication. The (001) orientations seen in the figures prove that the films have grown epitaxially on their respective substrates. The streaked spots present in the RHEED patterns indicate smoothness of the films, whereas the Kikuchi lines (long, diagonal streaks) which are clearly visible in Figure 64(a) are typical of a well-ordered crystalline surface. The Kikuchi lines arise when electrons channel through the crystal.

Figure 65 shows a typical  $2\theta$ - $\omega$  scan for a BKBO film on  $\text{LaAlO}_3$  with the peaks identified. It can be seen that the film has grown with both (001) and (011) orientations. This scan is useful for calculating a lattice parameter from the peak positions. The fact that potassium content scales directly with lattice parameter makes XRD very significant in determining chemical content of fully oxygenated films. A lattice parameter of 4.265 Å, for example, would indicate that too much potassium is present in the films and that the next experiment should be run at a higher temperature to release some of this volatile component. This should accordingly raise the  $T_c$  of the films. These results have not shown, however, that the lattice parameter has to be exactly in the expected range to be superconducting, nor that lattice parameters in this range necessarily mean that the films WILL be superconducting. Films that have been superconducting have had lattice parameters ranging from 4.261 to 4.294 Å, while those of non-superconducting films have ranged from 4.285 to 4.330 Å. The expected range for superconducting films would be 4.270-4.289 Å [65], so one might say that the values obtained are within experimental error of the expected ones.

The  $2\theta$  scan shown in Figure 66 shows a comparison of the (022) and (003) peaks so that one can assess the relative amount of each. The repeated observation of several orientations of BKBO on  $\text{MgO}$  and  $\text{Al}_2\text{O}_3$  (as well as lower  $T_c$ 's or no

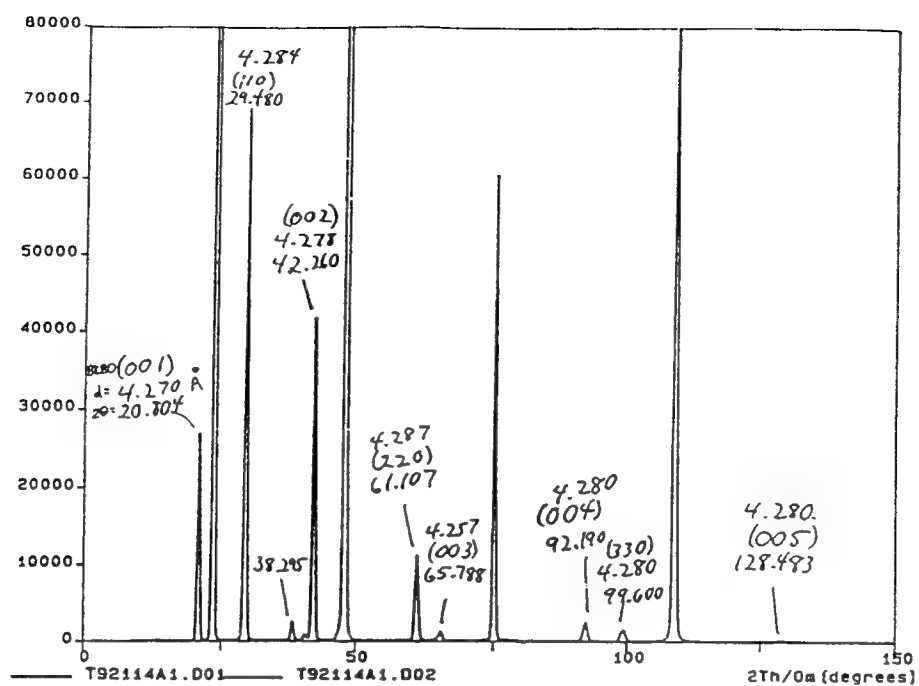


Figure 65. Typical 2θ-ω scan for a BKBO film of mixed orientation on LaAlO<sub>3</sub>.

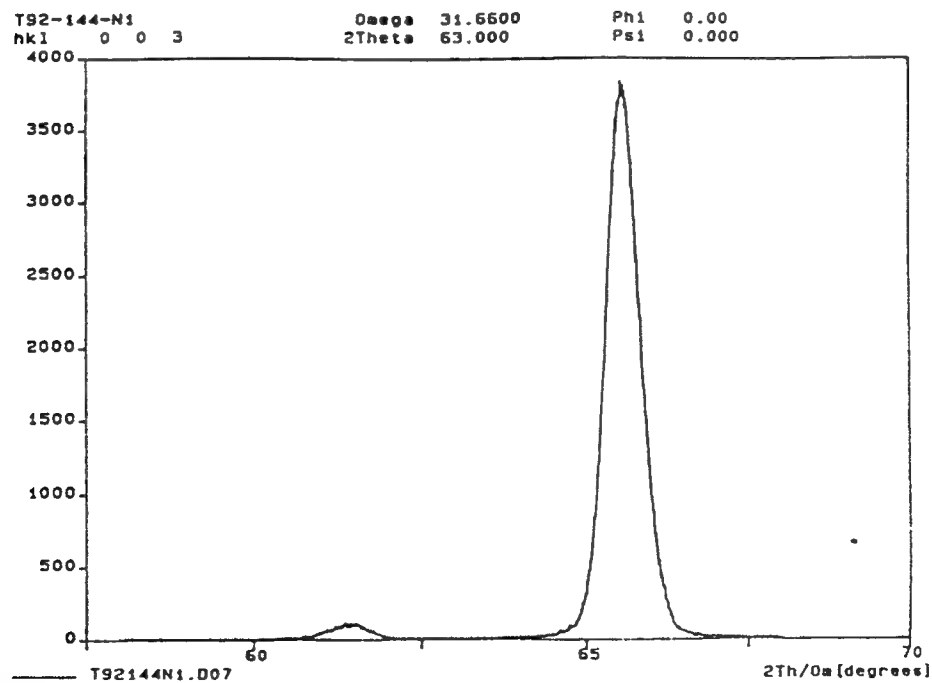


Figure 66. X-ray 2θ scan showing a comparison of the (022) and (003) peaks of a BKBO film on NdGaO<sub>3</sub>.

superconducting transition at all) led to our discontinuation of the use of these substrates. Multiple orientations, although to a lesser extent, were also observed for films grown on  $\text{LaAlO}_3$  and  $\text{NdGaO}_3$ , but films grown on  $\text{SrTiO}_3$  substrates were consistently single-orientation ones. For this reason,  $\text{SrTiO}_3$  buffer layers were used on the more technologically useful  $\text{LaAlO}_3$  and  $\text{NdGaO}_3$  substrates which can be fabricated as large wafers. This resulted in single-orientation BKBO films with a lattice parameter of  $4.280 \text{ \AA}$ , which can be seen in Figure 67. The alignment of these films was also greatly improved in both the growth direction and in the plane of the film. The improvement in the mosaic spread in the growth direction is evident in the decreased rocking curve width ( $\Delta\omega_1$ ) of the BKBO (002) peak, shown in Figure 68. Similar improvement in the plane of the film is indicated by the rocking curve width  $\Delta\omega_2$ , or full-width-half-maximum (FWHM), of the (303) peak in Figure 69. It can be seen that the use of a  $\text{SrTiO}_3$  (001) buffer layer decreased  $\Delta\omega_1$  from  $1.3^\circ$  to  $0.7^\circ$  and  $\Delta\omega_2$  from  $1.2^\circ$  to  $0.5^\circ$ .

The use of a  $\text{SrTiO}_3$  (001) buffer layer on the substrates changes the orientation so that epitaxial growth of the BKBO film on the underlying  $\text{SrTiO}_3$  buffer layer as well as on the  $\text{LaAlO}_3$  substrate is obtained. This is evident in the alignment of the {033} peaks in the  $\phi$  scan shown in Figure 70. Orientation relationships of misaligned layers can also be determined from  $\phi$  scans such as the one in Figure 71, which shows how BKBO films grow on  $\text{LaAlO}_3$  (001).

We observed that some BKBO films grow on  $\text{NdGaO}_3$  in a single orientation, whereas others have grains with both (001) and (011) growth directions. This may be due to the substrate miscut angle. Different wafers are miscut by different amounts. Some substrates are purposely miscut because it requires less energy for a thin film to nucleate on the resulting steps than on a flat surface, which would entail more surrounding broken bonds [177], as shown in Figure 72. It has been found that the growth mechanism of films is profoundly affected by the

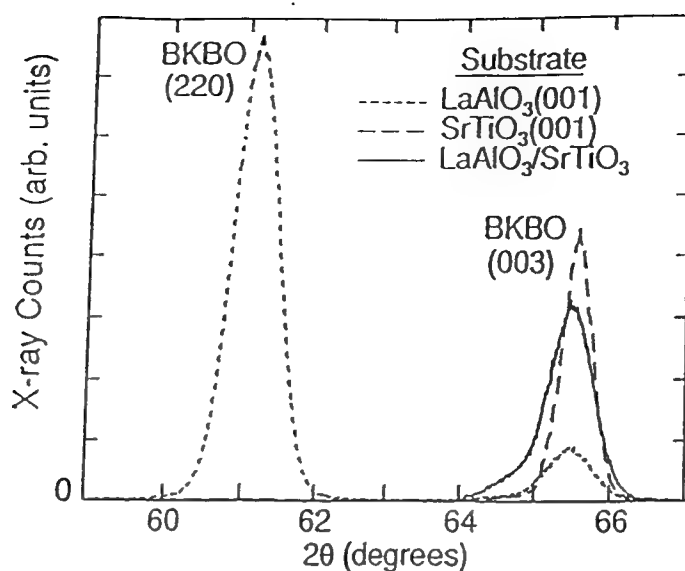


Figure 67. X-ray  $2\theta$  scan showing a comparison of (011) to (001) BKBO growth and how  $\text{SrTiO}_3$  buffer layers simulate  $\text{SrTiO}_3$  single-crystal substrates [58].

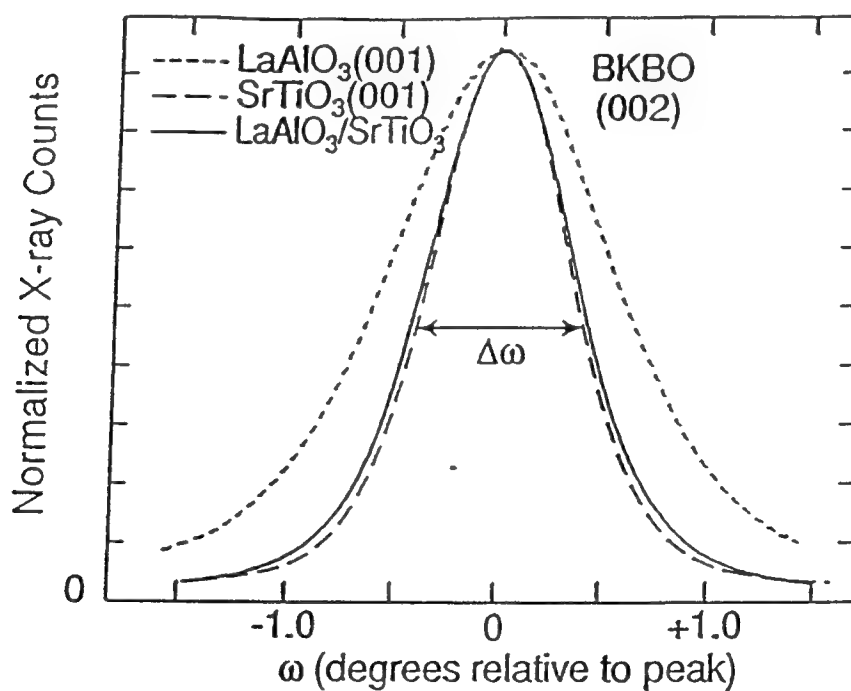


Figure 68. Mosaic spread of misaligned grains for the (001) growth direction of BKBO films. This shows the improvement gained by using  $\text{SrTiO}_3$  buffer layers and how they mimic  $\text{SrTiO}_3$  substrates [58].

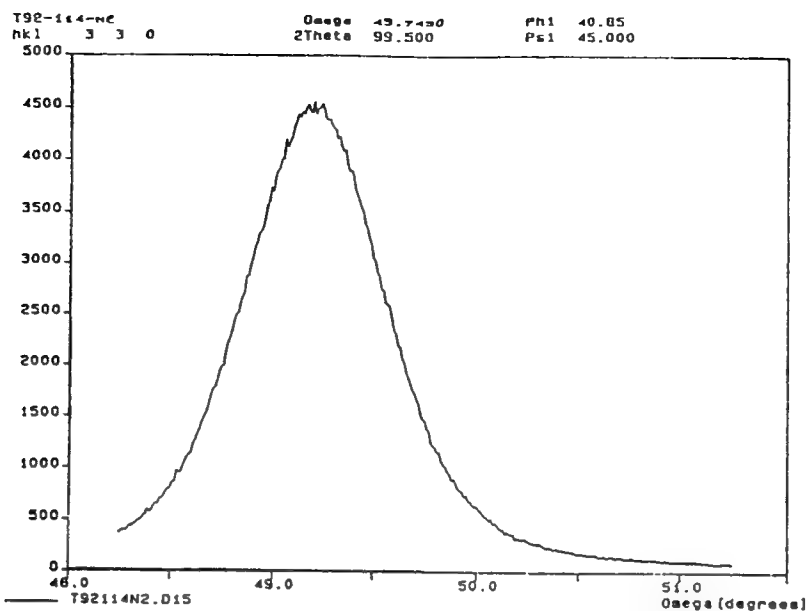


Figure 69. Rocking curve width,  $\Delta\omega_2$ , of BKBO (303) peak showing the mosaic spread in the plane of a BKBO film on NdGaO<sub>3</sub>.

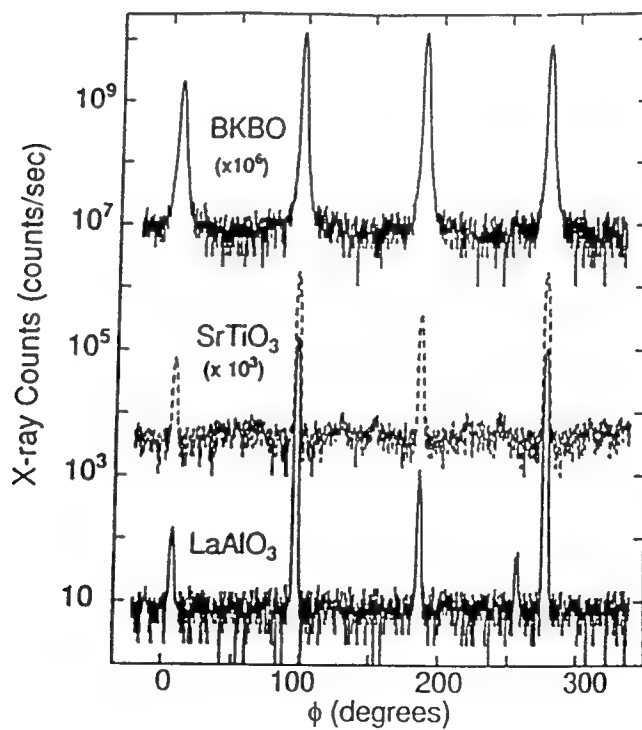


Figure 70. This  $\phi$  scan is of the BKBO, SrTiO<sub>3</sub>, and LaAlO<sub>3</sub> {033} x-ray diffraction peaks and shows the in-plane orientation of a BKBO (001) film grown on SrTiO<sub>3</sub>-buffered LaAlO<sub>3</sub> [58].



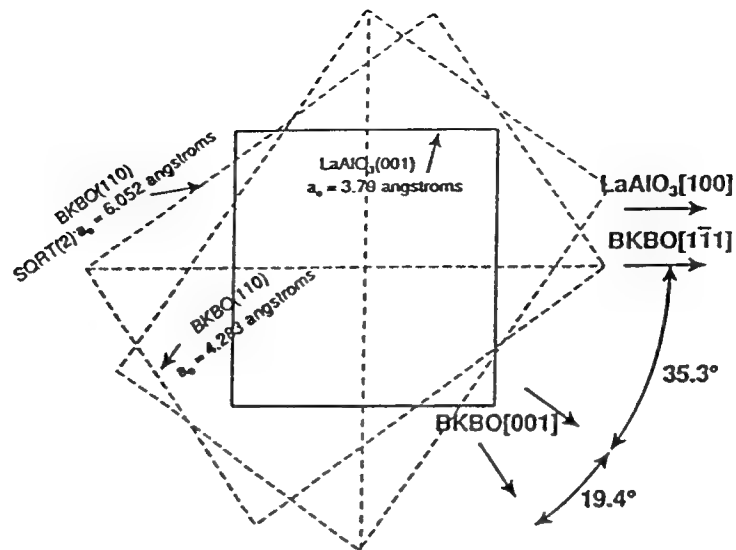


Figure 71. Orientation of BKBO (011) on  $\text{LaAlO}_3$  (001) as determined by a  $\phi$  scan.

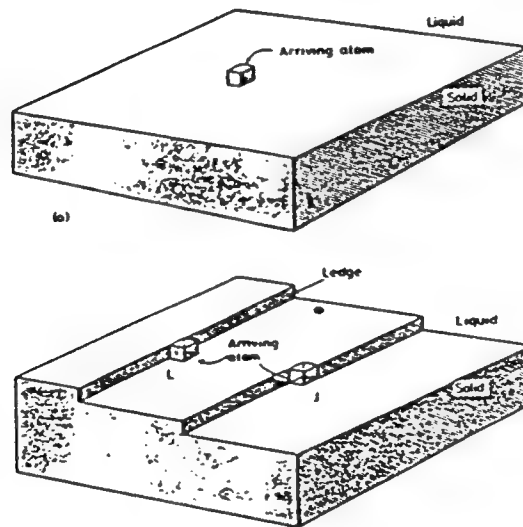


Figure 72. Schematic of nucleation occurring on a flat surface and on a step.

Addition of a single atom onto (a) a flat interface increases the number of broken bonds by four (b) a ledge increases the number of broken bonds by two (c) a jog does not change the number of broken bonds [177].

substrate miscut angle [178][179][180][181].

In addition to multiple orientations of BKBO films, there are apparently phases other than the cubic one present in some of the films. Figure 73, for example, shows some unusual peaks. The peaks are not located symmetrically about the large, center  $\{110\}$  or  $\{220\}$  peaks, indicating that they are not sidebars. Sidebars are periodic fluctuations which could be compositional variations caused, for example, by spinodal decomposition, or microstructural variations such as twins due to strain. One would expect the periodicity to be on a greater scale than the lattice constant and for it to be symmetric. In addition, the distance of the side peaks from the  $\{110\}$  is twice that from the  $\{220\}$ . It therefore appears that the peak splitting is due to the presence of an orthorhombic phase with lattice parameters somewhat different than those predicted [65] but still within the realm of possibility.

Higher  $T_C$ 's and sharper transitions correspond directly to the presence of a single-orientation film. The transitions shown in Figures 74, 75 and 76 for films grown from the first  $\text{Ba}_{0.6}\text{K}_{0.6}\text{BiO}_x$  target are proof of this. Figure 74 shows a BKBO film grown on  $\text{SrTiO}_3$ -buffered  $\text{LaAlO}_3$  with a transition ( $R=0$ ) at 26.2 K. By contrast, a BKBO film grown directly on  $\text{LaAlO}_3$  during the same deposition had a resistive  $T_C$  of 3 K lower and an inductive transition 6.5 K lower. In a similar manner, growing BKBO on  $\text{SrTiO}_3$ -buffered  $\text{NdGaO}_3$  increased the resistive  $T_C$  by 4 K and the inductive by 6 K. The 25.9 K-transition temperature in Figure 75 is that for a BKBO film grown directly on a  $\text{SrTiO}_3$  substrate during the same run. The films in Figures 74 and 75 are both single-orientation and represent the highest- $T_C$  films obtained. These films exhibited metallic behavior and had resistivities of  $\sim 320 \mu\Omega\cdot\text{cm}$  just above the transition. Another film, which had a resistive transition at 18.7 K, had a resistivity as low as  $68 \mu\Omega\cdot\text{cm}$  just above the transition. It was metallic with  $\rho(300 \text{ K})/\rho(25 \text{ K}) = 1.74$  (see Figure 76). The lowest-resistivity film to date had  $\rho = 45 \mu\Omega\cdot\text{cm}$  just above the transition and  $\rho(300 \text{ K})/\rho(25 \text{ K}) = 1.89$ . The

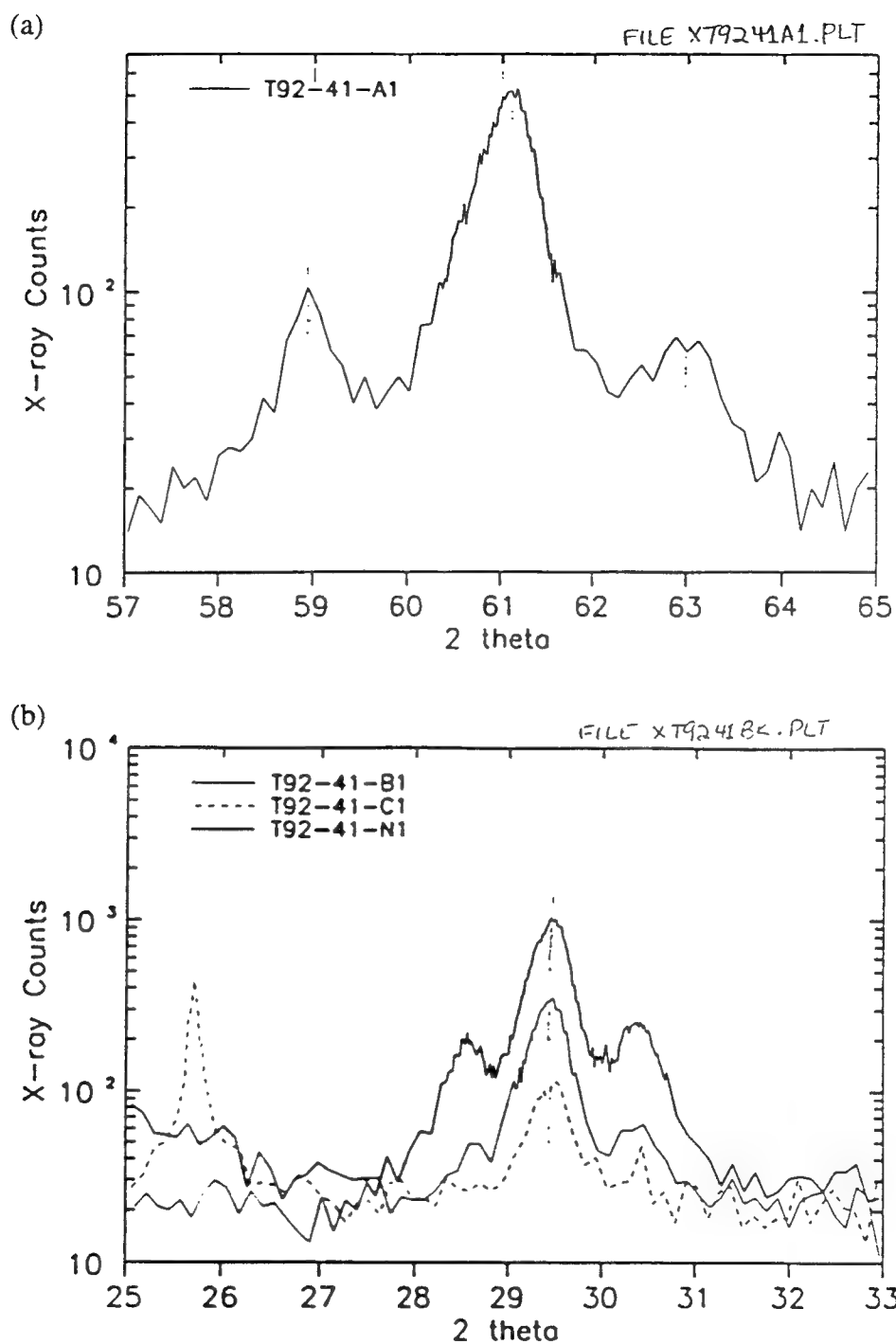


Figure 72 X-ray  $2\theta$ - $\theta$  scans showing (a)  $\{220\}$  peak splitting (b)  $\{110\}$  splitting for BKBO films which are believed to have randomly-oriented orthorhombic grains.

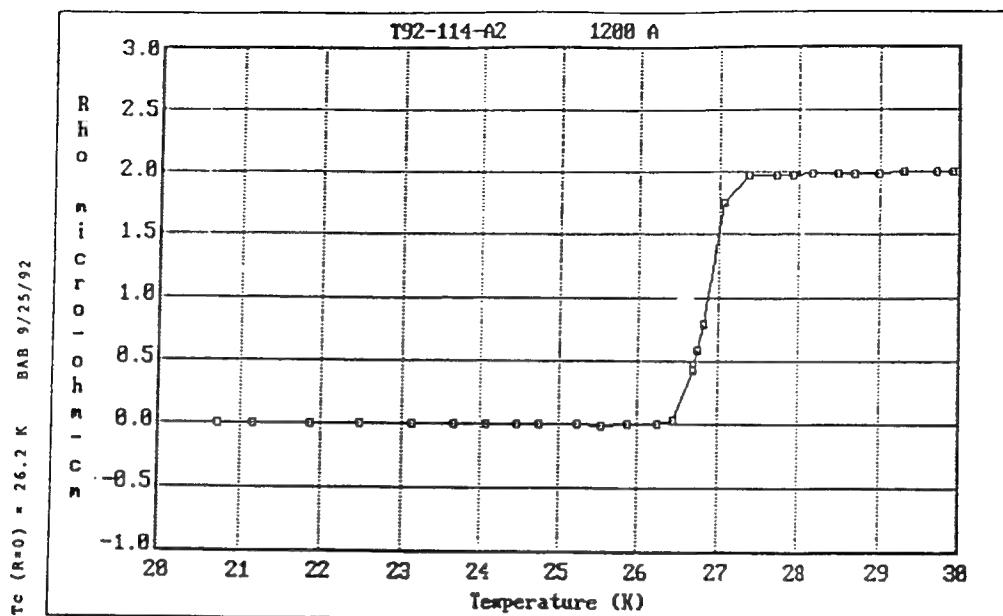


Figure 74. Transition temperature for a BKBO film on  $\text{SrTiO}_3$ -buffered  $\text{LaAlO}_3$ .

The use of the buffer raised the  $T_c$  by 3 K.

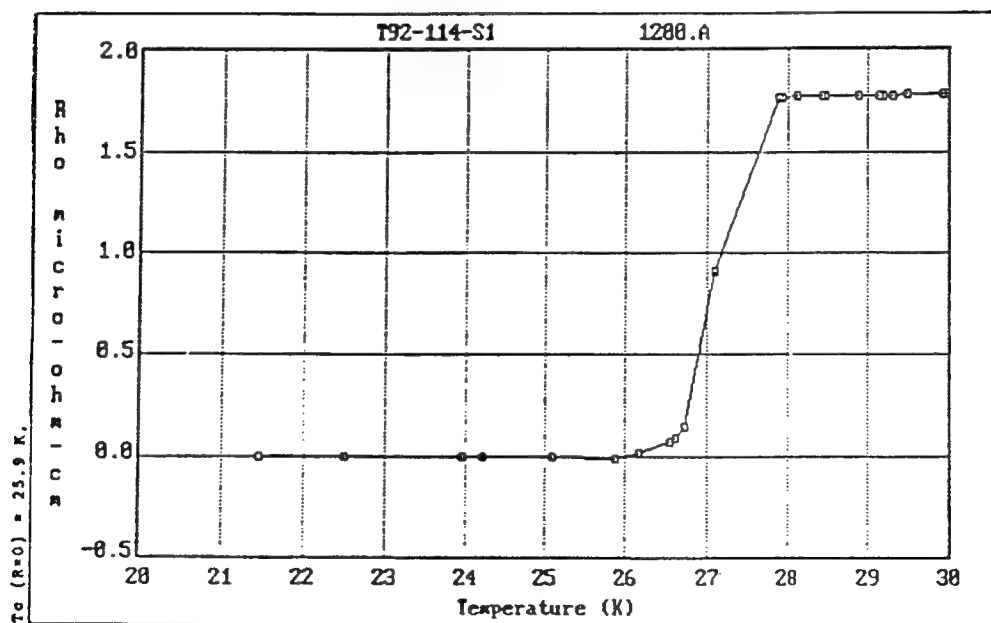


Figure 75. Transition temperature for a BKBO film grown directly on a  $\text{SrTiO}_3$  substrate. This film was deposited during the same run as that shown in Figure 74.

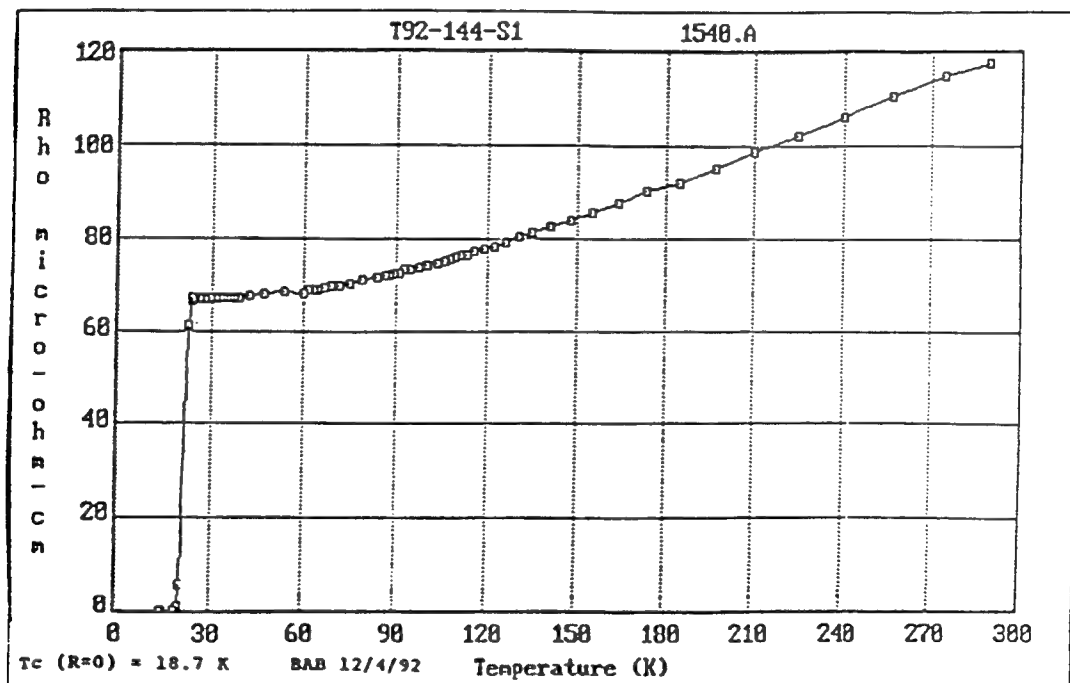


Figure 76. Resistivity vs. temperature for a BKBO film grown on  $\text{SrTiO}_3$ . This film had a particularly low resistivity of  $68 \mu\Omega\cdot\text{cm}$  just above the transition.

$T_c$  of this film was 21.9 K, and it was deposited under the same conditions as the 18.7 K film, thus refuting the assertion that a BKBO film with a higher  $T_c$  would have a higher resistivity.

Not all of the superconducting films are metallic. In some cases (such as that shown in Figure 77) there is an initial rise in resistivity and then a drop. In other cases there is a rise in resistivity with decreasing temperature until the transition is reached; this is indicative of variable-range hopping conduction. Figure 78(a) shows an example of this for 230 K to ~120 K. In such a case, the data fits an  $\exp[(T_0/T)^{1/4}]$  expression as shown in Figure 78(b). Conductivity is **not** due to thermal excitation of electrons, which is evident in the nonlinearity of the curves in Figure 78(c). Inductive transitions are always several degrees below the resistive ones. An example is shown in Figure 79.

Some of the films were patterned by photolithography and argon ion milling at 150 volts for critical current density ( $J_c$ ) measurements. This process was useful in confirming that the BKBO film was homogeneous and was not degraded by patterning, which is required for electronic devices. The results of the  $J_c$  measurements for a film grown on  $\text{LaAlO}_3$  are shown in Figure 80. This film was found to have a  $J_c$  of  $\sim 10^4 \text{ A/cm}^2$  just 2 K below the resistive transition and  $10^5 \text{ A/cm}^2$  at 4.2 K.

Contact resistance measurements were made on BKBO films using the  $T_c$  probe and placing the contacts so that I- and V- were on the same pad and I+ and V+ were on separate pads. The resistance below the superconducting transition was observed and a value of  $1.1 \times 10^{-2} \Omega \cdot \text{cm}$  was calculated. This sample was annealed in an attempt to lower this resistance by destroying any native surface layer which may have formed. Annealing increased the contact resistance, however.

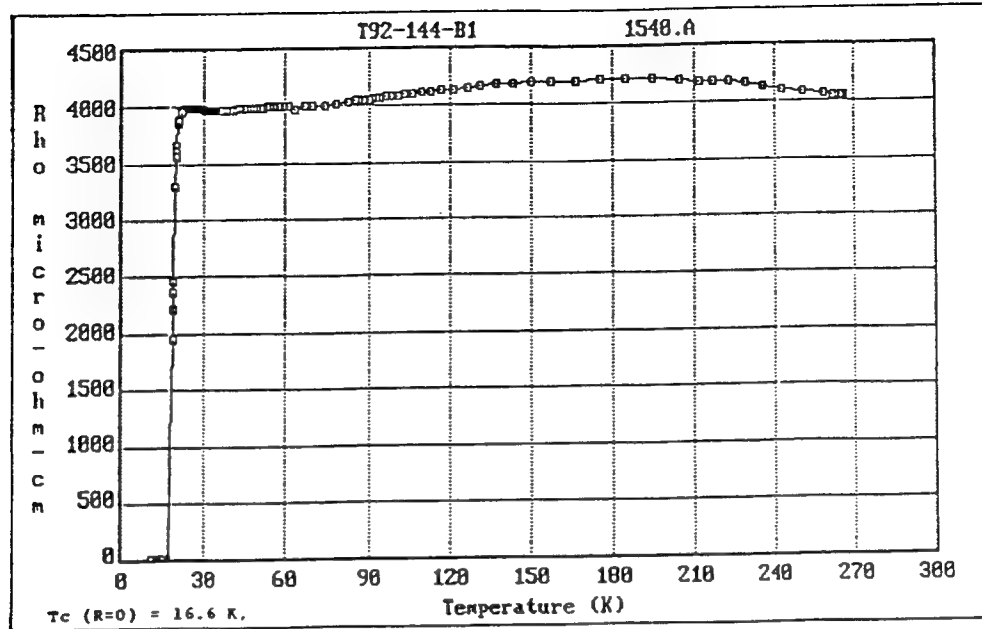


Figure 77. Resistivity vs. temperature for a BKBO film on MgO, showing an initial rise and then a drop in resistivity. This film was grown in the same run as that of Figure 76.

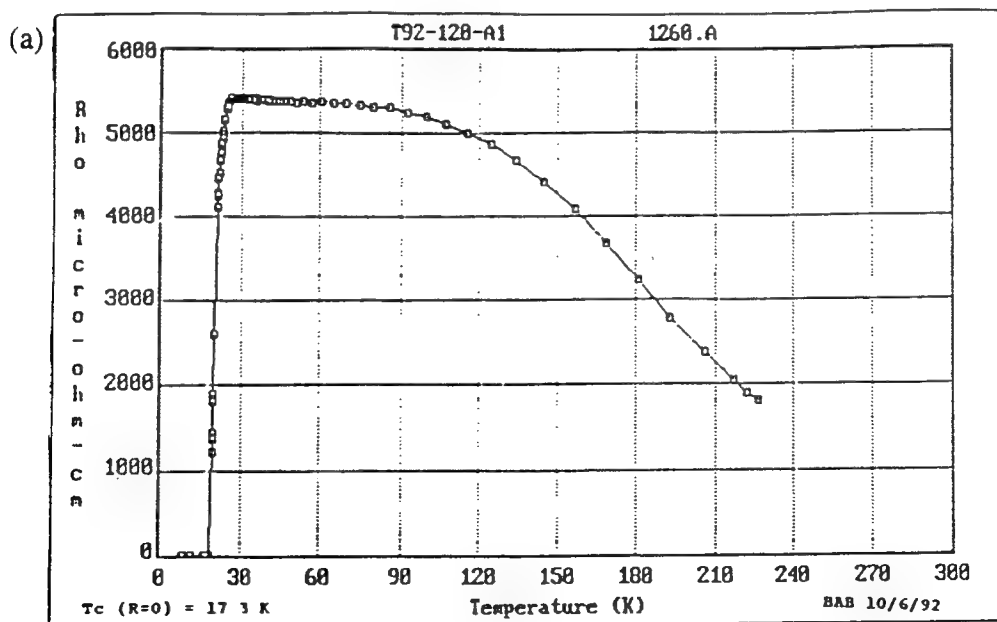


Figure 78. (a) Resistivity vs. temperature for a BKBO film grown on LaAlO<sub>3</sub>. This film exhibits variable-range hopping conduction.

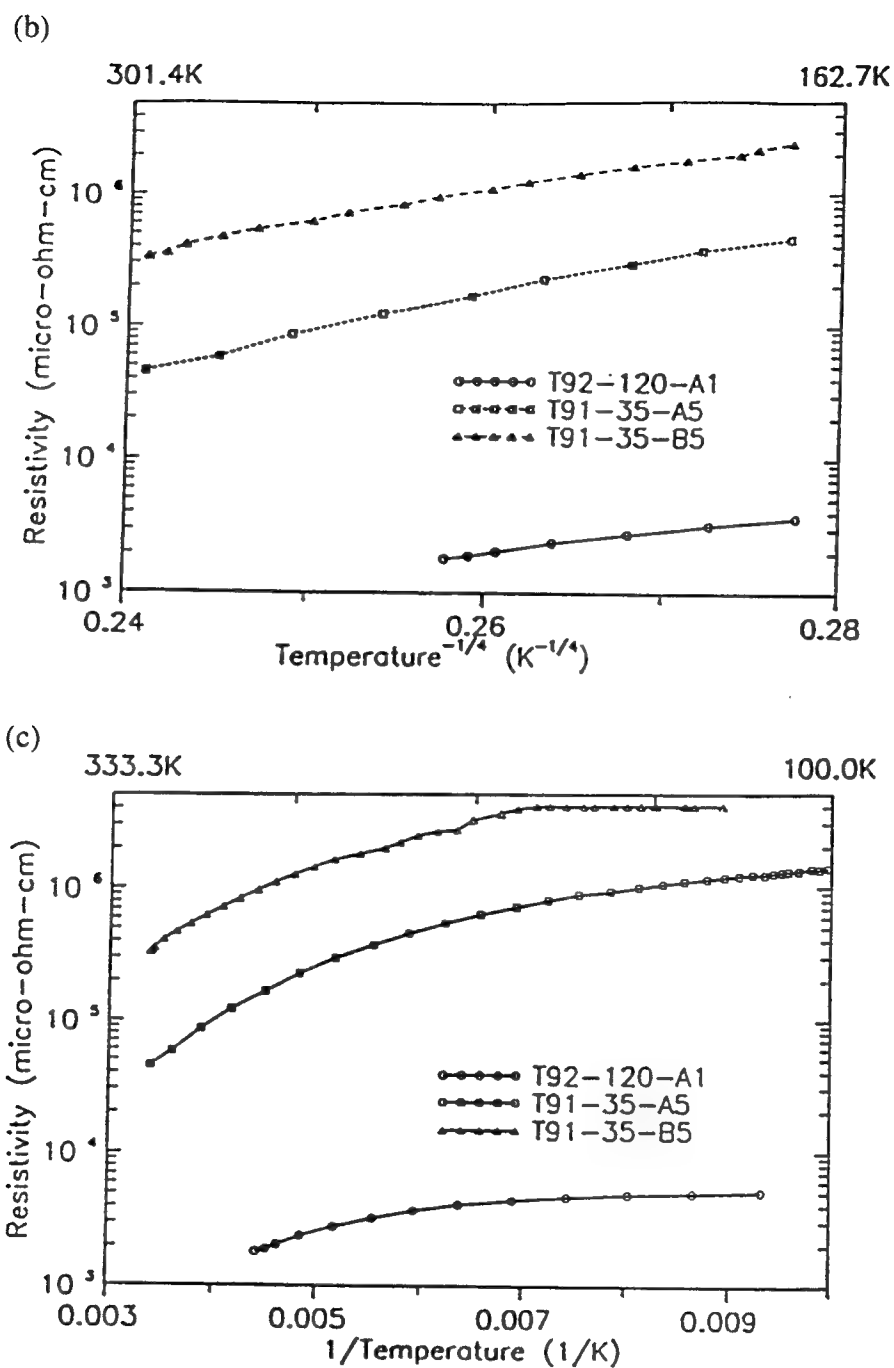


Figure 78. (b) Plot of  $\rho$  vs.  $T^{-1/4}$  for this film and two non-superconducting samples.

Variable-range hopping has such a temperature dependence. (c) Plot of  $\rho$  vs.  $1/T$ , showing that thermal excitation is **not** the mechanism responsible for conduction.



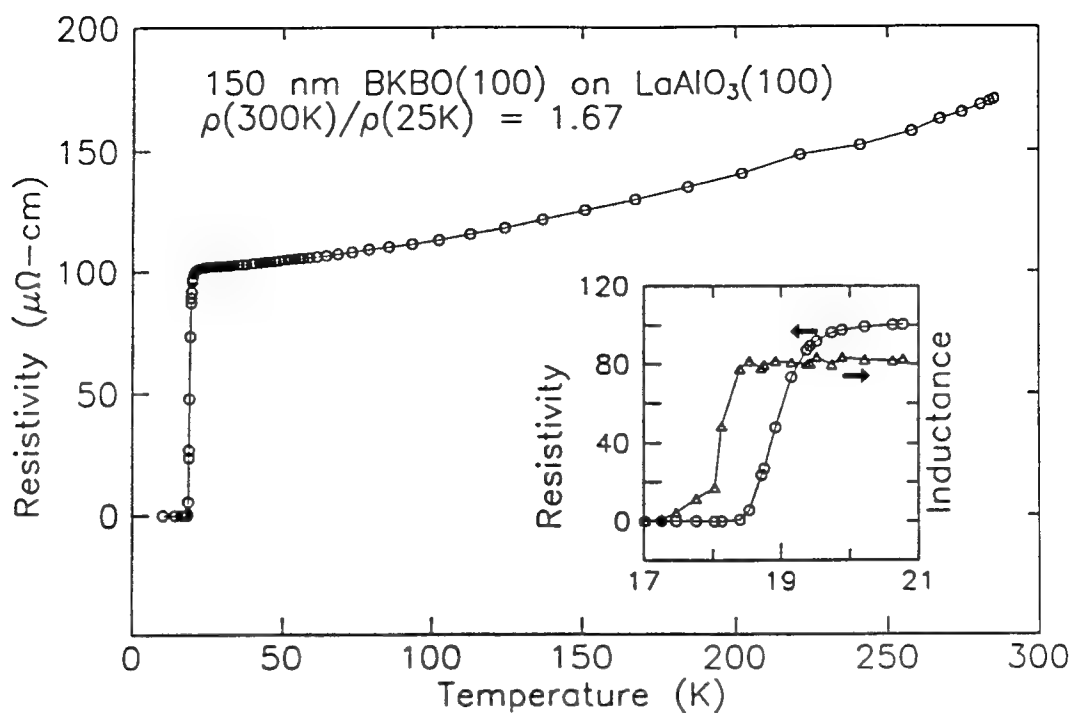


Figure 79. Superconductive transitions for a BKBO film on LaAlO<sub>3</sub>. Inset shows resistive transition at  $-18.5$  K and inductive at  $-17.2$  K.

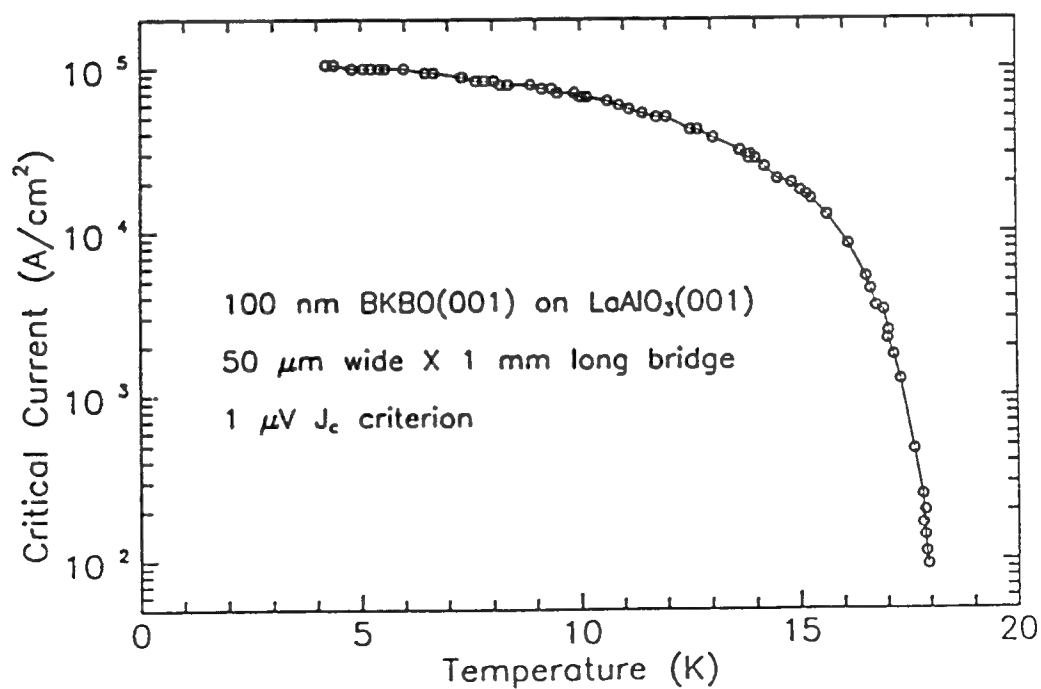


Figure 80. Critical current density measurement of a BKBO film [171].

## B. BKBO Junctions

The first junction measured was an SIN type (superconductor-insulator-normal metal) [171]. It consisted of a 3500 Å BKBO film on SrTiO<sub>3</sub> (011), with the native surface insulating layer used as the barrier, and silver paint as the metal counter electrode. This junction did exhibit tunneling behavior (see Figure 81) and a superconducting gap of ~2.5 mV at 4.2 K, which can be seen in Figure 82. A value of  $2\Delta/kT_C$  of 4.1 is obtained by this measurement, consistent with strong electron-phonon coupling.

A grain-boundary junction was fabricated by depositing a BKBO film over a step in a LaAlO<sub>3</sub> substrate. This junction had a rounded SNS-like I-V characteristic. Rounding of the curve is indicative of flux flow, which occurs when  $I_C$  is exceeded and fluxons are being dragged along by a Lorentz force. This may represent current flow through a reduced area in which  $I_C$  is easily exceeded, rather than junction behavior. This can be distinguished by determining junction response to microwaves. An SNS-type of characteristic such as this one could be from an SNS junction or from an SIS junction with a low enough capacitance that the junction is not hysteretic. The material at the grain boundaries could therefore be either normal-conducting or insulating. The junction resistance should give an indication of this. If these junctions truly are SNS ones, then this result is in disagreement with the SIS tunneling behavior seen for a BKBO grain-boundary junction grown on a SrTiO<sub>3</sub> bicrystal substrate [60].

All thin-film multilayer structures with 30-60 Å barriers did not exhibit tunneling behavior. The junctions were very low-resistance shorts, suggesting pinholes in the barrier. These may have been present because the barriers initially grew as islands, resulting in a non-uniform layer. The problem may be exacerbated by the large junction area.

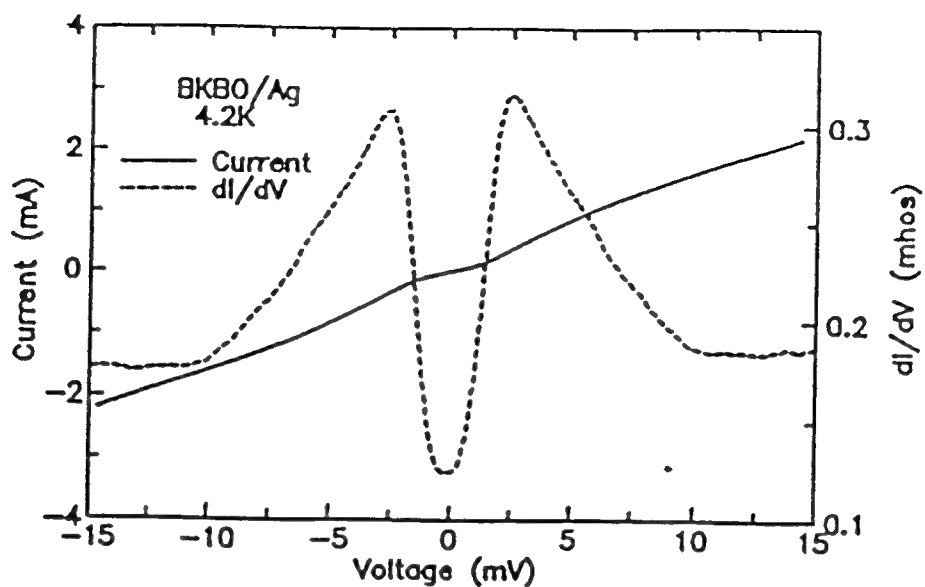


Figure 81. SIN tunneling data for a BKBO/native barrier/Ag junction at 4.2 K [171].

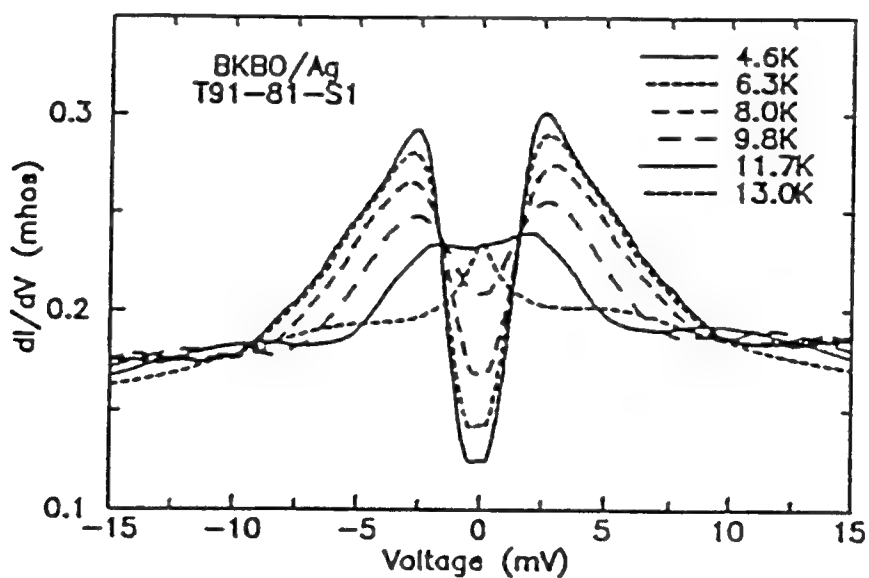


Figure 82. SIN tunneling data for a BKBO/native barrier/Ag junction at various temperatures. It can be seen that the gap has closed by 13.0 K [171].

A comparison of XPS spectra recorded before and after the barrier layers were deposited showed that the Ba, K, and Bi photoelectron intensities were greatly attenuated by the presence of an overlayer (see Figure 83), thus negating the possibility of the barrier layer remaining as islands throughout its growth.

RHEED and LEED indicated that each layer of the structure grew epitaxially. Careful observation of Figure 64 shows streaks for the base electrode in (a) and the counter electrode in (d), indicating two-dimensional growth and thus a smooth surface, whereas the MgO barrier in (b) and the SrTiO<sub>3</sub> barrier in (c) show round spots, which are indicative of three-dimensional growth. This shows that the 30-60 Å barriers grew as islands and may have had pinholes in thinner regions.

Junctions were subsequently made with thicker (nominally 200 Å) barriers of sputtered SrTiO<sub>3</sub> and 19 K-T<sub>C</sub> BKBO electrodes. The K/(K+Ba) ratio determined by EDX similarly showed the BKBO films in the junction to be potassium-rich, which is why the T<sub>C</sub> was only 19 K. Increasing the deposition temperature later led to T<sub>C</sub>'s of 25 K.

XPS scans were taken of the base electrode and of the artificial barrier layers. No evidence was found for chemical shifts that would indicate that a reaction between the barrier materials and the BKBO had occurred.

Structural evaluation of the junctions showed that each layer grew epitaxially on the one below it; this was confirmed by RHEED, LEED, and an XRD  $\phi$  scan. The BKBO base electrode of the junctions was grown directly on NdGaO<sub>3</sub>, and it had a predominantly (001) orientation, with some (011) growth present as well. The lattice parameter of the BKBO was 4.270 Å, indicating excess potassium, which is in agreement with EDXS results.

Since RHEED patterns are determined by a surface layer ~20-50 Å thick, on the same order as the coherence length of BKBO, the RHEED patterns

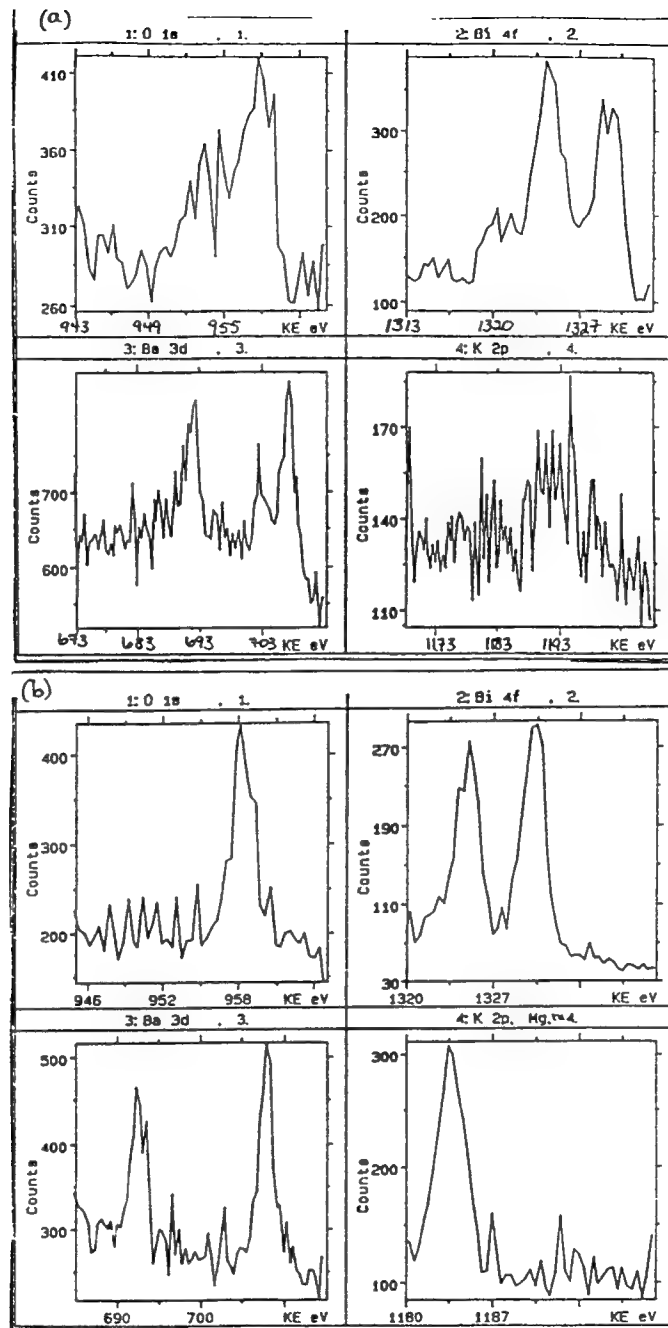


Figure 83. XPS scans of sample T92-85-B1, a BKBO film on MgO. (a) shows a scan for the BKBO film without oxygen anneal (b) is for a MgO barrier on a BKBO film. The tall peak in the fourth window of (b) is a Mg peak. Note how the Bi, Ba, and K peaks have been attenuated by the presence of the MgO overlayer. The peaks in (a) have not shifted in KE in (b), however, indicating that the two layers have not reacted.

observed showed a highly crystalline surface structure of the electrodes which determines the gap voltage and temperature dependence of a tunnel junction. The patterns shown in Figure 64, however, indicate three-dimensional, island-type or Stranski-Krastanov growth. The barrier probably grew initially as islands and was not of uniform thickness. Stranski and Krastanov showed that the second layer of a monovalent ionic crystal ( $M^+X^-$ ) condensing onto a divalent ( $M^{+2}X^{-2}$ ) substrate is less strongly bound than the first layer and even less than the surface of a bulk crystal of ( $M^+X^-$ ). Such a fluctuation of the adsorption energy of subsequent layers could well lead to island growth. This means that nucleation processes could be important during several stages of film growth and that nucleation could be either homogeneous or defect-induced [182]. Growth of a thin film can be described by [183]:

$$\sigma_s = \sigma_i + \sigma_o \cos \theta$$

in which  $\sigma_s$ ,  $\sigma_i$ , and  $\sigma_o$  are the surface energies of the substrate, the substrate-overgrowth (growing thin film) interface, and the overgrowth, respectively, and  $\theta$  is the contact angle of a deposit on the substrate. Three-dimensional islands are observed if deposit atoms are able to diffuse over the substrate and if  $\theta > 0$ . The surface energy of the overgrowth will be determined by the number of dangling bonds, so from this perspective, surface energy would be lowered if the incoming atoms join already-existing islands rather than attaching themselves to an isolated region of the substrate and nucleating a new island. The misfit strain energy and the energy of misfit dislocations should be considered as well. The number of islands per unit area depends on the deposit (film) thickness, the substrate temperature, and the deposition rate. Low substrate temperatures and high deposition rates favor a large

number of islands, since there is neither time enough nor the driving force of high temperature for surface diffusion of deposited atoms [183].

The junctions grown on NdGaO<sub>3</sub> (001) did exhibit tunneling behavior [58], as shown in Figures 84 and 85. It can be seen that the I-V characteristic in Figure 84 shows a great deal of junction leakage and high resistance when compared to an ideal one such as that for a BKBO/KNbO<sub>3</sub>/BKBO junction shown in Figure 86. The conductance curves shown in Figure 85 also have a rather odd shape when compared to those in Figure 87. This makes it difficult to assess the gap size, although it appears to be 7-10 mV if one looks only in the most temperature-dependent region of the curves. Previous measurements of the SIN junction already discussed, which contained a 15 K BKBO film on SrTiO<sub>3</sub>, had a gap of 2.5 mV, implying that a 19 K BKBO film on SrTiO<sub>3</sub> (which the top electrode in this SIS junction was) would have a gap of 3.2 mV. Since  $V_g = (\Delta_1 + \Delta_2)/e$ , this suggests that both the base and top electrodes made substantial contributions to the gap voltage.

A value of  $2\Delta/kT_c = 4.1$  was obtained for the SIN junction previously measured. Using this value, a gap of ~7 mV would be expected if the contributions to the gap voltage from both the base and counter electrodes were consistent with their  $T_c$ 's. The agreement between the expected gap value and that determined from Figure 85 is an indication that the initially-deposited BKBO layer in the top electrode, approximately a coherence length thick, was of high quality.

The effective thickness and height of the SrTiO<sub>3</sub> barrier in this junction were calculated using the Simmons model for a rectangular barrier [184], which is described in Appendix II. The width was between 60 and 46 Å and the height was between 220 and 360 mV at 4.2 and 14.2 K, respectively, although if only data at high voltages were considered, much less variation would be seen. The junctions had an extremely high resistance of 70 kΩ, which is far too great a value for practical

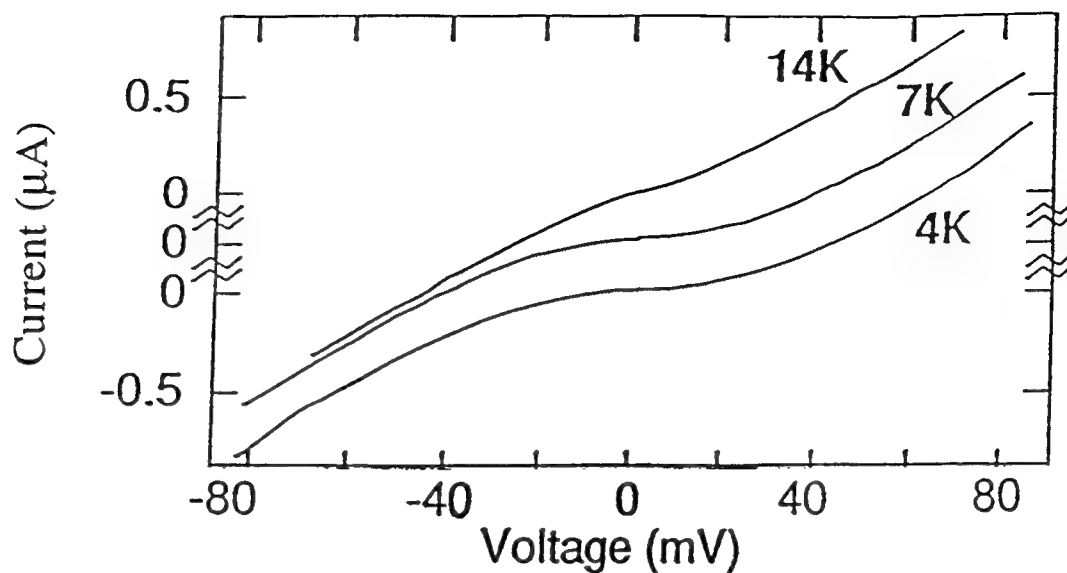


Figure 84. I-V characteristics for an epitaxial BKBO/SrTiO<sub>3</sub>/BKBO trilayer junction at various temperatures below  $T_c$  [58].

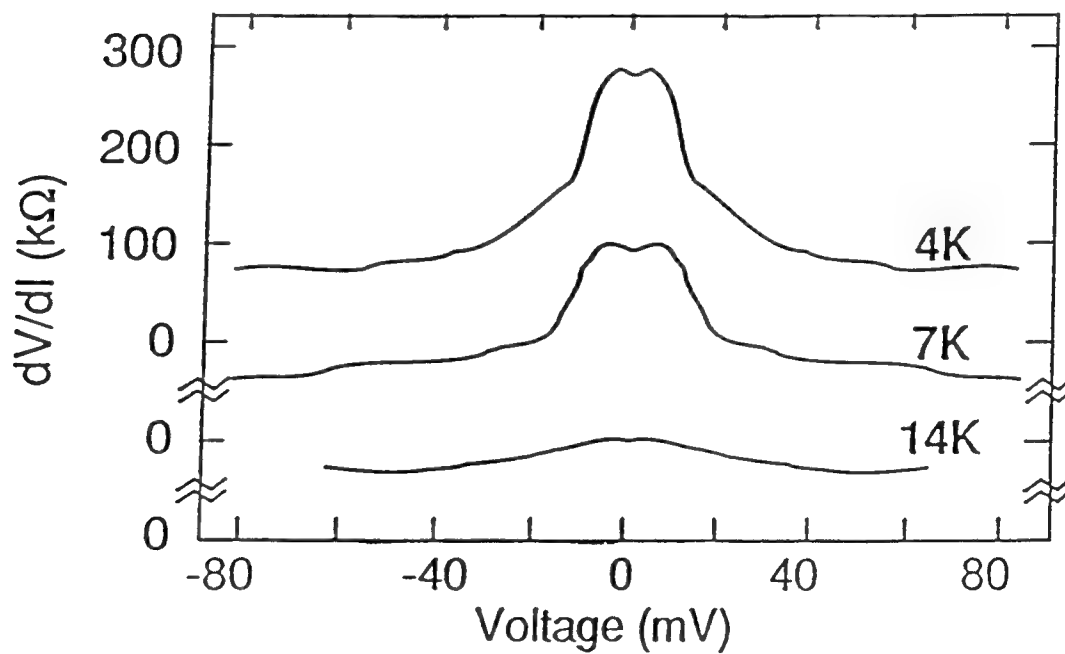


Figure 85. Tunneling data for an epitaxial BKBO/SrTiO<sub>3</sub>/BKBO trilayer junction at various temperatures below  $T_c$  [58].



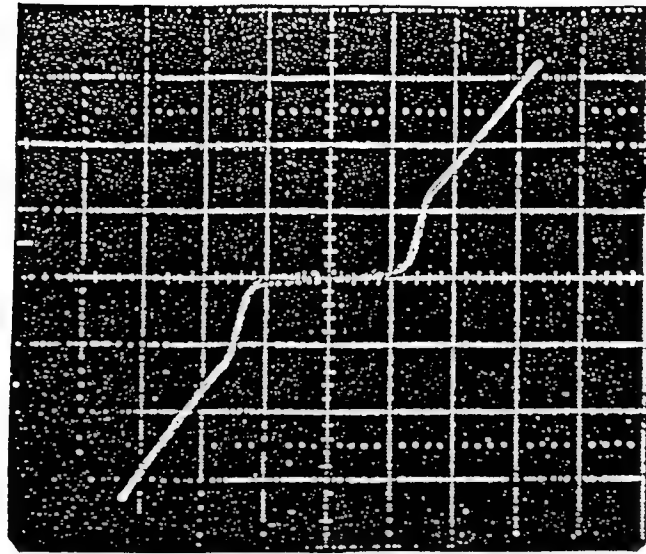


Figure 86. I-V characteristic of an all-BKBO SIS tunnel junction at 4.2 K. Nominal area of the device is  $10 \times 10 \mu\text{m}$ . Scales are vertical current =  $1 \mu\text{A}/\text{div.}$ , horizontal voltage =  $5 \text{ mV}/\text{div.}$   $T_c$  ( $R=0$ ) of the BKBO is 23 K [57].

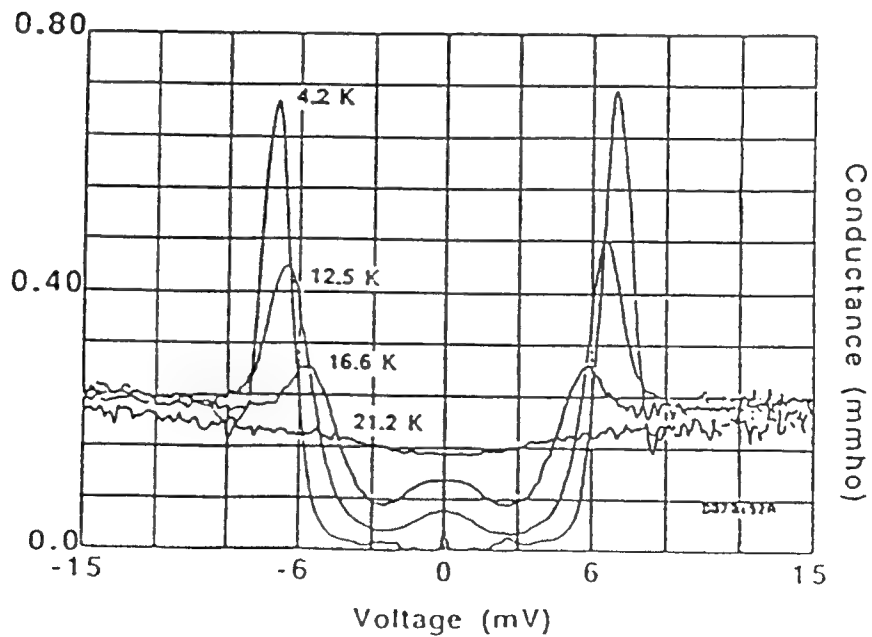


Figure 87. Conductance vs. bias voltage taken at four different temperatures below  $T_c$  on an all-BKBO junction [57].

use. The calculated resistivity of the  $\text{SrTiO}_3$  was  $7 \times 10^8 \Omega\text{-cm}$ , which one might expect for bulk  $\text{SrTiO}_3$ . The shape of the I-V curve is indicative of flux-flow behavior, which is seen for short junctions with an applied magnetic field or in long junctions due to self-field effects. These BKBO junctions were of rather large area which was ill-defined and could well be considered long junctions. The critical current through long junctions is non-uniform, as shown in Figure 14(d), and can be cancelled by oppositely-flowing currents in other regions of the junction. This may be why no critical current was observed in these junctions and only a quasiparticle curve was seen.

The resistance seen below the gap voltage shows the presence of leakage currents. These may be due to extra states in the gap (from impurities, for example) causing a tunneling current or to a conductive path such as a pinhole in parallel with the junction. There is increasing conductivity at higher voltages, which may be due to the relatively low barrier height calculated (a typical barrier height for NbN is 1-1.5 V). The Simmons model says that low barrier height will result in nonlinearity at high voltage.

The nominal deposited barrier thickness was 200 Å, in disagreement with the calculated thickness of 60 Å. This implies either that the barrier grew nonuniformly, with tunneling occurring through the thinner parts or that defects present in the barrier led to resonant tunneling, which is electron-tunneling partway across the barrier to a defect and then continued tunneling. Resonant tunneling has a lower probability because it involves several sequential tunneling events and is therefore undesirable because it leads to a lower current through the junction. Results from RHEED evaluation indicate that the former is the case; tunneling occurred through thinner parts of the nonuniform barrier.

### C. YBCO Films

Scanning electron microscopy shows the 1800-Å thick films made in the new chamber to have very few boulders and no *a*-axis grains. They did, however, have undesirable pits which may be due to copper re-sputtering. Very thick (>14,000-Å) films had very prominent *a*-axis growth.

Films had a  $T_c$  ( $R=0$ ) of 90 K, as shown in Figure 88. Metallic behavior was seen (see Figure 89) with a resistivity ratio  $\rho(300\text{ K})/\rho(91\text{ K})$  of  $\sim 2.8$ . YBCO displays variable-range hopping conduction only if doped with certain elements such as Pr [155] or if depleted of oxygen [136].

### D. Barrier Films

Ca-doped YBCO films grown with water vapor appeared to be smooth, shiny, and featureless under an optical microscope and were boulder- and *a*-axis-free when observed under an SEM, but they had unacceptably deep pits nonetheless. Films grown without water vapor had small, round features but no pits, boulders, or *a*-axis grains.

X-ray diffraction confirmed that there were no *a*-axis grains; this is shown by the  $2\theta$ - $\omega$  area scan in Figure 90 and the  $\psi$  scan in Figure 91. In the former, there would be a {309} peak at  $2\theta = 115.5^\circ$ ,  $\omega = 12.19^\circ$ , were *a*-axis growth present and in the latter, there would be a peak at  $54^\circ$ . The presence of (039) and (309) peaks in the first shows this material to be orthorhombic. The lattice parameters were calculated to be  $a = 3.821\text{--}3.829\text{ \AA}$ ,  $b = 3.887\text{ \AA}$ , and  $c = 11.733\text{ \AA}$ .

The transition temperature for this material is expected to be  $\sim 60\text{ K}$  [185], which would make it an ideal barrier for a YBCO SNS junction. The resistive and inductive transitions, however, occurred at 79.5 K and 76.9 K, respectively. These

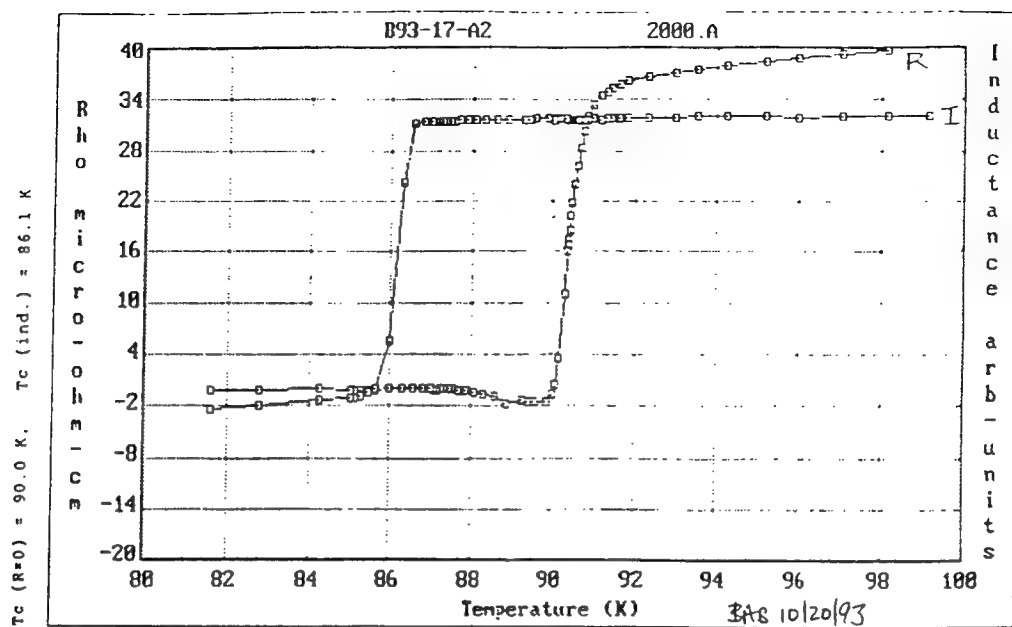


Figure 88. Resistive (90 K) and inductive (86.1 K) transitions for a YBCO film on  $\text{LaAlO}_3$ .

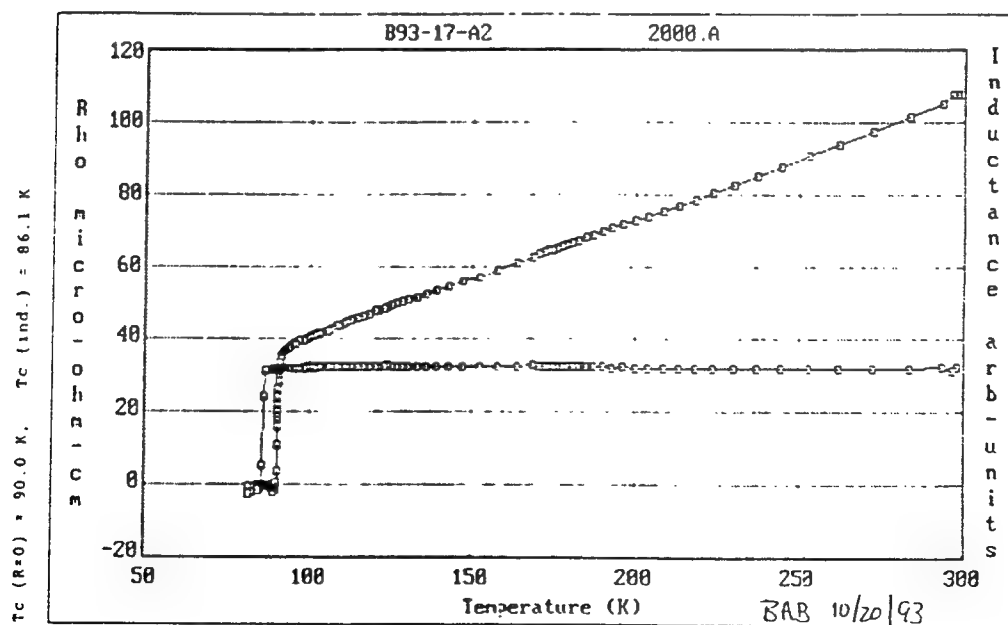


Figure 89. The  $\rho$  vs.  $T$  and  $I$  vs.  $T$  curves for a YBCO film on  $\text{LaAlO}_3$ . The ratio  $\rho(300 \text{ K})/\rho(100 \text{ K})$  is 2.75.

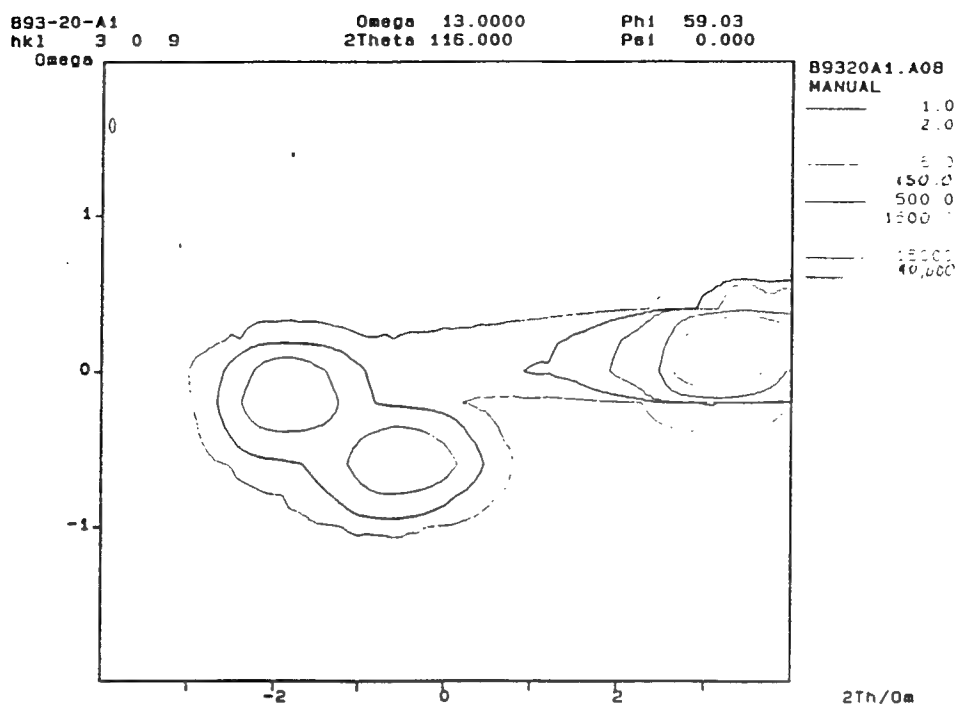


Figure 90. Area  $2\theta/\omega$  scan for a Ca/YBCO film. The peaks, from the left, are the YBCO (039), (309), and  $\text{LaAlO}_3$  (303), respectively. Were  $a$ -axis grains present, there would be another (309) peak at the same  $2\theta$  value as the other but a positive  $\omega$  value.

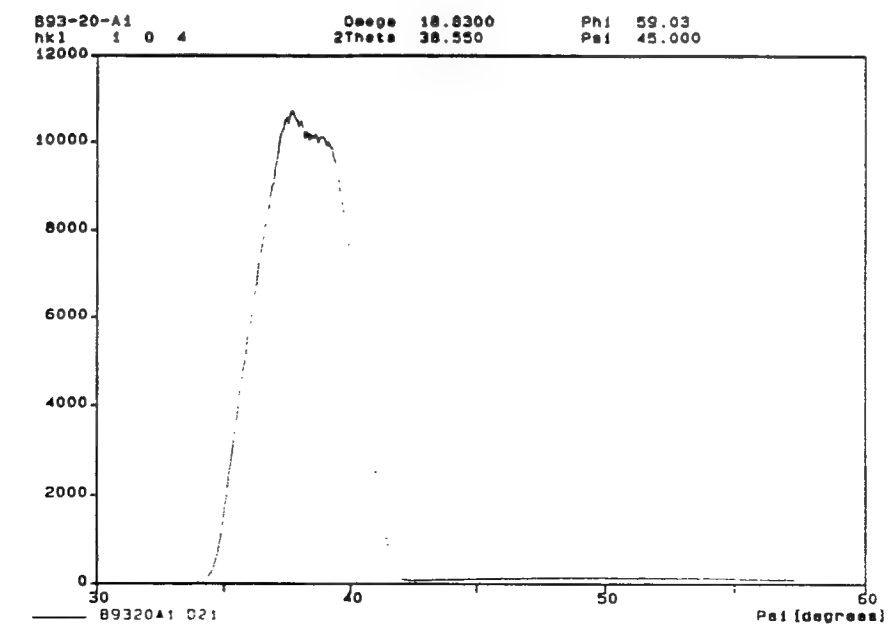


Figure 91. A  $\psi$  scan for Ca/YBCO. The peak at  $37^\circ$  represents  $c$ -axis growth. There is no peak at  $54^\circ$ , indicating no  $a$ -axis-oriented material.

temperatures are much too close to that of stoichiometric YBCO to be useful. The room-temperature resistivity was  $\sim 200 \mu\Omega\cdot\text{cm}$ . This target apparently changed in composition with increased usage or was not uniform because films later deposited from this target had  $T_C$ 's of 51 K.

Co-doped YBCO films grown on  $\text{LaAlO}_3$  had the same morphology as other films; they were boulder-free and  $a$ -axis-free but had undesirable pits in them. Very thick films ( $12,500 \text{ \AA}$ ) were grown so that EDXS analysis could be done without interference from substrate peaks. These films amazingly had no  $a$ -axis grains and no boulders. The grains were shaped like animal crackers. It was apparent from EDXS analysis on the target and the films that the target composition was reproduced in the films. It also showed the Co/Cu ratio to be higher than expected.

X-ray diffraction confirmed that no  $a$ -axis-oriented grains were present and also showed that the  $c$ -axis grains present were tetragonal, as predicted for  $x = 0.1\text{-}1.0$  [156]. Calculated lattice parameters were  $a = 3.867 \text{ \AA}$  and  $c = 11.672 \text{ \AA}$ . There were extraneous peaks which point to the possibility of the presence of a second phase.

These films had very broad transitions, with  $T_C$  (onset) = 35 K and  $T_C$  ( $R=0$ ) = 10 K. There was an expected [186] but rather odd rise in resistivity just above the transition as shown in Figure 92.

#### E. YBCO Edge Junctions

Most of the YBCO edge junctions with Co-doped YBCO barriers showed flux-flow behavior with rounded I-V characteristics. One junction, however, had a sharp, SNS-like I-V curve, which is shown in Figure 93. The same junction was then observed with 9.9 GHz radiation applied and then displayed the I-V characteristic depicted in Figure 94. Shapiro steps are clearly visible, proving that this junction is

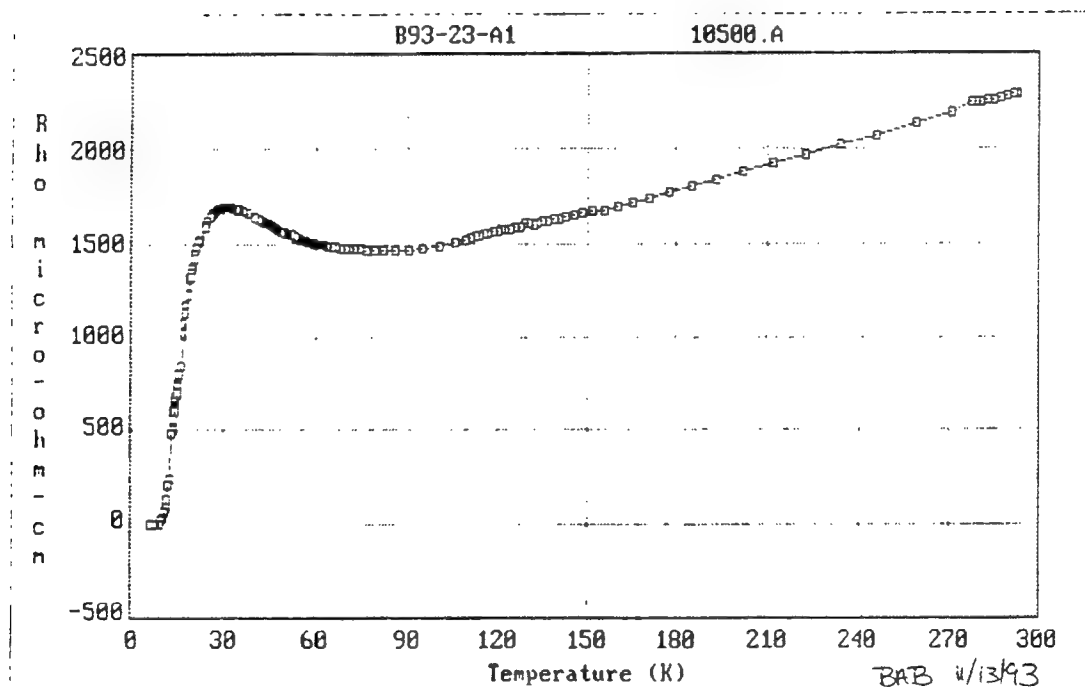


Figure 92. Resistivity vs. temperature for a Co/YBCO film on  $\text{LaAlO}_3$ . There is metallic behavior from room temperature to  $\sim 100$  K, then there is a rise in resistivity just above the transition.

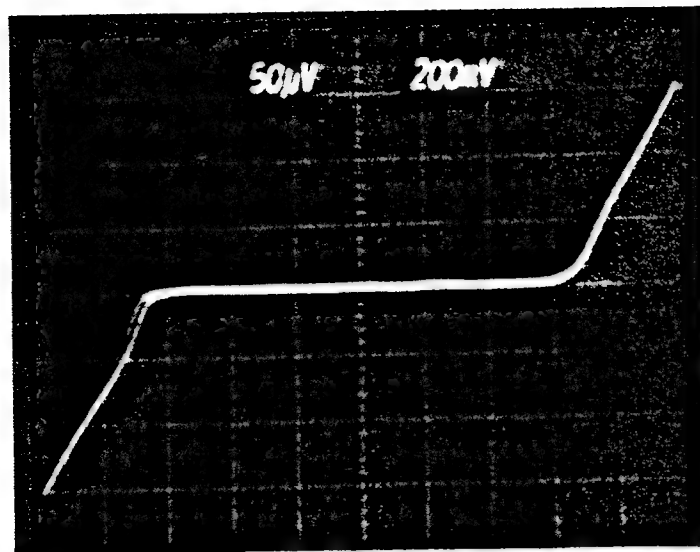


Figure 93. I-V characteristic for a YBCO SNS edge junction measured at  $T = 63.9$  K with a Co/YBCO barrier. Vertical axis is V, horizontal I, with  $x = 200 \mu\text{A}/\text{division}$ .

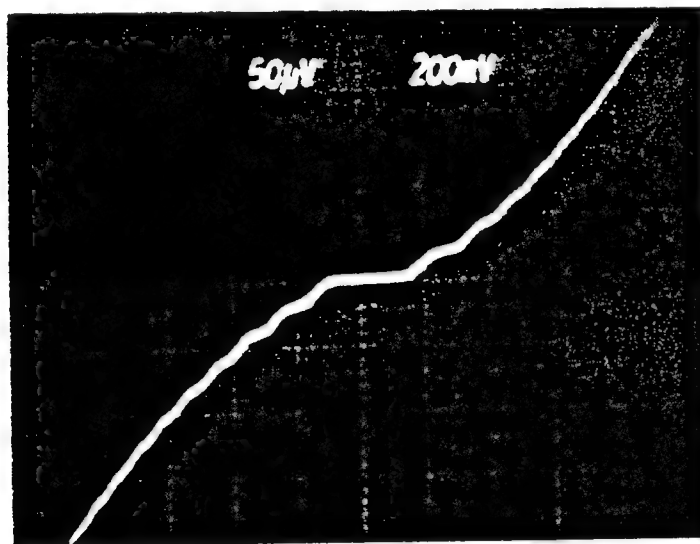


Figure 94. I-V characteristic of same junction as in Figure 93, showing Shapiro steps as a result of the application of 9.9 GHz radiation. This was measured at 64.7 K, and  $x=200 \mu\text{A}/\text{division}$ .



truly an SNS one and that Co-doped YBCO is a viable material for edge-junction barriers.

## Chapter VI. Conclusions

### A. Discussion of results

#### 1. BKBO Films

Work on this compound will not proceed at a rapid rate until sputtering targets can be fabricated reproducibly. This is not the only problem, however, since laser-ablated films made from stoichiometric targets made by Argonne National Laboratory had  $T_c$ 's of 28 K and  $J_c$ 's of  $> 1 \text{ MA/cm}^2$  [128], although not consistently. The most exasperating challenges are the difficulty in reproducibly depositing high-quality films due to target degradation and the volatility of the potassium, as well as the instability of the films themselves. Possible applications of junctions made from BKBO would be for infrared detectors [187] or for A/D converters. Electronics that degrade with time are unacceptable, unless society is suddenly as willing to purchase disposable computers as it is disposable cameras.

Such instability appears to be exacerbated by poor-quality films. Figure 60 shows a good-quality film (shiny blue, low resistivity) that was still of decent quality a year later (the  $T_c$  was very close to what it had been) although there was apparently a reaction of the top portion of film to form a non-conductive surface layer. The films represented in Figure 73 were dark green upon deposition and were not superconducting. [Most of the BKBO films were dark green; however, superconducting films have a metallic blue shine in reflection]. The peak splitting, assumed to be caused by randomly-oriented orthorhombic grains, points to the poor quality of these films. Two years after deposition, these films were retrieved for further analysis by x-ray diffraction. The films had totally degraded. They were colorless and the middle  $\{220\}$  peak, which had previously been 800 counts high, had shrunk to only 30 counts, with the side peaks in the noise. Any carbon dioxide in the air, which may be the cause of the degradation, since the surface layer consists

of carbonates, can more easily penetrate a poor-quality film which has more grain-boundary area and perhaps more defects such as microcracks or dislocations. Grain-boundary diffusion occurs more rapidly than diffusion through the lattice [188], as would diffusion through the relatively open structure around a strained area, especially for a small atom, as carbon is. Any exposed surface would readily degrade, since surface diffusion is the most rapid [188]. In addition, the greater the misorientation between grains, the more rapid the diffusion [189]. For this reason, one would make the assumption that a well-oriented material would be stable. It is obvious that this material will not be useful unless a method can be found to passivate it (such as the method used in this project of sputtering gold on top to passivate the BKBO and ensure good contact to it over time) and unless high-quality films can be made reproducibly.

All hope should not be abandoned, however. High-quality, stable films have been made. These films were junction-worthy and were also able to be used in a great number of experiments to try to understand the structural, electronic, and chemical nature of this still little-studied material. It remains a mystery why a BCS-like material with such a low density of states has such a high  $T_C$ . The variable-range hopping conduction displayed in certain cases is also a phenomenon worthy of further investigation. This compound is quite an interesting one for study. In addition, the discovery of superconductivity in BPBO and later in BKBO and Ba-Rb-Bi-O is what laid the groundwork for the discovery of the higher- $T_C$  superconductors. The rules formulated by A.W. Sleight and coworkers were the basis for investigation of new materials.

## 2. BKBO junctions

SIN junctions that used the native surface layer as the insulator were very useful for study, but because it is impossible to control the thickness of such a barrier, these junctions could not be used in device applications.

Grain-boundary junctions are also quite interesting for observing junction behavior and determining whether the material at the grain boundary is normal, insulating, perhaps superconducting at a lower temperature. Out of a series of BKBO grain-boundary junctions fabricated, only one worked and that one only briefly. These types of junctions are very difficult to reproduce and do not hold a great deal of promise for applications.

BKBO epitaxial trilayer junctions have the potential for being the most reproducible and useful, should the challenges of film-quality and an appropriate barrier material be overcome. The choice of a barrier is a difficult one. It would seem that MgO would be very compatible with BKBO since its lattice parameter is 4.212 Å, which is a mismatch of only 1.7%. However, BKBO films grown on MgO were of poor quality, with lower  $T_c$ 's (if any) and multiple orientations. MgO barriers grew as islands, as shown in the RHEED patterns in Figure 64. This may be because MgO has the NaCl structure, whereas BKBO is a perovskite. That fact may explain why BKBO consistently grew so well on SrTiO<sub>3</sub>, despite the 9% lattice mismatch between the two. However, SrTiO<sub>3</sub> grew as islands when used as a barrier. Perovskites with closer lattice matches to that of BKBO would warrant consideration. Barriers which were tried [57] were KNbO<sub>3</sub>, with lattice parameters of  $a = 3.971$  Å,  $b/\sqrt{2} = 4.027$  Å, and  $c/\sqrt{2} = 4.045$  Å, and KTaO<sub>3</sub>, with  $a = b = c = 3.989$  Å. There are also compounds such as BaTiO<sub>3</sub>, with  $a = b = 3.989$  Å,  $c = 4.029$  Å, or SrSnO<sub>3</sub>, which is 4.0334 Å, or the pseudocubic BaUO<sub>3</sub>, which is 4.387 Å, or BaSnO<sub>3</sub>, with a lattice parameter of 4.117 Å. The most promising

possibility from a dimensional view seems to be BaZrO<sub>3</sub>, with  $a = b = c = 4.192 \text{ \AA}$  [190].

One would have difficulty justifying the higher cost of the liquid helium necessary to cool BKBO junctions unless these junctions are more easily fabricated and are more reproducible than junctions made from higher- $T_c$  superconductors. So far this has not been the case. However, relatively little effort has been put into working with this material, yet four groups have already successfully fabricated SIS trilayer junctions. The challenges facing researchers from this material have also been present for other superconductors and were only overcome with time and patience. This material still has the advantages of isotropy, a relatively long coherence length, a much higher operating temperature than that of Nb junctions, thus allowing the use of closed-cycle helium refrigeration rather than requiring an endless supply of liquid helium, and the fact that operation at lower temperatures than those for the higher- $T_c$  superconductors greatly lowers the amount of noise present and thus reduces the risk of errors.

This project has allowed the quantification of the structural, chemical, and electronic properties of BKBO and a determination of what makes certain films better than others. It has led to the demonstration that various types of junctions can be made with this material and that epitaxy is achieved and interdiffusion or interfacial reactions are not a concern. Moreover, these materials can be patterned into junctions, apparently without degradation of the layers in the process. If the films can be made reproducibly and an appropriate barrier is used, chances are good that better-quality junctions could be made.

### 3. YBCO and barrier films

Initially, the same types of problems encountered with BKBO films were true of YBCO films. Degradation was seen in poor-quality, nonstoichiometric films. However, techniques have been established to reproducibly fabricate YBCO targets, so that films can be consistently deposited under the same conditions. In addition, YBCO has no volatile components, so a stoichiometric target composition can be easily reproduced in the film. A great deal is already known about this material, which makes developments with it that much easier.

This work has demonstrated that high-quality, single-orientation YBCO films can be made and that the challenge of anisotropy in this material can be overcome. In addition, it has shown that Co/YBCO and Ca/YBCO are both candidate materials for barriers if sputtering targets are of the proper composition, are reproducibly made, and do not degrade with time, and that single-orientation films of these materials can be made. The study and understanding of these materials are still in the initial stages, however.

### 4. YBCO edge junctions

It has been demonstrated that YBCO edge junctions can be made and that all materials in them can withstand patterning and the deposition of subsequent layers, although this is not always the case, and more investigation of these junctions must therefore be done. For example, deposition of the  $\text{SrTiO}_3$  insulator at high temperatures apparently degrades the YBCO beneath it by robbing it of oxygen. This problem seems to be worse when well-oriented insulators are grown which do not allow diffusion of oxygen to the base electrode. Challenges such as this must still be faced.

The edge junction configuration is desirable because it takes advantage of the fact that YBCO films prefer to grow in a *c*-axis orientation and it utilizes the greater conduction in the *a-b* plane while minimizing junction area in order to lower capacitance. High-quality electrodes can be made reproducibly and viable barrier materials have been found, so the challenges that remain are with consistently growing boulder-free YBCO electrodes, growing insulators that do not rob the electrodes of oxygen, and consistently growing good-quality, uniform barriers with low resistivities and the same  $T_C$ 's each time.

#### B. Suggestions for future research

1. Production of more BKBO grain-boundary junctions and measurement of their resistances to try to determine whether the material at the grain boundaries are normal or insulating would be of interest. Perhaps cleaving the junctions in some manner and attempting EDXS analysis at the step region would yield some useful information.
2. A different barrier material in BKBO trilayer junctions which grows uniformly is essential. If high-quality electrodes could be grown consistently, it would be of great interest to attempt to fabricate trilayer junctions with barrier materials not previously used and to observe the growth of the barrier by RHEED and LEED and to determine the conduction mechanisms through the junction, as was done for the BKBO/SrTiO<sub>3</sub>/BKBO junctions already fabricated.
3. Should such trilayer junctions be grown, it would be desirable to use much more precise photolithography in order to process well-defined junctions. Limiting junction size will lessen self-field effects seen in long Josephson junctions and will

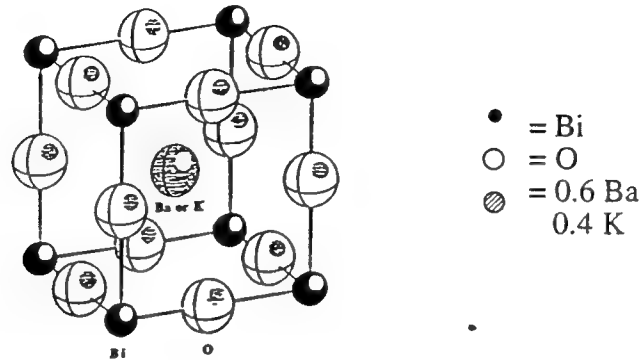
also lower capacitance. In addition, it greatly simplifies calculations when the area is known precisely.

4. It would be interesting to study different barrier materials for YBCO edge junctions. YBCO has been doped with many different elements and the effects on structural and electronic properties have been observed. Some of these compounds would be candidates for barriers. It would also be of interest to compare the growth of these barriers on YBCO to the growth of insulating barriers on BKBO.



## Appendix I. X-Ray Structure Factor Calculations

*Example 1:*  $\text{Ba}_{0.6}\text{K}_{0.4}\text{BiO}_3$  is a cubic perovskite. The structure of this compound is shown below:



The basis for this structure is given below:

Bi (0,0,0)  
 O ( $\frac{1}{2}, 0, 0$ )  
 O ( $0, \frac{1}{2}, 0$ )  
 O ( $0, 0, \frac{1}{2}$ )  
 0.6 Ba ( $\frac{1}{2}, \frac{1}{2}, \frac{1}{2}$ )  
 0.4 K ( $\frac{1}{2}, \frac{1}{2}, \frac{1}{2}$ )

The general form for the structure factor is [191]:

$$F_{hkl} = f_i e^{2\pi i(hu + kv + lw)} \quad (1)$$

When the basis for BKBO is substituted into the equation (1), the relation is then

$$F_{hkl} = f_{\text{Bi}} + f_{\text{O}} e^{h\pi i} + f_{\text{O}} e^{k\pi i} + f_{\text{O}} e^{l\pi i} + 0.6f_{\text{Ba}} e^{\pi i(h+k+l)} + 0.4f_{\text{K}} e^{\pi i(h+k+l)}$$

For example, specific reflections will have the following values:

$$F_{100} = f_{\text{Bi}} + f_{\text{O}} - 0.6f_{\text{Ba}} - 0.4f_{\text{K}} = F_{201} = F_{300} = F_{221}$$

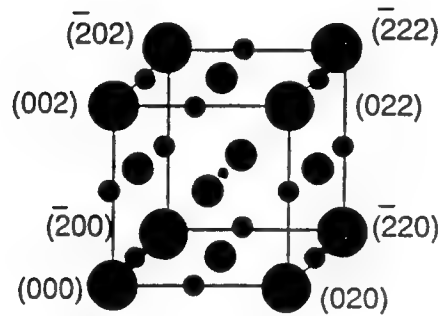
$$F_{110} = f_{\text{Bi}} - f_{\text{O}} + 0.6f_{\text{Ba}} + 0.4f_{\text{K}} = F_{211} = F_{310}$$

$$F_{111} = f_{\text{Bi}} - 3f_{\text{O}} - 0.6f_{\text{Ba}} - 0.4f_{\text{K}} = F_{311}$$

$$F_{200} = f_{\text{Bi}} + 3f_{\text{O}} + 0.6f_{\text{Ba}} + 0.4f_{\text{K}} = F_{220} = F_{222}$$

and so on. There are no reflections that are not allowed for this compound. The resulting reciprocal lattice pattern is shown below.

$$F_{200} > F_{110} > F_{100} > F_{111}$$



The positions of the peaks for the allowed reflections of a cubic material can be found using [192]

$$\sin^2 \theta = \frac{\lambda^2}{4a^2} (h^2 + k^2 + l^2) \quad (2)$$

using  $a = 4.283 \text{ \AA}$  [65] and  $\lambda = 1.542 \text{ \AA}$  for Cu  $K\alpha$  radiation and then using [165]

$$\frac{1}{d^2} = \frac{h^2 + k^2 + l^2}{a^2} \quad (3)$$

for a cubic material, one obtains the data given in Table I.

Table I. Positions of reflections calculated for BKBO

hkl	$h^2+k^2+l^2$	$\sin \theta$	$\theta$	$2\theta$	d
100	1	0.1800	10.37	20.74	4.283
110	2	0.2546	14.75	29.50	3.028
111	3	0.3118	18.17	36.33	2.473
200	4	0.3600	21.10	42.20	2.141
201	5	0.4026	23.74	47.47	1.915
500	25	0.900	64.16	128.32	0.8566

Note that  $h^2 + k^2 + l^2$  is the same for 300 and 221, so these reflections are both at  $65.37^\circ 2\theta$ . From Table I,  $\sin \theta/\lambda$  can be calculated and interpolation can be used to find atomic scattering factors from the data in Appendix 12 of Cullity [193]:

Table II. Calculated Atomic Scattering Factors

hkl	$\sin \theta/\lambda$	$f_K$	$f_{Ba}$	$f_{Bi}$	$f_O$
100	0.12	15.9	50.3	75.7	6.7
110	0.17	14.3	46.8	71.1	5.8
111	0.20	13.3	44.7	68.4	5.3
200	0.23	12.6	42.8	66.0	4.9

The intensity of powder pattern lines can be calculated from

$$I = |F|^2 P \left( \frac{1 + \cos^2 2\theta}{\sin^2 \theta \cos \theta} \right) e^{-2M} \quad (4)$$

where  $I$  is the relative integrated intensity,  $F$  is the structure factor,  $p$  is the multiplicity factor,  $\theta$  is the Bragg angle, and  $M$  depends on the amplitude of thermal vibration and the scattering angle  $2\theta$ . The term  $e^{-2M}$  is the Debye-Waller temperature factor and accounts for thermal vibrations of atoms. It is often neglected, however, so that the equation involves only the structure factor amplitude, the multiplicity factor for a given reflection, and the term in parentheses, which is the Lorentz-polarization factor [194].

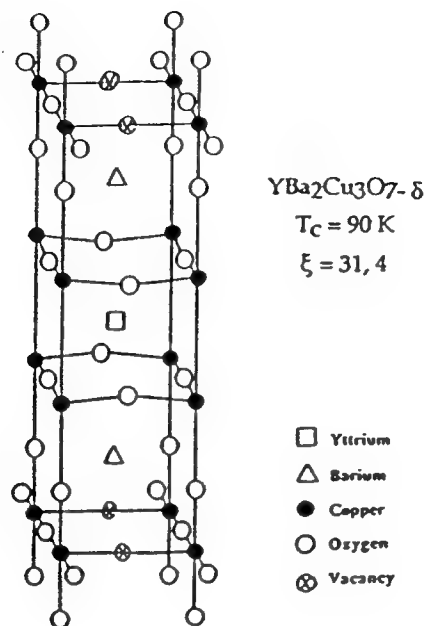
Multiplicity factors can be found in Appendix 13 of Cullity [195]. These account for the fact that a certain  $(hkl)$  actually represents a family of planes  $\{hkl\}$ . For example, a cubic material will have six  $\{100\}$  reflections. The Lorentz-polarization factors can be calculated from  $2\theta$  values. Calculations yielded the results given in Table III.

Table III. Calculated powder pattern intensities of BKBO reflections

$hkl$	$ F ^2$	$p$	LPF	$I$	$I/I_0$	$(I/I_0) \times 100$
100	2103.1	6	53.75	678,250	0.103	10
110	9820.8	24	27.94	6,585,436	1	100
111	414.5	8	17.96	59,555	0.009	0.9
200	12,414.4	6	12.89	960,130	0.146	14

Note that the intensities for 300 and 221 were added together, then the relative intensity was calculated from the sum.

*Example 2:* YBCO is an orthorhombic, perovskite-based structure. Its structure is shown below.



The basis for this structure, according to the atomic positions determined by Steinfink, et al. [137], will be that which is given below:

Basis:

Y ( $\frac{1}{2}, \frac{1}{2}, \frac{1}{2}$ )  
 Ba ( $\frac{1}{2}, \frac{1}{2}, 0.180$ )  
 Ba ( $\frac{1}{2}, \frac{1}{2}, 0.820$ )  
 Cu (0,0,0)  
 Cu (0,0,0.347)  
 Cu (0,0,0.653)  
 O ( $0, \frac{1}{2}, 0$ )  
 O (0,0,0.147)  
 O ( $\frac{1}{2}, 0, 0.358$ )  
 O ( $0, \frac{1}{2}, 0.358$ )  
 O ( $\frac{1}{2}, 0, 0.642$ )  
 O ( $0, \frac{1}{2}, 0.642$ )  
 O (0,0,0.853)

The structure factor would then be the following:

$$\begin{aligned}
F_{hkl} = & f_Y e^{\pi i(h+k+l)} + f_{Ba} e^{\pi i(h/2+k/2+(0.18)l)} + f_{Ba} e^{\pi i(h/2+k/2+(0.820)l)} + f_{Cu} + \\
& f_{Cu} e^{2\pi i(0.347)l} + f_{Cu} e^{2\pi i(0.653)l} + f_O e^{\pi i(h/2)} + f_O e^{\pi i(0.147)l} + f_O e^{\pi i(0.853)l} + \\
& f_O e^{2\pi i(h/2+(0.358)l)} + f_O e^{2\pi i(k/2+(0.358)l)} + f_O e^{2\pi i(h/2+(0.642)l)} + \\
& f_O e^{2\pi i(k/2+(0.642)l)}
\end{aligned}$$

Specific reflections could then be substituted into this and intensities calculated as in Example 1.

## Appendix II. Simmons Model for a rectangular barrier

The Simmons Model [184] can be used to model the barrier height and thickness of a tunnel junction from the I-V characteristic. Barrier height is determined by the size of the insulator gap and the difference in work functions of the electrodes and barrier. For an SIS junction, high-voltage data should be used where the I-V characteristic is linear. The author derived the following relation between current density, J, and applied voltage, V:

$$J = \beta (V + \gamma V^3) \quad (1)$$

$$\text{where } \beta = \{3e^2(2m\phi)^{1/2}/2h^2s\}\exp(-A\phi^{1/2}) \quad (2)$$

$$\text{and } \gamma = \{(Ae)^2/96\phi\} - \{Ae^2/32\phi^{1/2}\} \quad (3)$$

in which  $A = 4\pi(2m)^{1/2}s/h$ ,  $e$  = electronic charge,  $m$  = mass of electron,  $h$  = Planck's constant,  $s$  = electrode separation (barrier thickness), and  $\phi$  = barrier height at the electrode-insulator interface.

If one takes equation (1) and divides through by V, one obtains

$$I/AV = \beta + \beta\gamma V^2$$

If one then plots  $I/AV$  (conductance) vs.  $V^2$ , one obtains a slope of  $\beta\gamma$  and an intercept of  $\beta$ . These values can be substituted into equations (2) and (3), which can be solved simultaneously to find  $s$  and  $\phi$ .

### Appendix III - RHEED and LEED Patterns

For both LEED and RHEED,  $r_{hkl} \cdot d_{hkl} = \lambda L$

where

$r_{hkl}$  = distance from (000) to (hkl) on photograph (in cm)

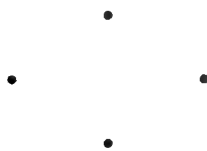
$d_{hkl}$  = distance from one hkl plane to the next

$\lambda$  = electron wavelength

$L$  = distance from sample to screen upon which image is projected

In our system, for RHEED,  $L = 17.5$  cm and  $E = 9000$  V, so  $\lambda L = 2.26$  Å·cm and for LEED,  $\lambda L = 54.0(E)^{-1/2}$  (Å·cm). The RHEED configuration is such that the beam approaches the sample at a glancing angle and is reflected onto a screen, whereas the beam is perpendicular to the sample surface in LEED and is reflected backward onto a wide-angle screen behind the beam source.

An example of a RHEED pattern is that for sample T92-83-S1, which was BKBO on SrTiO<sub>3</sub> (110). The pattern obtained was as shown below, with all distances between spots = 7.5 mm:



1. Using the values for the lattice parameter of  $a=4.283$  Å,  $d_{110}=3.029$  Å for BKBO and  $a=3.905$  Å for SrTiO<sub>3</sub>, one can calculate  $d_{hkl}$ .
2. For RHEED,  $\lambda L = 2.26$  Å·cm, which equals  $r_{hkl} \cdot d_{hkl}$ . It then follows that  $d = 2.26/r = 2.26$  Å·cm/ $0.75$  cm =  $3.01$  Å. The value of  $3.01$  Å obtained is close to that for  $d_{110}$  of BKBO, so this implies that the BKBO has assumed a (110) orientation in the growth direction.



3. The vertical direction on the photograph is always the growth direction of the film, so  $[110]$  must be the vertical direction. One can therefore assign the top spot to be  $(000)$  and the bottom to be  $(110)$ .
4. Since the interspot distances are all equal, the spots form equilateral triangles, which implies that all directions are at  $60^\circ$  to each other. It is therefore necessary to find directions  $60^\circ$  from  $[110]$ . The dot product of two directions can be found to determine the angle between directions. For example, consider the  $[101]$  and  $[110]$  directions:

$$\begin{aligned}
 [h_1 k_1 l_1] \bullet [h_2 k_2 l_2] &= |h_1 k_1 l_1| |h_2 k_2 l_2| \cos \theta \\
 h_1 h_2 + k_1 k_2 + l_1 l_2 &= \sqrt{h_1^2 + k_1^2 + l_1^2} \sqrt{h_2^2 + k_2^2 + l_2^2} \cos \theta \\
 [101] \bullet [110] &= \sqrt{2} \sqrt{2} \cos \theta \\
 1 &= 2 \cos \theta \\
 \theta &= 60^\circ
 \end{aligned}$$

5. The horizontal directions in the pattern could be any of a number of directions  $60^\circ$  from the  $[110]$  direction, depending on the angle of rotation of the sample about the  $[110]$  axis. For example, the various combinations of  $\langle 101 \rangle$  directions possible are these:

- (a)  $(000)$  to spot on right =  $[011]$ , spot on right to  $(110)$  spot =  $[10\bar{1}]$   
 so horizontal direction facing right is  $[\bar{1}12]$ , facing to left is  $[1\bar{1}\bar{2}]$
- (b) or could switch directions in (a) so that right is  $[1\bar{1}\bar{2}]$  and left is  $[\bar{1}12]$
- (c) another combination would be  $[101], [01\bar{1}]$ , with horizontal directions  $[1\bar{1}2]$  facing right and  $[\bar{1}1\bar{2}]$  facing left
- (d) or could switch directions in (c) so that  $[\bar{1}1\bar{2}]$  faces right and  $[1\bar{1}2]$  faces left

Suppose combination (a) is arbitrarily chosen. Once these assignments are made, the labelling becomes

$$\begin{array}{c}
 \bullet (000) \\
 \bullet (10\bar{1}) \quad \bullet (011) \\
 \bullet (110)
 \end{array}$$

and the direction out of the paper is set.

6. The direction of the beam (which comes straight out of the photograph) can be found by taking the cross product of two of the directions

$$\begin{aligned}
 [110] \times [\bar{1}12] &= \begin{vmatrix} i & j & k \\ 1 & 1 & 0 \\ \bar{1} & 1 & 2 \end{vmatrix} \\
 2i - 2j + 2k &= [1\bar{1}1]
 \end{aligned}$$

An example of a LEED pattern is that for sample T92-85-S1, which was BKBO on (110) SrTiO<sub>3</sub>. The pattern was obtained at 77 Volts.

$$\begin{array}{ccc}
 \bullet & \bullet & \text{A hexagonal pattern was seen, which one} \\
 & & \text{would find by looking down a } \langle 110 \rangle \\
 \bullet & \bullet & \text{direction} \\
 & & 
 \end{array}$$

- For LEED,  $\lambda L = 54.0/(E)^{1/2} = 6.154 \text{ \AA} \cdot \text{cm}$  when 77 V are used.
- Using  $\lambda L/r = d$ , one can calculate d-spacings for this film:  
 Horizontal distance  $d = 6.154 \text{ \AA} \cdot \text{cm} / 5.5 \text{ cm} = 1.12 \text{ \AA}$   
 Vertical distance  $d = 6.154 \text{ \AA} \cdot \text{cm} / 4.0 \text{ cm} = 1.54 \text{ \AA}$
- Considering the values for BKBO of  $d_{100}=4.283 \text{ \AA}$ ,  $d_{110}=3.029 \text{ \AA}$ ,  $d_{220}=1.51 \text{ \AA}$ , and  $d_{400}=1.07 \text{ \AA}$ , it is apparent that the horizontal distance is that of the  $d_{400}$  of BKBO and the vertical distance is the  $d_{220}$  of BKBO. The vertical direction of the pattern, which is the growth direction of the film, is therefore a  $\langle 110 \rangle$  and the horizontal direction is a  $\langle 100 \rangle$ .

4. Thus the directions could be

$$\begin{array}{c} [01\bar{1}] \bullet \rightarrow [100] \\ \downarrow \\ [011] \end{array}$$

## References

1. A.C. Rose-Innes and E.H. Rhoderick, *Introduction to Superconductivity*, New York: Pergamon Press, 1978, pp. 112-139.
2. L. Solymar and D. Walsh, *Lectures on the Electrical Properties of Materials*, New York: Oxford Science Publications, 1990, pp. 410-445.
3. N.W. Ashcroft and N.D. Mermin, *Solid State Physics*, Philadelphia: Holt, Rinehart, and Winston, 1976, p. 744.
4. C. Kittel, *Introduction to Solid State Physics*, New York: John Wiley and Sons, 1986, pp. 317-354.
5. Rose-Innes and Rhoderick, pp. 7-22.
6. B.I. Shklovskii, "Hopping Conduction in Lightly Doped Semiconductors (Review)," *Sov. Phys. - Semicond.*, vol. 6, pp. 1053-1075, 1973.
7. A. Miller and E. Abrahams, "Impurity Conduction at Low Concentrations," *Phys. Rev.*, vol. 120, pp. 745-755, 1960.
8. N.F. Mott, *Conduction in Non-Crystalline Materials*, Oxford: Clarendon Press, 1987, pp. 27-29.
9. T. Van Duzer and C.W. Turner, *Principles of Superconductive Devices and Circuits*, New York: Elsevier North Holland, Inc., 1981, p.291.
10. T.P. Orlando, E.J. McNiff, Jr., S. Foner, and M.R. Beasley, "Critical Fields, Pauli paramagnetic limiting, and material parameters of Nb<sub>3</sub>Sn and V<sub>3</sub>Si," *Phys. Rev. B*, vol. 19, pp. 4545-4561, 1979.
11. Rose-Innes and Rhoderick, pp. 31-39.
12. M. Tinkham, *Introduction to Superconductivity*, New York: Robert E. Krieger Publishing Co., 1980, pp. 104-142.
13. L. Solymar, *Superconductive Tunnelling and Applications*, London: Chapman and Hall, Ltd., 1972, p.55.
14. B.D. Josephson, "Possible New Effects in Superconductive Tunnelling," *Phys. Lett.*, vol. 1, pp. 251-253, 1962.
15. Van Duzer and Turner, p. 143.
16. Ibid, p. 208.
17. Ibid, p. 167.
18. J. Talvacchio, "Electrical Contact to Superconductors," *IEEE Transactions on Components, Hybrids, and Manufacturing Technology*, vol. 12, pp.21-31, March 1989.
19. T.P. Orlando and K.A. Delin, *Foundations of Applied Superconductivity*, New York: Addison-Wesley Publishing Company, 1991, pp. 393-447.
20. Ibid, p.247.
21. H. Kroger and U. Ghoshal, "Can Superconductive Digital Systems Compete with Semiconductor Systems?" *IEEE Transactions on Applied Superconductivity*, vol. 3, pp. 2307-2314, March 1993.

22. C. Hilbert, U. Ghoshal, and H. Kroger, "Superconducting Read-Out of CMOS RAM at Liquid Nitrogen Temperature," submitted to Appl. Phys. Lett.
23. R. Simon and A. Smith, *Superconductors: Conquering Technology's New Frontier*, New York: Plenum Press, 1990, pp. 169-191.
24. V.Z. Kresin and S.A. Wolf, *Fundamentals of Superconductivity*, New York: Plenum Press, 1990, pp. 155-168.
25. R. Simon and A. Smith, pp. 109-129.
26. V.Z. Kresin and S.A. Wolf, p. 110.
27. J.R. Gavaler, "Superconductivity in Nb-Ge films above 22 K," Appl. Phys. Lett., vol. 23, pp. 480-482, 1973.
28. M. Laguës, X.M. Xie, H. Tebbji, X.Z. Xu, V. Mairret, C. Hatterer, C.F. Beuran, and C. Deville-Cavelin, "Evidence Suggesting Superconductivity at 250 K in a Sequentially Deposited Cuprate Film," Science, vol. 262, pp. 1850-1852, Dec. 1993.
29. J.L. Tholence, B. Souletie, O. Laborde, J.J. Caponi, C. Chaillout, and M. Marezio, "Zero resistance around 250 K in superconducting Hg-compounds?" Physics Letters A, vol. 184, pp. 215-217, Jan. 1994.
30. A.W. Sleight, "Synthesis of Oxide Superconductors," Physics Today, vol. 44, pp. 24-30, June 1991.
31. A.W. Sleight, J.L. Gillson, and P.E. Bierstedt, "High-Temperature Superconductivity in the  $\text{BaPb}_{1-x}\text{Bi}_x\text{O}_3$  System," Solid State Commun., vol. 17, pp. 27-28, 1975.
32. L.F. Mattheiss and D.R. Hamann, "Electronic Structure of  $\text{BaPb}_{1-x}\text{Bi}_x\text{O}_3$ ," Phys. Rev. B, vol. 28, pp. 4227-4241, 1983.
33. W. Weber, in *Proceedings of the 18th International Conference on Low Temperature Physics* (Jpn. J. Appl. Phys., vol. 26, Suppl. 3, p. 981, 1987).
34. C.W. Chu, S. Huang, and A.W. Sleight, "Hydrostatic Pressure Effect on  $T_c$  of  $\text{Ba}_{0.9}\text{K}_{0.1}\text{Pb}_{0.75}\text{Bi}_{0.25}\text{O}_3$ ," Solid State Commun., vol. 18, pp. 977-979, 1976.
35. L.F. Mattheiss, E.M. Gyorgy, and D.W. Johnson, Jr., "Superconductivity above 20 K in the Ba-K-Bi-O System," Phys. Rev. B, vol. 37, pp. 3745-3746, 1988.
36. L.F. Mattheiss and D.R. Hamann, "Electronic Structure of the High- $T_c$  Superconductor  $\text{Ba}_{1-x}\text{K}_x\text{BiO}_3$ ," Phys. Rev. Lett., vol. 60, pp. 2681-2684, 1988.
37. R.J. Cava, B. Batlogg, J.J. Krajewski, R. Farrow, L.W. Rupp, Jr., A.E. White, K. Short, W.F. Peck, and T. Kometani, "Superconductivity near 30 K without copper: the  $\text{Ba}_{0.6}\text{K}_{0.4}\text{BiO}_3$  perovskite," Nature, vol. 332, pp. 814-816, 1988.
38. I. Giaever, "Electron Tunneling between two superconductors," Phys. Rev. Lett., vol. 5, pp. 464-466, 1960.
39. J. Nicol, S. Shapiro, and P.H. Smith, "Direct Measurement of the Superconducting Energy Gap," Phys. Rev. Lett., vol. 5, pp. 461-464, 1960.
40. P.W. Anderson and J.M. Rowell, "Probable Observation of the Josephson Superconducting Tunneling Effect," Phys. Rev. Lett., vol. 10, pp. 230-232, 1963.
41. R.E. Howard, E.L. Hu, L.D. Jackel, L.A. Fetter, and R.H. Bosworth, "Small-area high-current-density Josephson junctions," Appl. Phys. Lett., vol. 35, pp. 879-881, Dec. 1979.

42. R.F. Broom, A. Oosenbrug, and W. Walter, "Josephson junctions of small area formed on the edges of niobium films," *Appl. Phys. Lett.*, vol. 37, pp. 237-239, July 1980.
43. G. Dousselin and J. Rosenblatt, "Behavior of edge-grown low-capacitance superconducting tunnel junctions," *J. Appl. Phys.*, vol. 51, pp. 802-804, Jan. 1980.
44. A.W. Kleinsasser and R.A. Buhrman, "High-quality submicron niobium tunnel junctions with reactive-ion-beam oxidation," *Appl. Phys. Lett.*, vol. 37, pp. 841-843, Nov. 1980.
45. D.F. Moore, P. Vettiger, and T. Forster, "High current-density Josephson edge-junction capacitance," *Physica B & C*, vol. 108 B & C, pp. 983-984, 1981.
46. R.B. Laibowitz, R.H. Koch, A. Gupta, G. Koren, W.J. Gallagher, V. Foglietti, B. Oh, and J.M. Viggiano, "All high  $T_C$  edge junctions and SQUIDS," *Appl. Phys. Lett.*, vol. 56, pp. 686-688, Feb. 1990.
47. G. Koren, E. Polturak, E. Aharoni, and D. Cohen, "Characteristics of all-YBa<sub>2</sub>Cu<sub>3</sub>O<sub>7</sub> edge junctions operating above 80 K," *Appl. Phys. Lett.*, vol. 59, pp. 2745-2747, Nov. 1991.
48. R.P. Robertazzi, R.H. Koch, R.B. Laibowitz, and W.J. Gallagher, "Y<sub>1</sub>Ba<sub>2</sub>Cu<sub>3</sub>O<sub>7</sub>/MgO/Y<sub>1</sub>Ba<sub>2</sub>Cu<sub>3</sub>O<sub>7</sub> edge Josephson junctions," *Appl. Phys. Lett.*, vol. 61, pp. 711-713, August 1992.
49. J.B. Barner, B.D. Hunt, M.C. Foote, W.T. Pike, and R.P. Vasquez, "YBa<sub>2</sub>Cu<sub>3</sub>O<sub>7- $\delta$</sub> -based, edge-geometry SNS Josephson junctions with low-resistivity PrBa<sub>2</sub>Cu<sub>3</sub>O<sub>7- $\delta$</sub>  barriers," *Physica C*, vol. 207, pp. 382-389, 1993.
50. K. Char, M.S. Colclough, T.H. Geballe, and K.E. Myers, "High  $T_C$  Superconductor-normal-superconductor Josephson junctions using CaRuO<sub>3</sub> as the metallic barrier," *Appl. Phys. Lett.*, vol. 62, pp. 196-198, Jan. 1993.
51. Q.Y. Ying, C. Hilbert, and H. Kroger, "Fabrication and tunneling characteristics of low-leakage all-YBa<sub>2</sub>Cu<sub>3</sub>O<sub>7- $x$</sub>  edge junctions," *IEEE Transactions on Applied Superconductivity*, vol. 3, pp. 2277-2280, March 1993.
52. L. Antognazza, K. Char, T.H. Geballe, L.L.H. King, and A.W. Sleight, "Josephson coupling of YBa<sub>2</sub>Cu<sub>3</sub>O<sub>7- $x$</sub>  through a ferromagnetic barrier SrRuO<sub>3</sub>," *Appl. Phys. Lett.*, vol. 63, pp. 1005-1007, Aug. 1993.
53. K. Char, L. Antognazza, and T.H. Geballe, "Study of interface resistances in epitaxial YBa<sub>2</sub>Cu<sub>3</sub>O<sub>7- $x$</sub> /barrier/YBa<sub>2</sub>Cu<sub>3</sub>O<sub>7- $x$</sub>  junctions," to be published in *Appl. Phys. Lett.*
54. Y. Enomoto and K. Moriwaki, "Electrical Properties of Boundary between YBa<sub>2</sub>Cu<sub>3</sub>O<sub>7- $\delta$</sub>  and Ba<sub>1- $x$</sub> K <sub>$x$</sub> BiO<sub>3</sub> Thin Films," *Jpn. J. Appl. Phys.*, vol. 29, pp. L1455-L1457, 1990.
55. R.L. Fink, M. Thompson, C. Hilbert, and H. Kroger, "Hysteretic Josephson junctions from YBa<sub>2</sub>Cu<sub>3</sub>O<sub>7- $x$</sub> /SrTiO<sub>3</sub>/Ba<sub>1- $x$</sub> K <sub>$x$</sub> BiO<sub>3</sub> trilayer films," *Appl. Phys. Lett.*, vol. 61, pp. 595-597, 1992.
56. E.S. Hellman, S. Martin, E.H. Hartford Jr., D.J. Werder, G.M. Roesler Jr., and P.M. Tedrow, "Ba<sub>1- $x$</sub> K <sub>$x$</sub> BiO<sub>3</sub> sandwich-type tunnel junctions grown by molecular beam epitaxy," *Physica C*, vol. 201, pp. 166-170, 1992.

57. R.L. Fink, M. Thompson, C. Hilbert, and H. Kroger, "Hysteretic Josephson Junctions from High  $T_c$  Superconducting Thin Films," *IEEE Transactions on Applied Superconductivity*, vol. 3, pp. 22199-2221, March 1993.
58. B.A. Baumert, J. Talvacchio, and M.G. Forrester, "SrTiO<sub>3</sub> Buffer Layers and Tunnel Barriers for Ba-K-Bi-O Junctions," *Appl. Phys. Lett.*, vol. 62, pp.2137-2139, April 1993.
59. J. Amano, H. Ko, M. Narbutovskih, J. Sheats, and K. Tibbs, "Superconducting Ba<sub>1-x</sub>K<sub>x</sub>BiO<sub>3</sub> thin films and junctions," *J. Appl. Phys.*, vol. 74, pp.4620-4626, October 1993.
60. A. Kussmaul, E.S. Hellman, E.H. Hartford, Jr., and P.M. Tedrow, "Superconductor-insulator-superconductor tunneling in Ba<sub>1-x</sub>K<sub>x</sub>BiO<sub>3</sub> grain boundaries," *Appl. Phys. Lett.*, vol. 63, pp. 2824-2826, Nov. 1993.
61. H. Suzuki, S. Suzuki, M. Iyori, T. Yamamoto, K. Takahashi, T. Usuki, Y. Yoshisato and S. Nakano, "Characteristics of Au/Ba<sub>1-x</sub>K<sub>x</sub>BiO<sub>3</sub>/SrTiO<sub>3</sub>(Nb) Superconducting-Base Transistor," *IEEE Transactions on Applied Superconductivity*, vol. 3, pp. 2906-2909, March 1993.
62. D. Tseng and E. Ruckenstein, "Structure and Superconductivity of BaBiO<sub>3</sub> doped with alkali ions," *J. Mater. Res.*, vol. 5, pp. 742-745, April 1990.
63. D.G. Hinks, D.R. Richards, B. Dabrowski, A.W. Mitchell, J.D. Jorgensen, and D.T. Marx, "Oxygen Content and the Synthesis of Ba<sub>1-x</sub>K<sub>x</sub>BiO<sub>3-y</sub>," *Physica C*, vol. 156, pp. 477-480, 1988.
64. W. Jin, M.H. Degani, R. Kalia, and P. Vashishta, "Superconductivity in Ba<sub>1-x</sub>K<sub>x</sub>BiO<sub>3</sub> cubic oxides," *Phys. Rev. B*, vol. 45, pp.5535-5546, March 1992.
65. S. Pei, J.D. Jorgensen, B. Dabrowski, D.G. Hinks, D.R. Richards, A.E. Mitchell, J.M. Newsam, S.K. Sinha, D. Vaknin, and A.J. Jacobson, "Structural phase diagram of the Ba<sub>1-x</sub>K<sub>x</sub>BiO<sub>3</sub> system," *Phys. Rev. B*, vol. 41, pp. 4126-4141, 1990.
66. S. Pei, J.D. Jorgensen, D.G. Hinks, Y. Zheng, D.R. Richards, B. Dabrowski, and A.W. Mitchell, "Structure and Chemistry of Ba<sub>1-x</sub>K<sub>x</sub>BiO<sub>3-d</sub> at High Temperature," *J. Solid State Chem.*, vol. 95, pp. 29-38, 1991.
67. M.T. Weller, J.R. Grasmeyer, P.C. Lanchester, P.A.J. DeGroot, G.P. Rapson, and A.C. Hannon, "The Structure and Superconducting Properties of Ba<sub>0.7</sub>K<sub>0.3</sub>BiO<sub>2.91</sub>," *Physica C*, vol. 156, pp. 265-268, 1988.
68. L.F. Schneemeyer, J.K. Thomas, T. Siegrist, B. Batlogg, L.W. Rupp, R.L. Opila, R.J. Cava, and D.W. Murphy, "Growth and structural characterization of superconducting Ba<sub>1-x</sub>K<sub>x</sub>BiO<sub>3</sub> single crystals," *Nature*, vol. 335, pp. 421-423, 1988.
69. M.S. Hegde, P. Barboux, C.C. Chang, J.M. Tarascon, T. Venkatesan, X.D. Wu and A. Inam, "Electronic Structure of high- $T_c$  Ba<sub>0.6</sub>K<sub>0.4</sub>BiO<sub>3</sub> by x-ray photoelectron spectroscopy," *Phys. Rev. B*, vol. 39, pp. 4752-4755, 1989.
70. K. Ueki, A. Tokiwa, M. Kikuchi, T. Suzuki, M. Nagoshi, R. Suzuki, N. Kobayashi, and Y. Syono, "Valence State of Ba<sub>1-x</sub>K<sub>x</sub>BiO<sub>3-d</sub> Superconductor Controlled by the Oxygen Content," in *Advances in Superconductivity II*, Tsukuba, Japan, 1989, pp. 489-492.
71. Y. Idemoto, Y. Iwata and K. Fueki, "Oxygen content and  $T_c$  of Ba<sub>0.6</sub>K<sub>0.4</sub>BiO<sub>3-d</sub>," *Physica C*, vol. 201, pp. 43-49, 1992.

72. D.G. Hinks, B. Dabrowski, J.D. Jorgensen, A.W. Mitchell, D.R. Richards, S. Pei, and D. Shi, "Synthesis, structure and superconductivity in the  $\text{Ba}_{1-x}\text{K}_x\text{BiO}_{3-y}$  system," *Nature*, vol. 333, pp. 836-838, 1988.
73. Q. Huang, J.F. Zasadzinski, N. Tralshawala, K.E. Gray, D.G. Hinks, J.L. Peng, and R.L. Greene, "Tunnelling evidence for predominantly electron-phonon coupling in superconducting  $\text{Ba}_{1-x}\text{K}_x\text{BiO}_3$  and  $\text{Nd}_{2-x}\text{Ce}_x\text{CuO}_{4-y}$ ," *Nature*, vol 347, pp. 369-372, 1990.
74. H. Sato, H. Takagi, and S. Uchida, "Gap observation by tunneling measurement on superconducting  $\text{Ba}_{1-x}\text{K}_x\text{BiO}_3$  Thin Films: A Finite Energy Gap in  $\text{Ba}_{1-x}\text{K}_x\text{BiO}_3$ ," *Physica C*, vol. 169, pp. 391-395, 1990.
75. H. Suzuki, M. Iyori, K. Shimaoka, K. Yamano, T. Yamamoto, M. Kamino, K. Takahashi, T. Usuki, Y. Yoshisato and S. Nakano, "Preparation and Characterization of a Superconductor-Semiconductor Junction:  $\text{Ba}_{1-x}\text{K}_x\text{BiO}_3/\text{Nb-doped SrTiO}_3$ ," *International Symposium on Superconductivity*, Japan, 1991.
76. B.M. Moon, C.E. Platt, R.A. Schweinfurth, and D.J. Van Harlingen, "In-situ pulsed laser deposition of superconducting  $\text{Ba}_{1-x}\text{K}_x\text{BiO}_3$  thin films," *Appl. Phys. Lett.*, vol. 59, pp. 1905-1907, 1991.
77. C.J. Hou, R.L. Fink, C. Hilbert, and H. Kroger, "Low-leakage thin-film superconductor-insulator-normal metal tunnel junctions on co-evaporated  $\text{Ba}_{1-x}\text{Rb}_x\text{BiO}_3$  and rf-sputtered  $\text{Ba}_{1-x}\text{K}_x\text{BiO}_3$ ," *Appl. Phys. Lett.*, vol. 60, pp. 1262-1264, 1992.
78. A.N. Pargellis, F. Sharifi, R.C. Dynes, B. Miller, E.S. Hellman, J.M. Rosamilia, and E.H. Hartford, Jr., "All-high  $T_C$  Josephson tunnel junction:  $\text{Ba}_{1-x}\text{K}_x\text{BiO}_3/\text{Ba}_{1-x}\text{K}_x\text{BiO}_3$  junctions," *Appl. Phys. Lett.*, vol. 58, pp. 95-96, 1991.
79. F. Sharifi, A. Pargellis, R.C. Dynes, B. Miller, E.S. Hellman, J. Rosamilia, and E.H. Hartford, Jr., "Electron tunneling in the high- $T_C$  bismuthate superconductors," *Phys. Rev. B*, vol. 44, pp. 12521-12524, 1991.
80. J.F. Zasadzinski, N. Tralshawala, D.G. Hinks, B. Dabrowski, A.W. Mitchell, and D.R. Richards, "Tunneling Spectroscopy in Superconducting  $\text{Ba}_{1-x}\text{K}_x\text{BiO}_3$ : Direct Evidence for Phonon-mediated coupling," *Physica C*, vol. 158, pp. 519-524, 1989.
81. Y. Liu, J.F. Whitaker, and C.E. Platt, "Terahertz Spectroscopy of Superconducting Thin Film  $\text{Ba}_{0.6}\text{K}_{0.4}\text{BiO}_3$ ," submitted to the Ultrafast Electronics and Optoelectronics Conference, San Francisco, CA, Jan. 25-27, 1993.
82. M.S. Pambianchi, S.M. Anlage, E.S. Hellman, E.H. Hartford, Jr., M. Bruns, and S.Y. Lee, "Penetration depth, microwave surface resistance, and gap ratio in  $\text{NbN}$  and  $\text{Ba}_{1-x}\text{K}_x\text{BiO}_3$  thin films," *Appl. Phys. Lett.*, vol. 64, pp. 244-246, Jan. 1994.
83. D.G. Hinks, B. Dabrowski, D.R. Richards, J.D. Jorgensen, S. Pei, and J.F. Zasadzinski, "Evidence for Phonon-mediated coupling in superconducting  $\text{Ba}_{0.6}\text{K}_{0.4}\text{BiO}_3$ ," in *High Temperature Superconductors: Relationships between Properties, Structure, and Solid-State Chemistry*, San Diego, CA, April 1989, pp. 357-367.
84. D.G. Hinks, D.R. Richards, B. Dabrowski, D.T. Marx, and A.W. Mitchell, "The Oxygen Isotope Effect in  $\text{Ba}_{0.625}\text{K}_{0.375}\text{BiO}_3$ ," *Nature*, vol. 335, pp. 419-421, 1988.



85. S. Kondoh, M. Sera, Y. Ando, and M. Sato, "Normal State Properties and Oxygen Isotope Effect of (Ba,K)BiO<sub>3</sub>," *Physica C*, vol. 157, pp. 469-477, 1989.
86. C.K. Loong, D.G. Hinks, P. Vashishta, W. Jin, R.K. Kalia, M.H. Degani, D.L. Price, J.D. Jorgensen, B. Dabrowski, A.W. Mitchell, D.R. Richards, and Y. Zheng, "Oxygen Isotope Effect in Superconducting Ba<sub>1-x</sub>K<sub>x</sub>BiO<sub>3</sub> from Phonon Density of States," *Phys. Rev. Lett.*, vol. 66, pp. 3217-3220, 1991.
87. K.F. McCarty, H.B. Radousky, D.G. Hinks, Y. Zheng, A.W. Mitchell, T.J. Folkerts, and R.N. Shelton, "Electron-phonon coupling in superconducting Ba<sub>0.6</sub>K<sub>0.4</sub>BiO<sub>3</sub>: A Raman scattering study," *Phys. Rev. B*, vol. 40, pp. 2662-2665, 1989.
88. C.K. Loong, P. Vashishta, R.K. Kalia, M.H. Degani, D.L. Price, J.D. Jorgensen, D.G. Hinks, B. Dabrowski, A.W. Mitchell, D.R. Richards, and Y. Zheng, "High-Energy Oxygen Phonon Modes and Superconductivity in Ba<sub>1-x</sub>K<sub>x</sub>-BiO<sub>3</sub>: An Inelastic-Neutron-Scattering Experiment and Molecular-Dynamics Simulation," *Phys. Rev. Lett.*, vol. 62, pp. 2628-2631, 1989.
89. Z. Schlesinger, R.T. Collins, J.A. Calise, D.G. Hinks, A.W. Mitchell, Y. Zheng, B. Dabrowski, and N.E. Bickers, "Superconducting energy gap and a normal-state excitation in Ba<sub>0.6</sub>K<sub>0.4</sub>BiO<sub>3</sub>," *Phys. Rev. B*, vol. 40, pp. 6862-6866, 1989.
90. J.P. Wignacourt, J.S. Swinnea, H. Steinfink, and J.B. Goodenough, "Oxygen atom thermal vibration anisotropy in Ba<sub>0.87</sub>K<sub>0.13</sub>BiO<sub>3</sub>," *Appl. Phys. Lett.*, vol. 53, pp. 1753-1755, 1988.
91. Y. Ono, K. Yamauchi, and N. Yamada, "Anomalous Changes of Structural Parameters at T<sub>c</sub> in the Superconductor Ba<sub>0.7</sub>K<sub>0.3</sub>BiO<sub>3</sub>," *Jpn. J. Appl. Phys.*, vol. 30, pp. L182-L184, 1991.
92. K.C. Ott, M.F. Hundley, G.H. Kwei, M.P. Maley, M.E. McHenry, E.J. Peterson, J.D. Thompson, and J.O. Willis, "Barium Potassium Bismuth Oxide: Synthesis and Physical Properties," in *High Temperature Superconductors: Relationships between Properties, Structure, and Solid-State Chemistry*, San Diego, CA, April 1989, pp. 369-376.
93. S.D. Peacor, R.A. Richardson, J. Burm, C. Uher, and A.B. Kaiser, "Thermal conductivity of Ba-K-Bi-O: A Contrast to copper oxide superconductors," *Phys. Rev. B*, vol. 42, pp. 2684-2687, 1990.
94. J.E. Graebner, L.F. Schneemeyer, and J.K. Thomas, "Heat capacity of superconducting Ba<sub>0.6</sub>K<sub>0.4</sub>BiO<sub>3</sub> near T<sub>c</sub>," *Phys. Rev. B*, vol. 39, pp. 9682-9684, 1989.
95. M. Shirai, N. Suzuki, and K. Motizuki, "Electron-lattice interaction and superconductivity in BaPb<sub>1-x</sub>Bi<sub>x</sub>O<sub>3</sub> and Ba<sub>1-x</sub>K<sub>x</sub>BiO<sub>3</sub>," *J. Phys. Condens. Matter*, vol. 2, pp. 3553-3566, 1990.
96. A.I. Liechtenstein, I.I. Mazin, C.O. Rodriguez, O. Jepsen, and O.K. Andersen, "Structural phase diagram and electron-phonon interaction in Ba<sub>1-x</sub>K<sub>x</sub>BiO<sub>3</sub>," *Phys. Rev. B*, vol. 44, pp. 5388-5391, 1991.
97. M.J. Rice and Y.R. Wang, "Interpretation of Ba<sub>1-x</sub>K<sub>x</sub>BiO<sub>3</sub> as a Doped Peierls Insulator," *Physica C*, vol. 157, pp. 192-197, 1989.
98. N. Hamada, S. Massidda, A.J. Freeman, and J. Redinger, "Electronic structure, photoemission, inverse photoemission, and x-ray emission spectra of superconducting Ba<sub>1-x</sub>K<sub>x</sub>BiO<sub>3</sub>," *Phys. Rev. B*, vol. 40, pp. 4442-4452, 1989.

99. H.C. Gupta, "Phonons in High- $T_c$   $Ba_{0.6}K_{0.4}BiO_3$ ," *Physica C*, vol. 158, pp. 153-154, 1989.
100. R.J. Cava and B. Batlogg, "Superconductivity at High Temperatures Without Copper:  $Ba_{1-x}K_xBiO_3$ ," *MRS Bulletin*, vol. XIV, pp. 49-52, Jan. 1989.
101. A.W. Sleight, "Chemistry of Oxide Superconductors," in *High Temperature Superconductivity*, St. Andrews, Scotland, June 1991, pp. 97-143.
102. D.E. Cox and A.W. Sleight, "Mixed-Valent  $Ba_2Bi^{+3}Bi^{+5}O_6$ : Structure and Properties vs. Temperature," *Acta Crystallogr.*, vol. B35, pp. 1-10, Jan. 1979.
103. R.C. Taylor, M.M. Plechaty, and D.B. Beach, "Chemical Determination of Hole Location in the Superconducting System  $Ba_{1-x}K_xBiO_3$ ," *Mat. Res. Bull.*, vol. 26, pp. 1185-1192, 1991.
104. E.S. Hellman and E.H. Hartford, Jr., "Normal State Resistivity and Hall Effect in  $Ba_{1-x}K_xBiO_3$  Epitaxial Films," *Phys. Rev. B.*, vol. 47, pp. 11,346-11,353, May 1993.
105. H. Sato, S. Tajima, H. Takagi, and S. Uchida, "Optical study of the metal-insulator transition on  $Ba_{1-x}K_xBiO_3$  thin films," *Nature*, vol. 338, pp. 241-243, 1989.
106. M. Affronte, J. Marcus, and C. Escribe-Filippini, "Transport Properties of  $Ba_{1-x}K_xBiO_3$  Single Crystals," *Solid State Commun.*, vol. 85, pp. 501-506, 1993.
107. H. Takahashi, N. Mori, Y. Nagata, S. Nakamura, T. Uchida, J. Akimitsu, and Y. Tokura, "High pressure study on the superconducting transition temperature and Hall coefficient of  $Ba_{1-x}K_xBiO_3$  up to 8 GPa," *Physica C*, vol. 210, p. 485, 1993.
108. N.L. Jones, J.B. Parise, R.B. Flippin, and A.W. Sleight, "Superconductivity at 34 K in the K/Ba/Bi/O System," *J. Solid State Chem.*, vol. 78, pp. 319-321, 1989.
109. H. Uwe, T. Osada, A. Iyo, K. Murata, and T. Sakudo, "Pressure Effect on Superconducting  $Ba_{1-x}K_xBiO_3$  and  $BaPb_{1-x}Bi_xO_3$ ," *Physica C*, vol. 162-164, pp. 743-744, 1989.
110. J.E. Schirber, B. Morosin, and D.S. Ginley, "Effect of Pressure on the Superconducting Transition Temperature of  $Ba_{1-x}K_xBiO_3$ ," *Physica C*, vol. 157, pp. 237-239, 1989.
111. M.L. Norton, "The Chemistry of High  $T_c$  in the Bismuth-Based Oxide Superconductors  $BaPb_{1-x}Bi_xO_3$  and  $Ba_{1-x}K_xBiO_3$ ," in *Chemistry of Superconductor Materials*, Park Ridge, N.J.: Noyes Publications, 1992, pp. 347-379.
112. R. Hu, A.E. Lee, H.W. Chan, and C.L. Pettiette-Hall, "Superconducting  $Ba_{1-x}K_xBiO_3$  Thin Films by in-situ sputtering," *IEEE Transactions on Applied Superconductivity*, vol. 3, pp. 1556-1558, March 1993.
113. R.C. Lacoe, J.P. Wendt, and P.M. Adams, "Deposition of Barium Potassium Bismuth Oxide (BKBO) Thin Films by Laser Ablation," *IEEE Transactions on Applied Superconductivity*, vol. 3, pp. 1563-1566, March 1993.

114. S. Jin, T.H. Tiefel, R.C. Sherwood, A.P. Ramirez, E.M. Gyorgy, G.W. Kammlott, and R.A. Fastnacht, "Transport measurement of 32 K superconductivity in the Ba-K-Bi-O System," *Appl. Phys. Lett.*, vol. 53, pp. 1116-1118, 1988.
115. D.G. Hinks, A.W. Mitchell, Y. Zheng, D.R. Richards, and B. Dabrowski, "Synthesis of high-density  $\text{Ba}_{1-x}\text{K}_x\text{BiO}_3$  superconducting samples," *Appl. Phys. Lett.*, vol. 54, pp. 1585-1587, 1989.
116. C. Kittel, p. 150.
117. B. Dabrowski, D.G. Hinks, J.D. Jorgensen, R.K. Kalia, P. Vashishta, D.R. Richards, D.T. Marx and A.W. Mitchell, "Variable-Range Hopping Conduction in  $\text{Ba}_{1-x}\text{K}_x\text{BiO}_{3-y}$  System," *Physica C*, vol. 156, pp. 24-26, 1988.
118. D. Tseng and E. Ruckenstein, "Some Improvement in the  $T_c$  of Bismuth-Based Superconducting Compounds," *Materials Letters*, vol. 8, pp. 69-71, 1989.
119. E.S. Hellman, B. Miller, J.M. Rosamilia, E.H. Hartford, and K.W. Baldwin, "Variable-range-hopping transport in  $\text{Ba}_{1-x}\text{K}_x\text{BiO}_3$  ( $0 < x < 0.35$ )," *Phys. Rev. B*, vol. 44, pp. 9719-9722, 1991.
120. J.B. Torrance, A. Bezinge, A.I. Nazzal, and S.S.P. Parkin, "Disappearance of High Temperature Superconductivity Induced by High Carrier Concentrations," *Physica C*, vol. 162-164, pp. 291-295, 1989.
121. B. Batlogg, *Mechanisms of High Temperature Superconductivity*, Berlin: Springer-Verlag, 1989, pp. 324-331.
122. G.T. Seidler, T.F. Rosenbaum, P.D. Han, D.A. Payne, and B.W. Veal, "Critical fields and flux pinning in single crystal  $\text{Ba}_{1-x}\text{K}_x\text{BiO}_3$ ," *Physica C*, vol. 195, pp. 373-378, 1992.
123. B. Batlogg, R.J. Cava, L.W. Rupp, Jr., A.M. Mujsce, J.J. Krajewski, J.P. Remeika, W.F. Peck, Jr., A.S. Cooper, and G.P. Espinosa, "Density of States and Isotope Effect in BiO Superconductors: Evidence for Nonphonon Mechanism," *Phys. Rev. Lett.*, vol. 61, pp. 1670-1673, 1988.
124. C. Escribe-Filippini, J. Marcus, M. Affronte, H. Rakoto, J.M. Broto, J.C. Ousset, and S. Askenazy, "Upper critical field of  $\text{Ba}_{1-x}\text{K}_x\text{BiO}_3$  single crystal," *Physica C*, vol. 210, pp. 133-137, 1993.
125. D. McK. Paul, E.M. Forgan, R. Cubitt, S.L. Lee, H.A. Mook, and P. Timmins, "Neutron Scattering from the Flux Lattice in High Temperature Superconductors," preprint.
126. E.J. Ansaldi, Z.R. Wang, J.H. Cho, D.C. Johnston, and T.M. Riseman, "Magnetic Penetration Depth of  $\text{Ba}_{0.625}\text{K}_{0.375}\text{BiO}_3$ ," *Physica C*, vol. 185-189, pp. 1889-1890, 1991.
127. Van Duzer and Turner, p. 125.
128. R.A. Schweinfurth, C.E. Platt, M.R. Teepe, and D.J. Van Harlingen, "Electrical and magnetic transport properties of laser-deposited  $\text{Ba}_{1-x}\text{K}_x\text{BiO}_3$  thin films," *Appl. Phys. Lett.*, vol. 61, pp. 480-482, 1992.
129. U. Welp, W.K. Kwok, G.W. Crabtree, H. Claus, K.G. Vandervoort, B. Dabrowski, A.W. Mitchell, D.R. Richards, D.T. Marx, and D.G. Hinks, "The Upper Critical Field of  $\text{Ba}_{1-x}\text{K}_x\text{BiO}_3$ ," *Physica C*, vol. 156, pp. 27-34, 1988.

130. W.K. Kwok, U. Welp, G.W. Crabtree, K.G. Vandervoort, R. Hulscher, Y. Zheng, B. Dabrowski, and D.G. Hinks, "Magnetic and resistive measurements of the superconducting critical fields of melt-cast  $\text{Ba}_{0.65}\text{K}_{0.35}\text{BiO}_3$ ," *Phys. Rev. B*, vol. 40, pp. 9400-9403, 1989.
131. Y. Nagata, N. Suzuki, and T. Uchida, "Electrical resistivity of single crystal  $\text{Ba}_{1-x}\text{K}_x\text{BiO}_3$ ," *Physica C*, vol. 195, pp. 195-198, 1992.
132. N. Savvides, S.J. Collocott, C. Andrikidis, and K.H. Müller, "AC susceptibility, resistivity, and specific heat of the cubic superconductor  $\text{Ba}_{0.6}\text{K}_{0.4}\text{BiO}_3$ ," *Physica C*, vol. 171, pp. 181-186, 1990.
133. H.C. Yang, M.H. Hsieh, D.S. Lee, and H.E. Horng, "Magnetic properties of polycrystalline  $\text{Ba}_{0.5}\text{K}_{0.5}\text{BiO}_3$ ," *Phys. Rev. B*, vol. 42, pp. 2551-2553, August 1990.
134. J.D. Jorgensen, M.A. Beno, D.G. Hinks, L. Soderholm, K.J. Volin, R.L. Hitterman, J.D. Grace, I.K. Schuller, C.U. Segre, K. Zhang, and M.S. Kleefisch, "Oxygen ordering and the orthorhombic-to-tetragonal phase transition in  $\text{YBa}_2\text{Cu}_3\text{O}_{7-x}$ ," *Phys. Rev. B*, vol. 36, pp. 3608-3615, Sept. 1987.
135. A.G. Khachatryan, S.V. Semenovskaya, and J.W. Morris, Jr., "Phase diagram of the superconducting oxide  $\text{YBa}_2\text{Cu}_3\text{O}_{6+\delta}$ ," *Phys. Rev. B*, vol. 37, pp. 2243-2246, Feb. 1988.
136. R.J. Cava, B. Batlogg, C.H. Chen, E.A. Rietman, S.M. Zahurak, and D. Werder, "Single-phase 60-K bulk superconductor in annealed  $\text{Ba}_2\text{YCu}_3\text{O}_{7-\delta}$  ( $0.3 < \delta < 0.4$ ) with correlated oxygen vacancies in the Cu-O chains," *Phys. Rev. B*, vol. 36, pp. 5719-5722, Oct. 1987.
137. H. Steinfink, J.S. Swinnea, Z.T. Sui, H.M. Hsu, and J.B. Goodenough, "Identification and Structural Implications of the 90 K Superconducting Phase," *J. Am. Chem. Soc.*, vol. 109, pp. 3348-3353, 1987.
138. A. Williams, G.H. Kwei, R.B. Von Dreele, A.C. Larson, I.D. Raistrick, and D.L. Bish, "Joint x-ray and neutron refinement of the structure of superconducting  $\text{YBa}_2\text{Cu}_3\text{O}_{7-x}$ : Precision structure, anisotropic thermal parameters, strain, and cation disorder," *Phys. Rev. B*, vol. 37, pp. 7960-7962, May 1988.
139. X. Zeng, X. Jiang, H. Qi, D. Pang, N. Zhu, and Z. Zhang, "Relationship between superconductivity and lattice distortion in Y-Ba-Cu-O compounds," *Appl. Phys. Lett.*, vol. 51, pp. 692-693, Aug. 1987.
140. R.A. Laudise, L.F. Schneemeyer, and R.L. Barns, "Crystal Growth of High Temperature Superconductors - Problems, Successes, Opportunities," *J. Cryst. Growth*, vol. 85, pp. 569-575, 1987.
141. B. Batlogg, "Physical Properties of Cuprate Superconductors: An Introduction," in *Proc. Toshiba International School of Superconductivity*, Kyoto, 1991, pp. 1-21.
142. L.F. Mattheiss and D.R. Hamann, "Electronic Structure of the High  $T_c$  Superconductor  $\text{Ba}_2\text{YCu}_3\text{O}_{6.9}$ ," *Solid State Commun.*, vol. 63, pp. 395-399, 1987.
143. J.D. Jorgensen, "Defects and Superconductivity in the Copper Oxides," *Physics Today*, vol. 44, pp. 34-40, June 1991.
144. Y. Iye, "Anisotropic Transport Properties of High  $T_c$  Oxides," *International Journal of Modern Physics B*, vol. 3, pp. 367-388, 1989.

145. W.J. Gallagher, "Studies at IBM on anisotropy in single crystals of the high-temperature oxide superconductor  $\text{Y}_1\text{Ba}_2\text{Cu}_3\text{O}_{7-x}$ ," J. Appl. Phys., vol. 63, pp. 4216-4219, April 1988.
146. JCPDS Card File Data
147. R.W. Simon, A.E. Lee, C.E. Platt, K.P. Daly, J.A. Luine, C.B. Eom, P.A. Rosenthal, X.D. Wu, and T. Venkatesan, "Growth of High-Temperature Superconductor Thin Films on Lanthanum Aluminate Substrates," in *Science and Technology of Thin-Film Superconductors*, New York: Plenum Press, p. 339, 1989.
148. *Thermophysical Properties of Matter*, New York: Purdue Research Foundation, pp. 176, 288, and 570, 1977.
149. M. Sasaura, S. Miyazawa, and M. Mukaida, "Thermal expansion coefficients of high- $T_c$  superconductor substrate  $\text{NdGaO}_3$  single crystal," J. Appl. Phys., vol. 68, pp. 3643-3644, 1990.
150. R.M. Fleming, P. Marsh, R.J. Cava, and J.J. Krajewski, "Temperature dependence of the lattice parameters in the 30-K superconductor  $\text{Ba}_{0.6}\text{K}_{0.4}\text{BiO}_3$ ," Phys. Rev. B, vol. 38, pp. 7026-7028, 1988.
151. J. Talvacchio and G.R. Wagner, "High- $T_c$  film development for electronic applications," in *Superconductivity Applications for Infrared and Microwave Devices*, SPIE Proc., vol. 1292, p.2, 1990.
152. D.M. Kroeger, A. Choudhury, J. Brynestad, R.K. Williams, R.A. Padgett, and W.A. Coghlan, "Grain-boundary compositions in  $\text{YBa}_2\text{Cu}_3\text{O}_{7-x}$  from Auger electron spectroscopy of fracture surfaces," J. Appl. Phys., vol. 64, pp. 331-335, July 1988.
153. D. Halliday and R. Resnick, *Physics*, New York: John Wiley & Sons, 1978, p. 845.
154. A.H. Carim, S.N. Basu, and R.E. Muenchausen, "Dependence of crystalline orientation on film thickness in laser-ablated  $\text{YBa}_2\text{Cu}_3\text{O}_{7-\delta}$  on  $\text{LaAlO}_3$ ," Appl. Phys. Lett., vol. 58, pp. 871-873, Feb. 1991.
155. K. Kinoshita, A. Matsuda, H. Shibata, T. Ishii, T. Watanabe, and T. Yamada, "Crystal Structure and Superconductivity in  $\text{Ba}_2\text{Y}_{1-x}\text{Pr}_x\text{Cu}_3\text{O}_{7-y}$ ," Jpn. J. Appl. Phys., vol. 27, pp. L1642-L1645, Sept. 1988.
156. J.M. Tarascon, P. Barboux, P.F. Miceli, L.H. Greene, G.W. Hull, M. Eibschutz, and S.A. Sunshine, "Structural and physical properties of the metal (M)-substituted  $\text{YBa}_2\text{Cu}_{3-x}\text{M}_x\text{O}_{7-y}$  perovskite," Phys. Rev. B, vol. 37, pp. 7458-7469, May 1988.
157. Average of values from many sources
158. J.H. Lau and L.L. Moresco, "Mechanical Behavior of Microstrip Structures Made from  $\text{YBa}_2\text{Cu}_3\text{O}_{7-x}$  Superconducting Ceramics," IEEE Transactions on Components, Hybrids, and Manufacturing Technology, pp. 168-175, 1988.
159. Van Duzer and Turner, p. 184.
160. Manual for "US" sputtering gun
161. C.D. Wagner, W.M. Riggs, L.E. Davis, and J.F. Moulder, *Handbook of X-Ray Photoelectron Spectroscopy*, Eden Prairie, MN: Perkin-Elmer Corporation, 1979, pp. 4-163.

162. J.J. Friel and N.C. Barbi, *X-Ray Microanalysis and Computer-Aided Imaging*, Princeton, NJ: Princeton Gamma-Tech, pp. 4-47.
163. M.G. Lagally, "Diffraction Techniques," in *Methods of Experimental Physics*, vol. 22, New York: Academic Press, Inc., 1985, pp. 237-298.
164. Courtesy of Philips Analytical X-Ray
165. B.D. Cullity, *Elements of X-Ray Diffraction*, Reading, MA: Addison-Wesley Publishing Co., 1978, p. 501.
166. L.J. van der Pauw, "A Method of Measuring Specific Resistivity and Hall Effect of Discs of Arbitrary Shape," Philips Research Reports, vol. 13, pp. 1-9, Feb. 1958.
167. P. Horowitz and W. Hill, *The Art of Electronics*, New York: Cambridge University Press, 1990, pp. 1031-1032.
168. S. Pei, J.D. Jorgensen, D.G. Hinks, Y. Zheng, D.R. Richards, B. Dabrowski, and A.W. Mitchell, "Structure and Chemistry of  $\text{Ba}_{1-x}\text{K}_x\text{BiO}_3$ -d at High Temperature," J. Solid State Chem., vol. 95, pp. 29-38, 1991.
169. J.R. Gavaler, J. Talvacchio, T.T. Braggins, M.G. Forrester, and J. Gregg, "Critical parameters in the single-target sputtering of  $\text{YBa}_2\text{Cu}_3\text{O}_7$ ," J. Appl. Phys., vol. 70, pp. 4383-4391, Oct. 1991.
170. P.K. Gallagher, "Characterization of  $\text{Ba}_2\text{YCu}_3\text{O}_x$  as a function of Oxygen partial pressure - Part I: Thermoanalytical measurements," Advanced Ceramic Materials, vol. 2, pp. 632-639, 1987.
171. B.A. Baumert and J. Talvacchio, "Artificial Barriers for Ba-K-Bi-O Tunnel Junctions," IEEE Transactions on Applied Superconductivity, vol. 3, pp. 1567-1570, March 1993.
172. M.A. Sobolewski, S. Semancik, E.S. Hellman, and E.H. Hartford, "The effects of oxidation and air exposure on  $\text{Rb}_x\text{Ba}_{1-x}\text{BiO}_3$  superconducting thin films," J. Vac. Sci. Technol. A, vol. 9, pp. 2716-2720, Sept./Oct. 1991.
173. E.S. Hellman, E.H. Hartford, Jr., and E.M. Gyorgy, "Epitaxial  $\text{Ba}_{1-x}\text{K}_x\text{BiO}_3$  films on MgO: Nucleation, cracking, and critical currents," Appl. Phys. Lett., vol. 58, pp. 1335-1357, 1991.
174. D.P. Norton, J.D. Budai, B.C. Chakoumakos, and R. Feenstra, "Epitaxial growth of  $\text{Ba}_{1-x}\text{K}_x\text{BiO}_3$  thin films by pulsed-laser deposition," Appl. Phys. Lett., vol. 62, pp. 414-416, 1993.
175. M.G. Lagally and D.E. Savage, "Quantitative Electron Diffraction from Thin Films," MRS Bulletin, vol. 18, pp. 24-31, January 1993.
176. P.R. Pukite, J.M. Van Hove, and P.I. Cohen, "Sensitive reflection high-energy electron diffraction measurement of the local misorientation of vicinal GaAs surfaces," Appl. Phys. Lett., vol. 44, pp. 456-458, 1984.
177. D.A. Porter and K.E. Easterling, *Phase Transformations in Metals and Alloys*, London: Van Nostrand Reinhold Co., 1989, p. 200.
178. D.H. Lowndes, X.Y. Zheng, S. Zhu, J.D. Budai, and R.J. Warmack, "Suppression of the spiral-growth mechanism in epitaxial  $\text{YBa}_2\text{Cu}_3\text{O}_{7-x}$  films grown on miscut substrates," Appl. Phys. Lett., vol. 61, pp. 852-854, 1992.

179. B.H. Moeckly, S.E. Russek, D.K. Lathrop, R.A. Buhrman, M.G. Norton, and C.B. Carter, "Growth and Properties of  $\text{YBa}_2\text{Cu}_3\text{O}_7$  thin films on vicinal and polycrystalline MgO substrates," *Appl. Phys. Lett.*, vol. 57, pp. 2951-2953, 1990.
180. M.G. Norton, B.H. Moeckly, C.B. Carter, and R.A. Buhrman, "Growth mechanism of  $\text{YBa}_2\text{Cu}_3\text{O}_{7-d}$  thin films on vicinal MgO," *Journal of Crystal Growth*, vol. 114, pp. 258-263, 1991.
181. L.A. Tietz, S.R. Summerfelt, G.R. English, and C.B. Carter, "Early Stages of the heteroepitactic growth of hematite on (0001)  $\text{Al}_2\text{O}_3$  by transmission electron microscopy," *Appl. Phys. Lett.*, vol. 55, pp. 1202-1204, 1989.
182. J.A. Venables and G.L. Price, "Nucleation of Thin Films," in *Epitaxial Growth, Part B*, New York: Academic Press, 1975, pp. 381-436.
183. J.W. Matthews, D.C. Jackson, and A. Chambers, "Effect of Coherency Strain and Misfit Dislocations on the Mode of Growth of Thin Films," *Thin Solid Films*, vol. 26, pp. 129-134, 1975.
184. J.G. Simmons, "Low-Voltage Current-Voltage Relationship of Tunnel Junctions," *J. Appl. Phys.*, vol. 34, p. 238, 1963.
185. A. Manthiram, S.-J. Lee, and J.B. Goodenough, "Influence of Ca on the Superconductivity of  $\text{Y}_{1-x}\text{Ca}_x\text{Ba}_2\text{Cu}_3\text{O}_{7-\delta}$ ," *J. Solid State Chem.*, vol. 73, pp. 278-282, 1988.
186. Y. Oda, H. Toyoda, N. Kawaji, I. Nakada, and K. Asayama, "The Characterization of  $\text{YBa}_2(\text{Cu}_{1-x}\text{Co}_x)_3\text{O}_y$ ," *Jpn. J. Appl. Phys.*, vol. 27, pp. L1702-L1705, Sept. 1988.
187. K. Tanabe, Y. Enomoto, and A. Yamaji, "Electrical response of  $\text{Ba}_{1-x}\text{K}_x\text{BiO}_3$  polycrystalline thin films to infrared radiation," *Appl. Phys. Lett.*, vol. 57, pp. 2719-2721, 1990.
188. J.D. Verhoeven, *Fundamentals of Physical Metallurgy*, New York: John Wiley & Sons, 1975, p. 155.
189. P. Shewmon, *Diffusion in Solids*, Warrendale, PA: The Minerals, Metals & Materials Society, 1989, p. 197.
190. F.S. Galasso, *Structure, Properties, and Preparation of Perovskite-Type Compounds*, New York: Pergamon Press, 1969, pp. 18-19.
191. B.D. Cullity, p. 119.
192. Ibid, p. 91.
193. Ibid, pp. 520-522.
194. Ibid, p. 139.
195. Ibid, p. 523.